

THE EFFECT OF ENHANCED DIABATIC HEATING ON STRATOSPHERIC CIRCULATION

by
Mary M. Kleb

A dissertation submitted in partial fulfillment
of the requirements for the degree of
Doctor of Philosophy
(Atmospheric and Space Sciences)
in The University of Michigan
1997

Doctoral Committee:

Professor S. Roland Drayson, Chairperson
Professor William R. Kuhn
Professor Joyce E. Penner
Associate Professor Kenneth G. Powell
William L. Grose, National Aeronautics and Space
Administration, Langley Research Center

To Bill and Zoe for keeping me smiling.

TABLE OF CONTENTS

DEDICATION	ii
LIST OF FIGURES	v
CHAPTER	
I. INTRODUCTION	1
II. MODEL STUDIES OF DIABATIC HEATING ANOMALY	7
III. MODEL DESCRIPTION	22
3.1 Dynamics	22
3.2 Radiation	27
3.3 Numerical Techniques	30
3.4 Model Modifications	31
3.4.1 Hydrogen Fluoride Initialization	31
3.4.2 Diabatic Heating Perturbation	43
3.5 Summary	48
IV. COMPARISON OF MODELED HYDROGEN FLUORIDE DISTRIBUTION WITH OBSERVED HYDROGEN FLUO- RIDE DISTRIBUTION	50
4.1 Zonal Comparison	51
4.1.1 July	51
4.1.2 January	58
4.2 Vertical Profile Comparison	64
4.2.1 July	64
4.2.2 January	70
4.3 Conclusions	75
V. COMPARISON OF CONTROL AND PERTURBED MODEL SIMULATIONS	77

5.1	Comparison of Modeled and Actual Temperature and Zonal Wind	77
5.2	Zonal Mean	80
5.2.1	Temperature	80
5.2.2	Zonal Wind	81
5.2.3	Meridional Wind	87
5.2.4	Geopotential Height	88
5.3	Climatological Variance	90
5.3.1	Temperature	93
5.3.2	Zonal Wind	93
5.3.3	Geopotential Height	96
5.3.4	Variance in the Real Atmosphere	96
5.4	Temporal Evolution	100
5.4.1	Temperature	100
5.4.2	Zonal Wind	102
5.4.3	Meridional Wind	105
5.4.4	Geopotential Height	108
5.5	Wave Variance	110
5.5.1	Temperature	110
5.5.2	Zonal Wind	113
5.5.3	Meridional Wind	113
5.5.4	Geopotential Height	121
5.6	Conclusions	121

VI. COMPARISON OF MODEL RESULTS AND OBSERVATIONAL DATA 123

6.1	Hydrogen Fluoride	123
6.2	Temperature	136
6.3	Ozone	141
6.4	Conclusions	149

VII. SUMMARY 151

APPENDICES 157

BIBLIOGRAPHY 160

LIST OF FIGURES

Figure

3.1	HALOE hydrogen fluoride in ppbv versus ECMWF isentropic potential vorticity in $\frac{Km^2}{kgs}$ at the 158 mb pressure level. The solid lines are polynomial fits to segments of the data.	34
3.2	Same as in Figure 3.1 but at the 108 mb pressure level.	34
3.3	Same as in Figure 3.1 but at the 68 mb pressure level.	35
3.4	Same as in Figure 3.1 but at the 46 mb pressure level.	35
3.5	Same as in Figure 3.1 but at the 29 mb pressure level.	36
3.6	Same as in Figure 3.1 but at the 19 mb pressure level.	36
3.7	Same as in Figure 3.1 but at the 13 mb pressure level.	37
3.8	Zonal mean hydrogen fluoride (ppbv) on model day July 6, two model days after model initialization.	40
3.9	Zonal mean hydrogen fluoride (ppbv) on model day June 15, almost one year after model initialization.	41
3.10	Corrected zonal mean hydrogen fluoride (ppbv) on model day June 15, almost one year after model initialization.	41
4.1	Sunrise HALOE hydrogen fluoride (HF) distribution, July 4 through August 20, 1994. Contour levels are in parts per billion by volume (ppbv).	52
4.2	Summertime LaRC GCM HF distribution.	52

4.3	Fractional difference divided by 100 between HALOE and model HF distributions for the July-August time period. Dashed (negative) contours indicate model values lower than HALOE values. solid (positive) contours indicate model values higher than HALOE values.	53
4.4	Longitudinal variance in HALOE HF distribution for the time period July 4 through August 20, 1994.	55
4.5	Longitudinal variance in MODEL HF distribution for the time period July 4 through August 20.	55
4.6	Vertical component of the diabatic circulation calculated from UKMO data for the time period July 4 through August 20, 1994.	57
4.7	Vertical component of the diabatic circulation calculated from model data for the time period July 4 through August 20.	57
4.8	Same as in Figure 4.1 except for the time period January 5 through February 22, 1994.	59
4.9	Same as in Figure 4.2 except for the January 5 - February 22 time period.	59
4.10	Same as in Figure 4.3 except for the January 5 - February 22 time period.	60
4.11	Longitudinal variance in HALOE HF distribution for the time period January 5 through February 22, 1994.	61
4.12	Longitudinal variance in MODEL HF distribution for the time period January 5 through February 22.	61
4.13	Vertical component of the diabatic circulation calculated from UKMO data for the time period January 5 through February 22, 1994. . . .	62
4.14	Vertical component of the diabatic circulation calculated from model data for the time period January 5 through February 22.	62

4.15	A comparison of July hydrogen fluoride (HF) data from HALOE and the LaRC GCM. The HALOE data is from 1993 (solid), 1994 (dotted), and 1995 (dashed), averaged over the days indicated and spans the region 41.4S to 45.9S. The horizontal lines indicate the standard deviation of the unaveraged vertical profiles at those altitudes. Model data is at 43.3S.	65
4.16	Same as in Figure 4.15 except HALOE data spans 27.3S to 35.9S and model data is at 32.1S.	66
4.17	Same as in Figure 4.15 except HALOE data spans 5.2S to 7.7N and model data is at 4.2N.	67
4.18	Same as in Figure 4.15 except HALOE data spans 9.7N to 22.0N and model data is at 18.1N.	68
4.19	Same as in Figure 4.15 except HALOE data spans 29.5N to 38.9N and model data is at 34.9N.	69
4.20	Same as in Figure 4.15 except HALOE data spans 52.1N to 58.0N and model data is at 54.4N.	69
4.21	Same as in Figure 4.15 except in January, HALOE data spans 46.6N to 48.0N and model data is at 46.0N.	70
4.22	Same as in Figure 4.21 except HALOE data spans 29.7N to 37.6N and model data is at 32.1N.	71
4.23	Same as in Figure 4.21 except HALOE data spans 7.2S to 7.1N and model data is at 1.4S.	72
4.24	Same as in Figure 4.21 except HALOE data spans 24.7S to 12.5S and model data is at 18.1S.	73
4.25	Same as in Figure 4.21 except HALOE data spans 39.2S to 29.3S and model data is at 34.9S.	73
4.26	Same as in Figure 4.21 except HALOE data spans 57.5S to 51.3S and model data is at 54.4S.	74
5.1	July average for the zonal mean temperature difference. Contour interval is 1 K.	80
5.2	October monthly average of temperature for the control case.	82

5.3	Same as Figure 5.1 except for October.	82
5.4	December monthly average of temperature for the control case. . . .	83
5.5	Same as Figure 5.1 except for December.	83
5.6	July average for the zonal mean zonal wind difference. Contour interval is 1 m/s.	84
5.7	October monthly average of zonal wind for the control case.	85
5.8	Same as Figure 5.6 except for October.	85
5.9	December monthly average of zonal wind for the control case. . . .	86
5.10	Same as Figure 5.6 except for December.	86
5.11	July average for the zonal mean geopotential height difference. Con- tour interval is 25 km.	88
5.12	Same as Figure 5.11 except for October.	89
5.13	Same as Figure 5.11 except for December.	89
5.14	Climatological variance in ten consecutive October monthly means of zonally averaged temperature. Contour levels are 1, 10, and 100 K^2	91
5.15	Perturbation variance for October monthly mean of zonally averaged perturbed temperature data. Contour levels are 1, 10, and 100 K^2 . .	91
5.16	Same as Figure 5.14 except for December.	92
5.17	Same as Figure 5.15 except for December.	92
5.18	Same as Figure 5.14 except for zonal wind. Contour levels are 1, 10, and 100 $(m/s)^2$	94
5.19	Same as Figure 5.15 except for zonal wind. Contour levels are 1, 10, and 100 $(m/s)^2$	94
5.20	Same as Figure 5.18 except for December.	95

5.21	Same as Figure 5.19 except for December.	95
5.22	Same as Figure 5.14 except for geopotential height. Contour levels are 100, 1000, and 10,000 km ²	97
5.23	Same as Figure 5.15 except for geopotential height. Contour levels are 100, 1000, and 10,000 km ²	97
5.24	Same as Figure 5.22 except for December.	98
5.25	Same as Figure 5.23 except for December.	98
5.26	Temporal evolution of perturbed temperature minus control temperature at 90°E and 29 mb. Contour interval is 1 K.	101
5.27	Same as Figure 5.26 except at 270°E.	102
5.28	Temporal evolution of perturbed zonal wind minus control zonal wind at 0°E and 19 mb. Contour interval is 2 m/s.	103
5.29	Same as Figure 5.28 except at 180°E.	104
5.30	Temporal evolution of perturbed meridional wind minus control meridional wind at 90°E and 19 mb. Contour interval is 2 m/s.	106
5.31	Same as Figure 5.30 except at 270°E.	106
5.32	Temporal evolution of perturbed meridional wind minus control meridional wind at 90°E and 2 mb. Contour interval is 2 m/s.	107
5.33	Same as Figure 5.32 except at 270°E.	107
5.34	Temporal evolution of perturbed geopotential height minus control geopotential height at 90°E and 19 mb. Contour interval is 25 km.	109
5.35	Same as Figure 5.34 except at 270°E.	109
5.36	October monthly mean of the temperature wave variance for the control simulation. The contour interval is 50 K ²	111
5.37	Same as Figure 5.36 except for the perturbed simulation.	111
5.38	December monthly mean of the temperature wave variance for the control simulation. The contour interval is 50 K ²	112

5.39	Same as Figure 5.38 except for the perturbed simulation.	112
5.40	October monthly mean of the zonal wind wave variance for the control simulation. The contour interval is 100 (m/s) ²	115
5.41	Same as Figure 5.40 except for the perturbed simulation.	115
5.42	December monthly mean of the zonal wind wave variance for the control simulation. The contour interval is 100 (m/s) ²	116
5.43	Same as Figure 5.42 except for the perturbed simulation.	116
5.44	October monthly mean of the meridional wind wave variance for the control simulation. The contour interval is 100 (m/s) ²	117
5.45	Same as Figure 5.44 except for the perturbed simulation.	117
5.46	December monthly mean of the meridional wind wave variance for the control simulation. The contour interval is 100 (m/s) ²	118
5.47	Same as Figure 5.46 except for the perturbed simulation.	118
5.48	October monthly mean of the geopotential height wave variance for the control simulation. The contour interval is 20 km ²	119
5.49	Same as Figure 5.48 except for the perturbed simulation.	119
5.50	December monthly mean of the geopotential height wave variance for the control simulation. The contour interval is 20 km ²	120
5.51	Same as Figure 5.50 except for the perturbed simulation.	120
6.1	October monthly average of hydrogen fluoride for the control case. .	124
6.2	October monthly average for the zonal mean hydrogen fluoride difference.	124
6.3	December monthly average of hydrogen fluoride for the control case.	125
6.4	December monthly average for the zonal mean hydrogen fluoride difference.	125
6.5	Control eddy hydrogen fluoride flux for December 1, 11, 21, and 31.	128

6.6	Difference (perturbed - control) eddy hydrogen fluoride flux for December 1, 11, 21, and 31.	129
6.7	Control eddy heat flux for November 1, 11, and 21.	130
6.8	Control eddy heat flux for December 1, 11, 21, and 31.	131
6.9	Difference (perturbed - control) eddy heat flux for November 1, 11, and 21.	133
6.10	Difference (perturbed - control) eddy heat flux for December 1, 11, 21, and 31.	134
6.11	Control geopotential height in km ($\times 10^{-2}$) at 3.44 mb. Data is southern hemisphere on November 1 and 15 and December 1 and 15.	135
6.12	October monthly mean of the vertical component of the diabatic circulation for the control case.	147
6.13	Same as Figure 6.12 except for perturbed minus control cases.	147
6.14	Same as Figure 6.12 except for December.	148
6.15	Same as Figure 6.13 except for December.	148

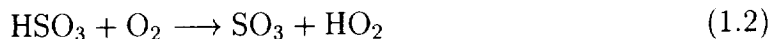
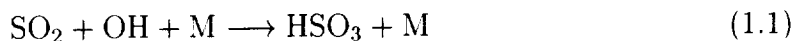
CHAPTER I

INTRODUCTION

The Earth's atmosphere can be divided into layers according to the atmospheric temperature profile. For the most part the stratosphere is characterized by temperature increasing with altitude due to the absorption of ultra violet light by oxygen and ozone. The lower stratosphere is essentially isothermal. Since warmer air lies above colder air there is very little vertical mixing into and within the stratosphere. The tropopause marks the lower boundary of the stratosphere. The precise location of the tropopause ranges between 8 and 18 kilometers depending on season and latitude. The stratopause or upper boundary is located around 50 kilometers. Compared to the troposphere, the layer of the atmosphere from 0 to roughly 15 kilometers, the stratosphere is relatively dry and rich in ozone. Even though the stratosphere accounts for less than 20% of the total mass of the atmosphere, it nonetheless plays an important role in the global climate through dynamical, radiative, and chemical processes. These processes interact closely and to understand the stratosphere, it is necessary to understand the roles that the dynamical, radiative, and chemical processes play. Ozone plays a major role in the chemistry and radiative balance of the stratosphere. Dynamics are important in the transfer of energy and in the modulation of stratospheric ozone. These processes affect each other and in order to study

these subjects, dynamics must be included and therefore understood.

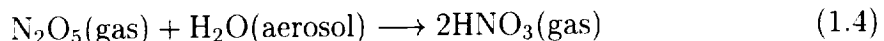
The stratosphere can be perturbed by anthropogenic influences (*e.g.* chlorofluorocarbon induced ozone depletion) and naturally occurring events such as the eleven year solar cycle and volcanic eruptions. Antarctic ozone depletion is a complex interaction of anthropogenic influences and naturally occurring dynamical, radiative, and chemical processes. This phenomenon is fairly well understood. However there is also some evidence for midlatitude ozone depletion that is not completely understood but may be related to volcanic aerosols [1]. Not all volcanic eruptions affect the stratosphere, enough vertical force must exist to penetrate the tropopause. If a volcano does penetrate into the stratosphere, the sulfur dioxide gas reacts to form sulfuric acid aerosols according to the following mechanism [2].



The predominate aerosol forming processes for H_2SO_4 are believed to be heterogeneous and heteromolecular nucleation of the H_2SO_4 - H_2O system around Aitken particles [3]. In the stratosphere, these aerosols can remain for one to three years before removal by sedimentation [4]. Their effects on the stratosphere are important and are closely related to one another.

One possible result of volcanic material in the stratosphere is the depletion of nitrogen oxides. Nitrogen oxides (NO_x) consist of NO , NO_2 , NO_3 , and N_2O_5 [5] and are important in the modulation of stratospheric ozone. The concentration of NO_x depends on stratospheric temperature, ozone levels, and planetary albedo, all of which can be affected by volcanic aerosols [6]. It is also believed that nitrogen oxide

can be removed from the stratosphere through heterogeneous reactions (reactions that involve elements in different phases) occurring on sulfuric acid (volcanic) aerosol surfaces similar to the heterogeneous reactions on polar stratospheric clouds which are responsible for Antarctic ozone depletion [7], [5], [8]. The following reaction on volcanic aerosol surfaces converts NO_x to HNO_3 (nitric acid) [5].



In sunlight N_2O_5 rapidly photodissociates into NO_2 and NO_3 . Nitrate (NO_3) quickly photodissociates and reacts to form NO and O_2 . Nitric acid on the other hand, is a long lived species and its formation in reaction (1.4) renders more reactive nitrogen essentially inert [9].

While nitrogen dioxide participates in a catalytic cycle that destroys ozone, at certain altitudes other chemical reactions dominate making it crucial to the abatement of ozone loss [10]. Nitrogen dioxide can slow ozone destruction by sequestering ClO in the chlorine nitrate (ClNO_3) reservoir [9]. It is believed that without NO_2 available to deactivate ClO , the net result of reaction (1.4) is to reduce stratospheric ozone at midlatitudes [7], [11], [12] (this is not expected to be important in the tropics where ozone production greatly exceeds ozone loss [13]).

Another important result of volcanic aerosol in the stratosphere is a radiative perturbation [14]. In the tropics the cloud of sulfuric acid aerosols enhances reflectivity in the visible and ultraviolet wavelengths [15]. This increases the reflectivity in the lower stratosphere, and has the effect of enhancing ozone depletion by increasing the ozone photodissociation rates above the aerosol cloud in the lower stratosphere [16]. The impact of enhanced photodissociation rates is expected to be greatest in the tropics where the aerosol cloud can remain for one to three years [15].

Anomalous diabatic heating of the stratosphere is another result of the volcanic aerosols. This heating occurs as a result of absorption of solar and planetary radiation by the aerosols and the absorption of enhanced diffuse radiation by ozone [14]. The heating could impact the dynamics of the stratosphere as well as transport of important trace species (*e.g.* ozone) since a warmer tropical stratosphere should have stronger upward motions [14]. Hofmann et al. report depleted ozone values in the upper and lower stratosphere in the southern hemisphere in the spring of 1991 that were 50% greater than the ‘normal’ ozone depletion [17]. These additional losses were attributed to ozone poor air (due to heterogeneous reactions on volcanic aerosols) being transported to high latitudes and altitudes [17]. After the eruption of El Chichón in Mexico, Dunkerton and Delisi [18] reported that in addition to the warming of the lower tropical stratosphere, a cooling occurred in the middle and upper stratosphere. This cooling could only partly be explained as a dynamical response to subtropical aerosol heating centered off the equator. It could not be explained through a radiative response to volcanic aerosol in the lower stratosphere.

During the summer and fall of 1991 the fortuitous timing of two events made possible detailed studies of the above mentioned phenomena. In September 1991 the Upper Atmosphere Research Satellite (UARS) was launched. One goal of UARS was to supply new data on chemical constituents, temperature, and winds in the stratosphere and mesosphere in an effort to better understand the factors that modulate stratospheric ozone [19].

Three months prior to the UARS launch, Mt. Pinatubo in the Philippines (15.1°N, 120.4°E) erupted [20]. Possibly the largest eruption of the century, it is the first volcanic impact on the stratosphere to be observed and tracked by satellite [21]. Mt. Pinatubo spewed millions of tons of sulfur dioxide gas into the stratosphere

where it formed sulfuric acid aerosols. One of the instruments on UARS, the Halogen Occultation Experiment (HALOE), confirmed the existence of subsidence within the polar vortex in the Antarctic during the spring of 1991 and provided a quantitative estimate of the rate of descent [22]. Over the course of one year, HALOE coverage extends from 80°N to 80°S, from 10 km to between 60 and 120 km depending on the constituent [23]. Vertical profiles (mixing ratio vs. altitude in pressure) of several constituents, including hydrogen fluoride, showed evidence of very strong unmixed vertical descent inside the polar vortex, but none so dramatically as methane. The vertical profiles inside the polar vortex showed mixing ratios in the middle stratosphere to be as low as mixing ratios in the mesosphere and having weak vertical gradients. Since the source of methane is at the surface of the earth and it has a long photochemical lifetime in the stratosphere, these observations led to the conclusion that there was strong vertical descent (at least one scale height per month) between 65 and 25 km within the Antarctic polar vortex [22].

The objective of this research focuses on the stratospheric dynamical response to the increase in aerosol loading and subsequent enhanced diabatic heating resulting from the eruption of Mt. Pinatubo. In particular, can the rapid subsidence observed in the Arctic and Antarctic be affected by enhanced diabatic heating in the equatorial region.

The methodology used to study this topic is as follows. A realistic heating perturbation was incorporated into the LaRC 3-D GCM to study the dynamical response to the perturbation. A hydrogen fluoride tracer was also included in the LaRC GCM to study the impact the heating perturbation had on the tracer distribution. Specifically, could the high southern latitude changes in HF observed by HALOE in October 1991 be attributed to the enhanced heating of the stratosphere due to

Pinatubo aerosols. Finally observational data are used to determine if the same dynamical response was apparent in the real atmosphere.

The remaining chapters are organized as follows. Chapter II outlines previously completed studies of volcanic aerosol heating resulting from the eruptions of Mt. Pinatubo and El Chichón. Chapter III describes the Langley Research Center three dimensional general circulation model (GCM) and modifications made to that model for this study (addition of hydrogen fluoride tracer and diabatic heating enhancement). The hydrogen fluoride tracer is included in the LaRC GCM to study the impact the heating perturbation has on the tracer distribution. Specifically, can the high southern latitude changes in HF observed by HALOE in October 1991 be attributed to the enhanced heating of the stratosphere by Pinatubo aerosols. Chapter IV compares unperturbed hydrogen fluoride distribution to the hydrogen fluoride distribution measured by HALOE. In Chapter V a comparison of control and perturbed model runs is presented. These results are discussed in Chapter VI along with an analysis of satellite observations. Finally, Chapter VII is a summary of the research and concluding remarks.

CHAPTER II

MODEL STUDIES OF DIABATIC HEATING ANOMALY

Some model studies have already been completed addressing the issues of the magnitude of the temperature perturbation in the lower stratosphere as well as the effects of the perturbation on stratospheric circulation related to the eruptions of Mt. Pinatubo and El Chichón. The models ranged in sophistication from 3-D GCMs (general circulation model) to a 1-D radiative-convective model. This survey was restricted to radiative transfer calculations of heating rates given the aerosol loading and did not include measurements of stratospheric temperature anomalies which could not be definitively attributed to volcanic aerosols. The following is a summary of the studies, first for the Mt. Pinatubo eruption, then for the El Chichón eruption.

Young et al. [24] examined the radiatively forced dispersion of the Pinatubo aerosol cloud using three computational models; a three dimensional spectral primitive equation model, a three dimensional aerosol microphysical/transport model, and a radiative transfer model. The latitude/longitude aerosol distribution was initialized according to the TOMS SO_2 data from June 16 (day 1). The aerosol cloud was then advected in the transport model by winds calculated in the circulation model.

There was no sedimentation, coagulation, or nucleation explicitly calculated. The aerosols were small enough that sedimentation was negligible the first few months after the eruption and mass conversion from SO_2 to H_2SO_4 was parameterized based on observations.

After a 75 day simulation (corresponding to the end of August) there was a temperature perturbation of 8°C in a small area centered at the equator at an altitude of 26 km. Between 10°N and 45°N and between 21 and 30 km, the perturbation ranged from 1°C to 4°C . According to Labitzke and McCormick [25] tropical stratospheric temperatures were well below normal in June following the eruption and near mean in the beginning of July. A noticeable anomalous rise in temperatures began July 8. In order to approximate the heating rates necessary to achieve the 8°C perturbation calculated for the end of August by Young et al., we will assume the positive temperature perturbation began in mid July (approximately when Labitzke and McCormick noted an anomalous rise in temperatures). This assumption results in an average heating rate of $.18^\circ\text{C}/\text{day}$ from mid July through the end of August.

Young et al. calculated the movement of the aerosol cloud, but not global scale stratospheric motions induced from aerosol heating.

Pitari [14] simulated the heating of the aerosol layer in order to study its impact on stratospheric dynamics. This simulation was run with a three dimensional global model of the stratosphere for two cases, a control run (with no volcanic aerosols) and a perturbed run (includes Pinatubo aerosols). For the perturbed run, the aerosols varied in time and latitude according to aerosol backscatter measurements. The data of Winker and Osborn [26] were used to estimate aerosol content in tropical latitudes. Data from D'Altorio [27] were used for northern midlatitudes and data from Young (personal communication) for southern midlatitudes. Time evolution

was estimated based on measurements of optical thickness (Stowe et al. [28] and McCormick, personal communication). Aerosol composition was assumed to be 75% sulfuric acid.

The aerosol radiative heating rate is defined to be the sum of aerosol heating due to absorption of incident radiation, absorption/emission of infrared radiation, and absorption of diffuse solar radiation (radiation scattered by the aerosols). In order to reduce the computational time required in the calculation, parameterizations were made for each of the contributors to the radiative heating rate.

Pitari's results show a maximum net heating rate of approximately .2K/day from about 21 to 24km in August. The heating rate decreases above and below these altitudes. In December the maximum is still near .2 K/day at 24 km, but drops off more rapidly as altitude decreases than it did in August.

Pitari's study also addresses the impact that the calculated anomalous diabatic heating had on stratospheric circulation. Significant changes in the diabatic vertical velocity are found for winter and fall. In the northern hemisphere winter there is a substantial anomalous downward motion in the high latitude lower stratosphere. In addition, there is upwelling above 0.2 mb in the northern hemisphere high latitude region. The lower stratosphere perturbation is 10% of the diabatic circulation calculated for the control case [14]. Pitari reasons this perturbation in the vertical velocity is due to the fact that radiative equilibrium is not reached in the tropics and adiabatic cooling is similar in magnitude to the aerosol heating [14], and references cited therein. In the fall there is significant anomalous subsidence in the northern hemisphere stratosphere as well, but it is above 2 mb. A less pronounced subsidence in the southern hemisphere polar region also exists between roughly 20 mb and 1 mb [14].

Some uncertainties in this calculation exist. The major shortcomings include the calculation of the upward flux of planetary radiation at the lower boundary of each pressure level (which depends on emission from the ground and tropospheric clouds), the simplification of the δ -Eddington approximation in the calculation of the diffuse solar heating, and the calculation of the particle-optical parameters.

Kinne et al. [13] also calculated aerosol heating in order to investigate the effect of changing tropical ozone amounts on stratospheric circulation. The placement of the aerosol layer was between 18 and 26 km based on tropical lidar observations (*e.g.* [29]). Three months after the eruption, monthly averaged aerosol optical depths reached a maximum of 0.21 for visible wavelengths, followed by a continuous decline leading to optical depths of 0.15 six months after the eruption.

Very few specifics are given on the radiative transfer calculations. The model was two-stream and determined the heating or cooling in a tropical atmosphere. A random overlap of high, medium, and low clouds was also included. The cloud cover was assumed to be 55% low, 35% mid-level, and 15% high.

The calculated heating rates were approximately 0.3K/day. Infrared heating accounted for between 75% and 90% of the total heating, having a greater percentage at the lower levels of the aerosol cloud. The magnitude of the heating was greatest between 24 and 25 km.

There was no discussion of the accuracy of these calculations and also no model calculation of the dynamical response to the model-calculated abnormal heating. One important difference between these results and those of Pitari was that Pitari found that in the aerosol cloud the IR contribution was negative, while Kinne found it to be positive. The difference may arise from the way cloud cover was designated by Pitari and Kinne, since the infrared contribution is sensitive to radiative processes

associated with clouds. In the Pitari experiment there was no explicit parameterization for cloud cover. In order to calculate the upward flux of planetary radiation at each model level, Pitari calculated a weighted average (weight equaled percent cloud cover) of the ground surface flux and the flux coming from an average cloud altitude (6 km) [14]. Kinne included tropospheric clouds as described above.

Brasseur and Granier [5] used a two-dimensional (latitude - altitude) model simulation to study the impact of the Mt. Pinatubo eruption on stratospheric ozone concentrations. This model simulated the chemical, radiative, and dynamical processes in the middle atmosphere. The aerosol layer was centered over the equator between 16 and 28 km with a maximum surface area density of $100 \mu\text{m}^2/\text{cm}^3$ at 23 km. The volcanic cloud was confined between 15°N and 15°S and completely mixed zonally. The dispersion of the cloud was not simulated, instead specific instances in the dispersion were modeled.

Two September time-frame simulations were conducted, one with heterogeneous chemistry that ignored aerosol heating and one without heterogeneous chemistry that included aerosol heating. In the simulation without heterogeneous chemistry the aerosol layer absorbs radiation from the sun (ultraviolet, visible and near infrared) and terrestrial radiation, resulting in a heating of the tropical lower stratosphere. Brasseur and Granier assumed a constant heating rate of .4K/day at the cloud center. The resulting temperature increase ranged from 2 to 6 K between 16 and 25 km. Directly associated with the temperature increase was a strengthening of the mean meridional circulation by approximately 10%. The tropical regions had stronger upward circulation which was accompanied by stronger downward motions at higher latitudes.

Like Brasseur and Granier, Kinnison et al. [30] used a 2 dimensional (zonally-

averaged) chemical, radiative, transport model to study the effects of the Mt. Pinatubo eruption on stratospheric ozone abundances. For the reference atmosphere (not perturbed by volcanic aerosol), the aerosol surface area density was derived from SAGE II data. The surface area density varied in altitude (between 12 and 32 km), latitude (pole to pole), and time. The perturbed aerosol loading (due to the Pinatubo eruption) was derived from SAGE II and CLAES (Cryogenic Limb Array Etalon Spectrometer) data. Kinnison et al. [30] describe the process of combining the SAGE II and CLAES data in detail.

A 3 year simulation was executed, beginning December 22, 1990 and ending December 22, 1993. The maximum heating occurred in October and November, 1991. Introducing mid-October aerosol extinctions into a background atmosphere, the maximum heating rate due to solar radiation was .33 K/day near 30 km. The maximum heating rate due to infrared radiation was .27 K/day near 25 km. The maximum total aerosol heating rate was .47 K/day at about 25 km.

These changes in heating rates were then used to study changes in temperature and circulation (not concurrently). The perturbed temperature and circulation were compared to the corresponding unperturbed quantities from before the eruption. When the aerosol induced heating rates influenced only the temperature, there was a 5 to 6 K rise in temperature in the lower stratosphere. The maximum increase in temperature was centered slightly south of the equator. When the anomalous heating rates affected the circulation, there was an increase in the diabatic vertical velocities of 1.6 km per 100 days.

One source of error in this analysis is the calculation of the heating due to solar radiation. This calculation is highly dependent on the single scattering albedo (ω_o). The solar heating scales approximately as $1 - \omega_o$. Kinnison et al. chose a single scat-

tering albedo of 0.99. This value was slightly lower than the result of Mie calculations for H_2SO_4 which yielded a value of unity. Using $\omega_o = 0.99$ was more consistent with observations that attribute the lower value to absorption by the carbon aerosol.

Tie et al. [31] used a two dimensional chemical and dynamical model of the atmosphere to investigate the effect the Mt. Pinatubo eruption had on stratospheric ozone. The 2-D model was developed by Brasseur et al. and later modified by Brasseur and Granier [32], [5]. The model simulated the aerosol cloud for three years (corresponding to July 1991 through June 1994). The sulfur plume was injected into the tropical lower stratosphere (between 15°N to 5°S , and 19 and 26 km). Ninety percent of the sulfur was in the form of SO_2 gas, the rest as sulfate particles. The model simulated several microphysical properties such as heterogeneous nucleation, condensation, coagulation, sedimentation, and washout. Modified photolysis rates were also calculated to account for the effects of the aerosols. In addition, a cloud cover was assumed, which specified a random overlap of clouds at three levels in the atmosphere (818 mb, 520 mb, and 226 mb).

About two months after the eruption, the simulated volcanic plume was located between 17 and 30 km, with a maximum in sulfate mass concentration near 24 km. The maximum heating rate was slightly lower at 22 km. The absorption of long-wave radiation yielded a heating rate of .22 K/day. The scattering and absorption of solar radiation added another .06 K/day to the heating rate, for a total maximum heating rate of .28 K/day above the equator.

At 20 km, this additional heating resulted in a temperature perturbation and a perturbation in the vertical velocity. The temperature perturbation reached a maximum of 4.5 K at 10°N during November and December 1991, approximately six months after the eruption. One difference between the calculated and observed re-

sults of the temperature perturbation is the rate at which it diminished. Both the calculated and observed temperature change increased at a rate of 1 K/month for the first 4 months following the eruption. Following this, however, the calculated temperature perturbation decreased slower than the observed temperature perturbation. According to Tie et al. [31] this was most likely due to uncertainties in the calculation of the radiative effects of the sulfate aerosols. The total uncertainty in the net heating rate calculation was 20%.

The change in the vertical velocity was greatest during the first five months following the eruption. There was increased upward motions between 10°S and 20°N and increased subsidence in the midlatitudes of both the northern and southern hemispheres. The changes in the vertical velocities were up to 12% of the background vertical velocity (maximum of .25 mm/s).

Rosenfield et al. [33], used an interactive two-dimensional (latitude-height) model to study the effects of the Mt. Pinatubo eruption of stratospheric chemistry, radiation, and dynamics. This model coupled the Goddard Space Flight Center two-dimensional fixed transport chemistry model [34], and the zonally averaged radiative-dynamical model [35]. The coupled model is interactive in that the diabatic heating rates derived from model ozone and temperature fields are used to determine the temperatures and transport circulation. Gas phase chemical reactions which are temperature dependent were computed using model-predicted temperatures. The following is a brief description of the radiative, chemical, and dynamical modules and some results.

In the radiative portion of the coupled model, the calculation of clear sky heating rates included the effects of solar heating and infrared heating and cooling due to carbon dioxide, ozone, and water vapor. Temperature and ozone profiles used

in these computations were model predicted while the water vapor distribution was derived from the Limb Infrared Monitor of the Stratosphere (LIMS) and a tropospheric climatology. Cloud effects were specified such that the outgoing longwave flux at the top of the atmosphere was consistent with satellite observations. The volcanic aerosol distribution was determined using monthly and zonally averaged SAGE II $1\text{ }\mu\text{m}$ stratospheric extinction coefficients. Interpolation was used to obtain global coverage. The pre-Pinatubo aerosol distribution was based on the climatology compiled by Hitchman et al. [36]. The size distribution for background and volcanic aerosols was constant.

The chemistry module employs the family chemistry method described in [34]. Model coverage is global with a 10° grid resolution. There are 46 equally spaced (in pressure) pressure levels from the ground to about .002 mb. Concentrations are computed for 53 gas phase species and total concentrations of the odd nitrogen, odd oxygen, odd chlorine, and odd bromine families.

Heterogeneous reactions on sulfate aerosols as well as type I and type II PSCs are included. Model calculated temperatures are not used to determine PSC formation. PSC formation is based on a probability distribution which describes longitudinal temperature variability as a function of time of year and location. This is important since temperatures are about 10° colder than climatology in the lower stratosphere high latitude winter. However, this also means that PSC formation will not respond to changes in the temperature field due to the volcanic eruption.

The dynamical module is a momentum conserving advection scheme, advecting chemical constituents and dynamical quantities. Geographical coverage is near global (85.1°S to 85.1°N , 4.86° resolution) and from 2.66 km to 106.4 km (2.66 km resolution). The circulation is determined by the net diabatic heating which is calculated

from model distributions of temperature and ozone. The model includes a planetary wave parameterization which calculates wave-mean flow momentum transfer and the effects of wave dissipation. Contributors include Rayleigh friction, gravity wave drag, vertical momentum diffusion, and momentum deposition from non-linear wave breaking.

Allowing the additional volcanic aerosols to impact only the heating rates resulted in a solar heating perturbation of .1 K/day in the tropics in October 1991. For the clear sky case, the IR heating perturbation was .9 K/day, for a net heating rate perturbation of 1 K/day. For the cloudy case the IR heating contribution was negative, yielding a net cooling of .3 K/day. The maximum temperature change of 3 K occurred at 24 km between 20°S and 30°N in mid 1992. The heating perturbation also resulted in enhanced low latitude ascent and enhanced mid latitude descent from July 1991 through early 1992.

When a full chemistry-radiation perturbation was permitted to develop, the maximum temperature change at 24 km occurred in late 1991 (about 2°C increase). The altitude of the maximum decreased with time so that by late 1992, the maximum temperature change was at 18.6 km (over 2.5°C increase). At 18.6 km the maximum temperature change was between the equator and 30°S. Poleward of 60° N and S there were episodic decreases in temperature of about 2°C in the southern hemisphere and 1.5°C in the northern hemisphere. These decreases were the result of decreases in ozone. Perturbations to the circulation were not discussed for this case.

These same type of studies have been conducted related to the eruption of El Chichón (Mexico, April, 1982). El Chichón placed about a third as much sulfur dioxide gas in the tropical lower stratosphere as did Mt. Pinatubo [21]. Another major difference between the two eruptions is tied to the quasi-biennial oscillation

(QBO). When Mt. Pinatubo erupted the lower stratosphere was transitioning from the warm to cool period of the QBO. During the eruption of El Chichón, the lower stratosphere was in the cool phase of the QBO [37]. The following is a general summary of the results of the El Chichón model simulations.

Rind et al. [38] conducted a study in which the Global Climate Middle Atmosphere Model at the Goddard Institute for Space Studies was used to investigate the response of the middle atmosphere to an increase in the stratospheric aerosol burden. Part of this investigation involved including volcanic aerosol in the stratosphere and not allowing the sea surface temperature to change. It was intended that this experiment illustrate the direct stratospheric response to the additional aerosol.

The simulated volcanic aerosol parameters were based on measurements of El Chichón and Agung (Bali, March, 1963) volcanic clouds. They had an optical depth which did not vary in space or time and were assumed to be 75% H_2SO_4 by weight with a zonally-averaged distribution. After a 6 month spin-up, the model was run for 3 years.

The volcanic aerosols induced a warming in the tropical lower stratosphere between 10 and 30 km. The warming was due to the absorption of both long-wave and short-wave radiation. The annual temperature average showed a maximum increase of 2°C centered over the equator. In the middle to upper stratosphere there was a cooling of about .25 to $.5^\circ\text{C}$ in the tropics. The polar regions showed a cooling in the lower stratosphere and cooling in the middle to upper stratosphere. Maximum cooling in the polar regions was 1 to 1.5°C while the maximum warming (in the northern hemisphere) reached 4°C .

The aerosol heating directly influenced the residual circulation by increasing the equator to pole motions. The changes in temperature also indirectly affected the

circulation. There was an increase in the vertical stability which resulted in weaker Hadley and Ferrel Cell circulations. In addition, there was a relative conversion of the kinetic energy from zonal to eddy. In the low to mid stratosphere this led to an increase in standing eddy energy along with a weakening of midlatitude westerlies. The net effect was an increase in wave energy propagation toward midlatitudes in the troposphere and stratosphere.

In another 2-D study, Pitari et al. [39] investigated the effect of El Chichón on middle atmosphere circulation. The simulation began three months after the eruption and continued for one year. The maximum heating rates ranged between $.03^{\circ}/\text{day}$ and $.1^{\circ}/\text{day}$. In October, 1982, the maximum heating rates were centered slightly north of the equator near 25 km. As the simulation continued the maximum shifted toward the north pole and was located at the north pole by April, 1983. The greatest heating rates occurred one year after the eruption in April, 1983. The associated temperature perturbation ranged from 1°C to 3°C . The maximum temperature perturbation occurred in the summer and fall of 1982 and decreased in magnitude as the run continued. As with the heating anomaly, the temperature perturbation was initially centered just north of the equator at around 25 km and migrated to the north during the simulation. It was centered over the north pole by July, 1983. In addition to the temperature increase, there was a temperature decrease (about $.3^{\circ}\text{C}$) in the lower stratosphere at high latitudes. This decrease was stronger in the northern hemisphere than the southern hemisphere. One year after the eruption, a 1°C to 2°C increase persisted in the mid to high northern latitudes. The effect of this temperature perturbation on the circulation was found to be rather weak.

In an examination of the effect El Chichón had on ozone Verdecchia et al. [16] used a 2-D zonally-averaged transport model to calculate the change in ozone. As

a part of the experiment, temperature change due to volcanic aerosols were also calculated. Verdecchia et al. calculated enhanced heating of 1 K from 60°N to 45°S between 20 and 30 km. The maximum heating was 3 K and it occurred in the north tropical lower stratosphere.

Pollack et al. [40] calculated the impact of the El Chichón on the radiation budget of the northern tropics using a one dimensional (vertical) radiative-convective model. The simulation calculated the perturbations in radiative fluxes, atmospheric heating rates, and temperature for the six month period following the eruption. The aerosol cloud extended from 16 to 31 km with the peak at 28 km.

The region of the atmosphere where the cloud was located warmed due to the absorption solar and infrared radiation. The maximum heating (3.5 K) was at 24 km whereas the maximum cloud extinction was at 28 km. The warming is displaced for two reasons. The aerosols at 24 km were heated more by downwelling radiation from the volcanic cloud at higher altitudes and the background atmospheric temperature was lower at 24 km than at 28 km. Above the aerosol cloud the atmosphere cooled because less of the thermal radiation from the troposphere reached it.

The modeling studies of the radiative effects of the Pinatubo eruption are summarized in Table 2.1 and illustrate some similarities and differences between the studies. All of the studies found a net positive heating rate perturbation. These rates varied between .1 K/day and .47 K/day. The heating rate for Young et al. is approximated by Kleb based on the temperature change found by Young. The maximum in the heating enhancements were for the most part located over the equator near 24 or 25 km (within the aerosol cloud). Some notable differences concerned the relative magnitudes of the solar and infrared contributions. Pitari [14] found that the infrared contribution was negative, but this was countered by strong direct solar

Authors	Model Type	IR	Solar	Net
Young et al. [24]	3D	.18	0	.18
Pitari [14]	3D	-.2	.4	.2
Kinne et al. [13]	2 stream rad. trans.	.23-.27	.03-.08	.3
Brasseur and Granier [5]	2D	-	-	.4
Kinnison et al. [30]	2D	.27	.33	.47
Tie et al. [31]	2D	.22	.06	.28
Rosenfield et al. [33]	2D	.9	.1	1.

Table 2.1: Summary of model calculated heating rate enhancements from Mt. Pinatubo. The heating due to infrared and solar wavelengths and the net heating are given in units of K/day. A dash indicates net heating was not separated into infrared and solar contributions. The Rosenfield et al. entry is for the clear sky case.

heating and diffuse solar heating. Kinnison et al. [30] found positive infrared heating but somewhat stronger solar heating. Kinne [13] and Tie et al. [31] both found solar heating to be significantly less than infrared heating. These differences are due to the sensitivity of the calculations to processes which are difficult to model (such as cloud cover), a lack of microphysical and optical data, as well as approximations and simplifications which are necessary in any modeling endeavor. These studies show that there is sensitivity to the approximations and assumptions made and this should be kept in mind when doing similar studies or in using these results.

This dissertation attempts to expand these results in the following manner. A two dimensional general circulation model is used which is different from all but two of the studies (Young et al. and Pitari). The analysis by Young et al. does not address changes in circulation due to the enhanced heating and will be addressed here. The

model Pitari used includes the addition of the quasi-geostrophic approximation. The GCM being used in this study has no such approximation. In addition Pitari's aerosol distribution was two dimensional while this study utilizes a three dimensional heating rate enhancement. Finally in this study a tracer is included in the GCM to allow for additional analysis of circulation changes.

CHAPTER III

MODEL DESCRIPTION

3.1 Dynamics

The Langley Research Center (LaRC) general circulation model (GCM) is a spectral model which originated from the model described by Hoskins and Simmons, [41] with subsequent versions described by Grose et al., [42], Blackshear et al., [43], and Pierce et al., [44]. Conservation of mass, momentum, and energy is preserved by the following set of three dimensional primitive equations, [41]:

$$\frac{\partial \zeta}{\partial t} = \frac{1}{1 - \mu^2} \frac{\partial}{\partial \lambda} \mathcal{F}_V - \frac{\partial}{\partial \mu} \mathcal{F}_U, \quad (3.1)$$

$$\frac{\partial D}{\partial t} = \frac{1}{1 - \mu^2} \frac{\partial}{\partial \lambda} \mathcal{F}_U + \frac{\partial}{\partial \mu} \mathcal{F}_V - \nabla^2 \left(\frac{U^2 + V^2}{2(1 - \mu^2)} + \phi + \bar{T} \ln p_\star \right), \quad (3.2)$$

$$\frac{\partial T'}{\partial t} = -\frac{1}{1 - \mu^2} \frac{\partial}{\partial \lambda} (UT') - \frac{\partial}{\partial \mu} (VT') + DT' - \dot{\sigma} \frac{\partial T}{\partial \sigma} + \kappa \frac{T\omega}{p}, \quad (3.3)$$

$$\frac{\partial \ln p_\star}{\partial t} = -V \cdot \nabla \ln p_\star - D - \frac{\partial \dot{\sigma}}{\partial \sigma}, \quad (3.4)$$

$$\frac{\partial \phi}{\partial \ln \sigma} = -T, \quad (3.5)$$

where $\mathcal{F}_U = V\zeta - \dot{\sigma} \frac{\partial U}{\partial \sigma} - T' \frac{\partial \ln p_\star}{\partial \lambda}$, $\mathcal{F}_V = -U\zeta - \dot{\sigma} \frac{\partial V}{\partial \sigma} - T'(1 - \mu^2) \frac{\partial \ln p_\star}{\partial \mu}$, and $\dot{\sigma} = \frac{D\sigma}{Dt} = \frac{\partial \sigma}{\partial t} + U \cdot \nabla \sigma$.

Absolute vorticity is denoted by ζ , divergence by D , temperature by $T = \bar{T}(\sigma) + T'$, surface pressure by p_\star , geopotential by ϕ , and $\kappa = \frac{R}{C_p}$. These quantities have

been nondimensionalized using the radius of the planet, a , as the length scale, the reciprocal of the earth's angular velocity, Ω^{-1} , as the time scale, $a^2\Omega^2/R$ (where R is the gas constant) as the temperature scale, and $p_0 = 1000\text{mb}$ as the pressure scale. The vertical coordinate is σ which equals p/p_* ; λ is longitude; and $\mu = \sin \theta$, where θ is the latitude. The horizontal components of velocity are given by U and V which are the longitudinal and latitudinal velocities multiplied by $\cos \theta$.

Equations (3.1) through (3.5) describe the motion of a perfect gas surrounding a spherical, rotating planet and were derived using a few basic assumptions. The first assumption is that the fluid is inviscid or frictionless. The second is that the motion is adiabatic; a reversible process in which no heat is exchanged with the surroundings. The final assumption is that the hydrostatic relation holds [41]. The hydrostatic relation states that the gravity force is in perfect balance with the vertical component of the pressure gradient force. This relation is valid except for relatively small scale features such as a squall line or tornado.

Equations 3.1 and 3.2 are the horizontal momentum equations. The right hand side of Equation 3.1 and the first two terms on the right hand side of Equation 3.2 are horizontal advection. The third term on the right hand side of Equation 3.2 is the diffusion. Equation 3.3 is the energy equation. On the right side the first two terms are again horizontal advection. The fourth term is vertical advection and the last term represents the conversion between mechanical and thermal energy during ascent or descent. Equation 3.4 is the continuity equation and equation 3.5 is the hydrostatic relation.

The tracer equation is as follows,

$$\frac{\partial C}{\partial t} = -\nabla \cdot (VC) - \frac{\partial}{\partial \sigma}(\dot{\sigma}C) + S + D \quad (3.6)$$

where C is constituent mixing ratio and S is the source. The remaining variables are as described above. This equation is used for the tracer transport (hydrogen fluoride). A calculation of the globally integrated mass of HF at the beginning of the simulation and one year later verified that mass was conserved. There was a .2% loss of HF.

Model coverage is global with about a 2.8° resolution in longitude and latitude. Vertical coverage extends from the surface to about 95 km and is divided into 34 sigma levels. In the troposphere (below about 200mb) the levels are spaced approximately 100mb (0.1 sigma) apart. Above the troposphere the sigma levels are spaced about 3km apart (corresponding to approximately 60 mb apart near the tropopause and .003 mb apart near the top model level). Orographic forcing is approximated by using a smoothed spherical harmonic representation of the earth's topography given by the one-degree grid values from Gates and Nelson [45].

At every level in the model a biharmonic diffusion term ($\nabla^4\zeta$ for vorticity, ∇^4D for divergence, and ∇^4T for temperature) is included in the vorticity, divergence, and temperature prognostic equations to simulate sub-grid-scale diffusion and to inhibit spectral blocking (growth of amplitude at small scales in the dynamical model variables) [46], [47]. To remove large scale spurious model oscillations, Bourke [47] added a divergence dissipation term of the form $-KD$ to the divergence prognostic equation. The same technique is used in the LaRC GCM to suppress artificial oscillations on all scales [42], [43], [44].

There exists some evidence that the vertical mixing of horizontal momentum by "cumulus" friction (momentum exchange by cumulus convection) is an important process in the general circulation of the tropics (see [48] and references cited therein). Simulations showed that without cumulus friction, the amplitude of simulated trop-

ical waves was too large, e.g. [49]. Holton and Colton, [49], show that a relatively large drag coefficient is needed in the vorticity equation for the 200mb vorticity field in the tropics in the summer. Helfand concludes in his study that including cumulus friction improved the simulation of the Hadley cell, [48]. In another study by Thompson it is concluded that cumulus friction plays a minor role in the mean meridional circulation of the tropics, [50]. This investigation showed that while cumulus friction did not play an important role in their Hadley circulation, it can be important for momentum transport in the absence of horizontal eddy momentum fluxes, [50]. In the LaRC GCM the effects of cumulus friction on horizontal momentum are parameterized by including a linear damping term in the divergence and vorticity equations for the region between 10°N and 10°S between 650mb and 100mb, [43], [44].

Eddy friction within the planetary boundary layer is a significant process by which energy dissipates in the atmosphere, and thus it is an important feature to simulate in a general circulation model [51]. It has been shown that an eddy friction proportional to the square of the wind speed behaves reasonably well [51], [52]. Therefore, the same technique is used in the LaRC GCM to simulate the effects of surface drag.

Vertical diffusion of momentum and temperature are parameterized using the nonlinear, time-split technique of Williamson et al., [53]. The equations for zonal and meridional wind and temperature to be used in the diffusion calculation can be summarized follows:

$$u_k^{*n+1} - \{\bar{u}_k^{n-1}\} = a_k(u_{k+1}^{*n+1} - u_k^{*n+1}) - c_k(u_k^{*n+1} - u_{k-1}^{*n+1}), \quad (3.7)$$

$$v_k^{*n+1} - \{\bar{v}_k^{n-1}\} = a_k(v_{k+1}^{*n+1} - v_k^{*n+1}) - c_k(v_k^{*n+1} - v_{k-1}^{*n+1}), \quad (3.8)$$

$$T_k^{*n+1} - \{\bar{T}_k^{n-1}\} = a_k \left[\left(\frac{\sigma_k}{\sigma_{k+1}} \right)^\kappa T_{k+1}^{*n+1} - T_k^{*n+1} \right] - c_k \left[T_k^{*n+1} - \left(\frac{\sigma_k}{\sigma_{k-1}} \right)^\kappa T_{k-1}^{*n+1} \right], \quad (3.9)$$

where

$$a_k = \frac{2\Delta t}{\Delta\sigma_k(\sigma_{k+1} - \sigma_k)} \left(\frac{g\bar{\rho}_{k+1/2}^{n-1}}{\bar{p}_s^{n-1}} \right)^2 \bar{K}_{k+1/2}^{n-1} \quad 1 \leq k \leq K-1 \quad (3.10)$$

and

$$c_k = \frac{2\Delta t}{\Delta\sigma_k(\sigma_k - \sigma_{k-1})} \left(\frac{g\bar{\rho}_{k-1/2}^{n-1}}{\bar{p}_s^{n-1}} \right)^2 \bar{K}_{k-1/2}^{n-1} \quad 2 \leq k \leq K. \quad (3.11)$$

Since divergence and vorticity are prognostic variables in the model, the diffused velocity fields (u_k^{*n+1} and v_k^{*n+1}) are not explicitly carried. Thus, the associated diffused divergence and vorticity are not calculated either. Instead the net effects of momentum and temperature diffusion are saved for addition to the nonlinear terms in the divergence, vorticity, and energy equations [53].

Throughout most of the middle atmosphere (stratosphere and mesosphere) the coldest temperatures are at the winter pole, and the warmest temperatures at the summer pole. However, in the upper mesosphere and lower thermosphere, this temperature feature reverses and the coldest (warmest) temperatures are in the summer (winter) polar region. This temperature distribution is not in radiative equilibrium and must be maintained by dynamics. In the summer for instance, ascent of air-masses causes adiabatic cooling, and vice versa in the winter. According to Holton, both this heat budget and the momentum budget cannot be balanced without a strong zonal drag force (see discussion in [54]). The source of this zonal drag force is believed to be the wave drag produced when vertically propagating gravity waves break down near the mesopause, [54] and references cited therein. Following the technique described in [55], [56], [54], and [57], the effects of gravity waves breaking

in the mesopause region is parameterized by a Rayleigh friction term being applied to the divergence and vorticity equations. The drag term begins at about 55 km. and increases to a peak time of 0.4 days at the top model level.

3.2 Radiation

Diabatic heating is treated differently above and within the troposphere. Above about 100 mb the radiative transfer scheme of Shine, [58], [59], is employed. This radiative transfer calculation accounts for absorption of solar ultraviolet radiation by oxygen and ozone and absorption of thermal infrared radiation by carbon dioxide, ozone, and water vapor using a seasonally varying solar forcing [58].

The solar radiation calculation includes the absorption of radiation by ozone and diatomic oxygen in the region $0.175\mu\text{m}$ to $0.7\mu\text{m}$. This region is divided into six sections, covering the prominent absorption features of the two gases [58]. For most bands an effective ‘monochromatic’ parameter is specified for the calculations. Also included in the calculations are heating due to the reflection of radiation by the troposphere, the curvature of the earth for calculation of path length of solar radiation at large zenith angles, and a simplified specification of albedo as a function of latitude, [58] and references cited therein. Some notable processes which are not included are absorption in the near-infrared by water vapor and carbon dioxide as well as the effects of airglow. The near IR bands of water vapor can contribute heating equivalent to 5 to 10% of the heating from ozone in the stratosphere [58]. Shine concludes that this combined with the uncertainties in the ozone climatology and the omission of cooling due to thermal emission by some trace gases result in a tolerable error [58]. According to Shine the effects of neglecting airglow are balanced somewhat by also neglecting the additional heating due to oxygen and ozone at the

2.7 and 4.3 μm bands [58].

The thermal radiation (wavelengths greater than $4.0\mu\text{m}$) calculations include the $15.0\mu\text{m}$ bands of carbon dioxide, the $9.6\mu\text{m}$ bands of ozone and the vibration-rotation and rotation bands of water vapor. For carbon dioxide, transmittances are derived from line-by-line transmittance matrices. Atmospheric heating rates are calculated using the Curtis matrix method and departures from local thermodynamic equilibrium are also accounted for using a matrix inversion method, [58] and references cited therein.

The transmittances for the $9.6\mu\text{m}$ band of ozone are found using the Malkmus model with a simple method for including the transition from Lorentz to Doppler line shape in the middle stratosphere [58]. A major stumbling block to calculating the diabatic impact of ozone is the fact that in the GCM the stratosphere and troposphere radiation calculations are completely separate (Shine had a similar problem since his model did not have an explicit troposphere). In the cold lower stratosphere the absorption of upwelling radiation from the warm troposphere below can be an important heat source. The LaRC GCM approximates the upward flux in the same way Shine does. Using a radiation model that had a troposphere, Shine made several calculations of upwelling flux at different latitudes with a multi-level cloud. Shine found that allowing the troposphere to emit as a blackbody at the 700mb level produced about the same flux as in the multi-level cloud calculations. As a result, the zonal monthly mean 700mb temperatures interpolated from Oort, [60], are used.

A simplified approach is used for water vapor since it is the least important gas considered (for long-wave radiation) and historically not as much has been known about its mixing ratios in the middle atmosphere. Although our knowledge about water vapor mixing ratios has improved, this knowledge has not yet been used to

improve the radiation calculations. The cooling rates are calculated using an expression that is quadratic in local temperature. The coefficients are found using a full radiative transfer calculation with band model transmittances [58]

The LaRC GCM is not coupled with the LaRC CTM (chemistry/transport model). As a result, the ozone distribution, as determined by the chemistry/transport model, is not used in the radiation calculations. The same ozone climatology used by Shine is used in the LaRC GCM for radiation calculations. Shine's ozone climatology is based on two sources. Below the middle mesosphere the ozone climatology is based on balloon and SBUV (solar backscatter ultraviolet) measurements. It is the same climatology used as for first guess retrievals for the SBUV instrument, [61]. Since SBUV instrument does not have sufficient resolution in the upper mesosphere, the tabulated monthly mean data from Keating and Young are used [62] there. These data are derived from instruments on the Solar Mesosphere Explorer. Because the ozone distribution used in the radiative calculations in the GCM is not a model generated distribution, but a climatology instead, the heating enhancement will not impact the ozone distribution. In this way the heating perturbation can not feed back into the chemistry and radiation processes as it does in the real atmosphere.

Shine's model was not designed for use above .01mb (approximately 80 km). As a result, the region above 80 km is treated as a 'sponge' layer in which the mesospheric jets are artificially closed off. This is accomplished through the cooperative effects of the Rayleigh friction that is applied to the divergence and vorticity equations and by the application of diabatic heating that is proportional to the diabatic heating at 80 km multiplied by a factor ranging from 1.0 at 80 km to 0.0 at the top model level (approximately 95 km).

Diabatic heating in the troposphere (below 100 mb) is estimated by a scheme

which relies on a two-term Taylor series type expansion. The three dimensional model heating rate at model temperature, T , is given by:

$$Q(T) = Q(FGGE) + h(p) \times (T - T(\text{climatology})). \quad (3.12)$$

Here $Q(FGGE)$ is a trigonometric interpolation in time of the three dimensional heating rates obtained by Wie et al., [63]. Wie et al. calculated the diabatic heating rates from data gathered during the First GARP (Global Atmospheric Research Program) Global Experiment (FGGE). The data included global distributions of geopotential height, temperature, and zonal and meridional wind components for the period December 1, 1978 through November 30, 1979, [63]. The variable $h(p)$ is related to the Newtonian cooling coefficients given by Cunnold et al., [64] and $T(\text{climatology})$ is also a trigonometric interpolation of the climatological temperatures as reported by Randel, [65].

3.3 Numerical Techniques

The LaRC GCM uses a spectral representation in the horizontal and finite difference in the vertical, [42], [43], [44]. The prognostic variables (absolute vorticity, divergence, temperature, and geopotential) are expressed spectrally according to the spherical harmonic expansion: $X = \sum X_n^m P_n^m(\mu) e^{im\lambda}$ with triangular truncation of order 32, where P_n^m is a Legendre polynomial. Once expressed in terms of spherical harmonics, the linear terms in the horizontal equations are integrated according to the transform method described by Orszag, [66], while nonlinear terms are evaluated using the method of Eliassen, [67], [42]. The finite difference scheme of Hoskins and Simmons, [41], is employed in the vertical.

Time integration is conducted using the semi-implicit technique of Robert et al.,

[68] with a 15 minute time step. The finite difference operators are:

$$F_{\tau} = \frac{F(\tau + 1) - F(\tau - 1)}{2} \quad (3.13)$$

and

$$\bar{F}_{\tau} = \frac{F(\tau + 1) + F(\tau - 1)}{2} \quad (3.14)$$

where $\tau = \frac{t}{\Delta t}$, the dimensionless time variable, [68].

The LaRC GCM is second order accurate in time [68] and in the vertical [41]. In the horizontal since the variables are represented by surface spherical harmonics the model is exact to wave 32 (it is order T32). Waves 1 through 31 and their derivatives are represented exactly. The derivatives are calculated analytically. Wave 32 is not represented exactly since it depends on wave 33 and wave 32 is not resolved.

Initial conditions for the dynamical model were obtained from a zonally symmetric climatological wind field corresponding to northern hemisphere winter solstice conditions reported by Holton, [55] and Murgatroyd, [69]. Temperature and surface pressure fields are generated via the nonlinear balancing procedure of Hoskins and Simmons, [41], under the constraints of zero divergence and zero divergence tendency, [44]. The model was integrated for 75 model days with the seasonal parameters held at their solstice values. By this time, the effects of “initialization shock” had subsided and the dynamical state of the model at day 75 was used as the initial condition for the seasonally evolving GCM simulation. The GCM is integrated for 560 model days then initialized with hydrogen fluoride.

3.4 Model Modifications

3.4.1 Hydrogen Fluoride Initialization

Hydrogen fluoride (HF) is introduced in the LaRC GCM to enable a comparison of the impact that enhanced diabatic heating has on the model HF distribution with

the HF distribution observed by satellites. Hydrogen fluoride initialization in the LaRC GCM is accomplished through three different techniques depending on the altitude region. Between 180mb and 10mb a technique called reconstruction is used. Below 180mb, the concentration of HF is set to 0.01 ppbv, and above 10 mb zonal averages of HALOE HF data are used. Although every effort was made to achieve the best initialization possible, outside the reconstruction area, the methods employed were fairly crude. This is not expected to adversely impact the results since the GCM is integrated sufficiently to allow the tracer field to align with model dynamics. HF is transported as an inert tracer by the GCM according to Equation 3.6.

The technique of reconstruction was first described by Schoeberl et al., [70]. This involves the use of conservative coordinates - air parcel tags which do not vary or vary very little under the motion of the parcel. To do this, the data are transformed into conservative coordinates and accumulated. Once enough data is accumulated it can be transformed back into physical space at any location (hence ‘reconstruction’) [71]. The air parcel tags or tracers can be any conserved scalar quantity. For practical purposes, any tracer with a relatively long lifetime can be used to remove the meteorological variability yet still retain enough vertical and latitudinal variability to be used as a conservative coordinate for the same period of time [71]. In the stratosphere, chemical tracers such as CH_4 , CO_2 , and chlorofluorocarbons can be used as conservative coordinates as well as the dynamical quantities, potential vorticity and potential temperature. Potential vorticity and potential temperature work best over short periods (a week to a month) when friction and diabatic processes are negligible, however corrections for diabatic drift can be made [71]. The following procedure was used in applying this technique to initialization of HF in the LaRC GCM.

The first step was to gather HF and potential vorticity data. Potential vorticity and HF are expected to have a coherent relationship since both are tracer quantities and thus should illustrate the effects of atmospheric motions. data is that measured by the HALOE instrument [23] and the isentropic (surfaces of constant potential temperature) potential vorticity (PV) data is that derived from meteorological data in the European Center for Medium-range Weather Forecast (ECMWF) database. The only ECMWF data available corresponded to the dates of the Airborne Southern Hemispheric Ozone Experiment / Measurements for Assessing the Effects of Stratospheric Aircraft (ASHOE/MAESA) missions. These missions occurred in 1994 at the following times: March 24 through April 9, May 17 through June 9, July 24 through August 10, and September 26 through October 21. The measurements of the meteorological variables used to derive isentropic potential vorticity and the HALOE occultation within 24 hours of one another. Depending on the date, the PV data was calculated at either five pressure levels (150 mb, 100 mb, 70 mb, 50 mb, and 30 mb) or seven pressure levels (includes two additional levels, 200mb and 10 mb). The PV data was smoothed to remove high frequency noise, while still retaining important meteorological features. The HF data used in the reconstruction and the reconstruction itself was therefore limited to the altitude range of the potential vorticity data. The PV data was then interpolated to the same locations in space and time as the HF data. Note that even though this data spans several months (and even seasons) it is used to initialize HF in the GCM in early July. This is to ensure a wide range of PV values.

Once the ECMWF isentropic potential vorticity has been interpolated to the location of the HALOE hydrogen fluoride, they can be plotted in order to elucidate a relationship between the two. The goal is to initialize the LaRC GCM, therefore

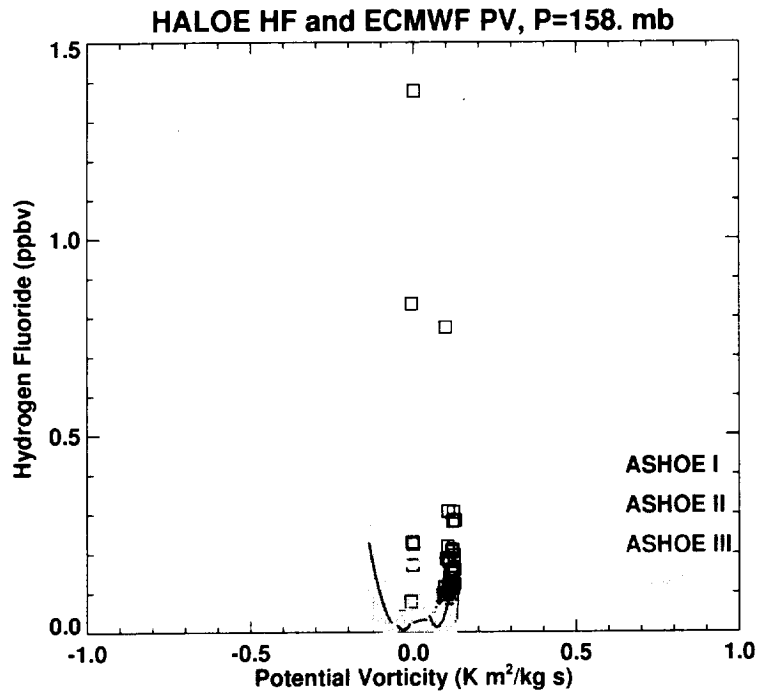


Figure 3.1: HALOE hydrogen fluoride in ppbv versus ECMWF isentropic potential vorticity in $\frac{\text{K m}^2}{\text{kg s}}$ at the 158 mb pressure level. The solid lines are polynomial fits to segments of the data.

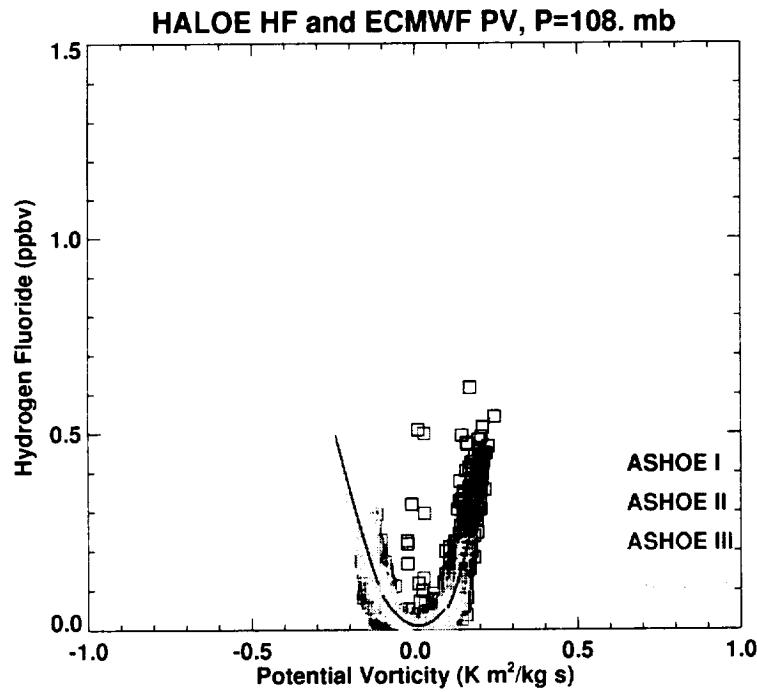


Figure 3.2: Same as in Figure 3.1 but at the 108 mb pressure level.

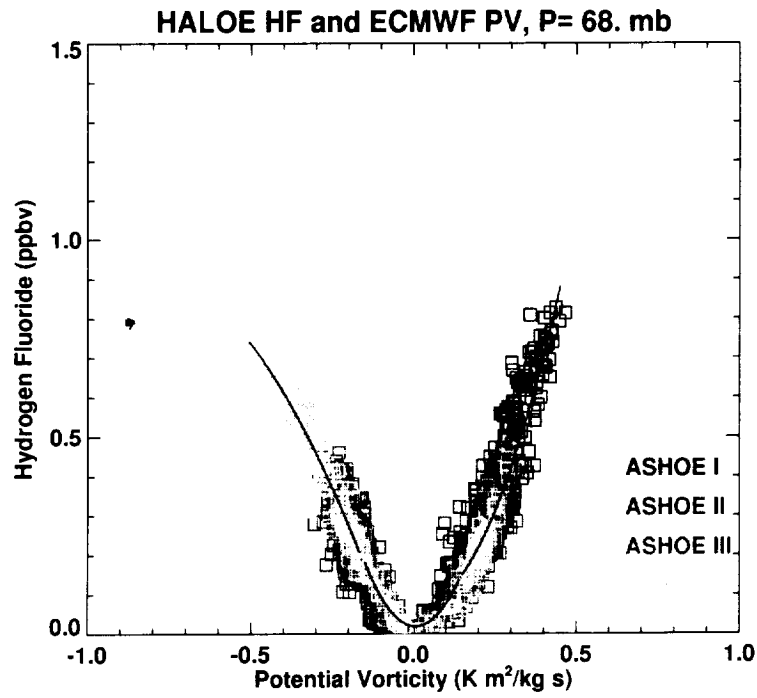


Figure 3.3: Same as in Figure 3.1 but at the 68 mb pressure level.

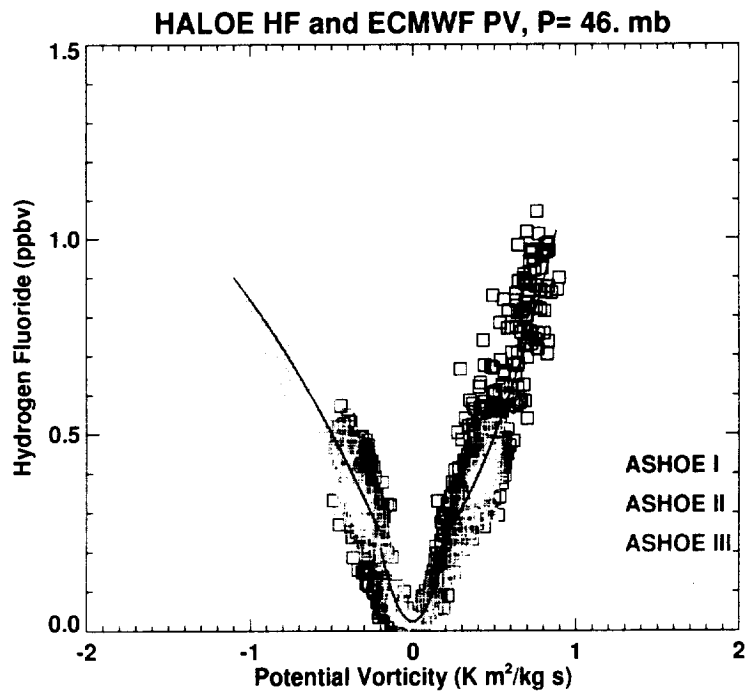


Figure 3.4: Same as in Figure 3.1 but at the 46 mb pressure level.

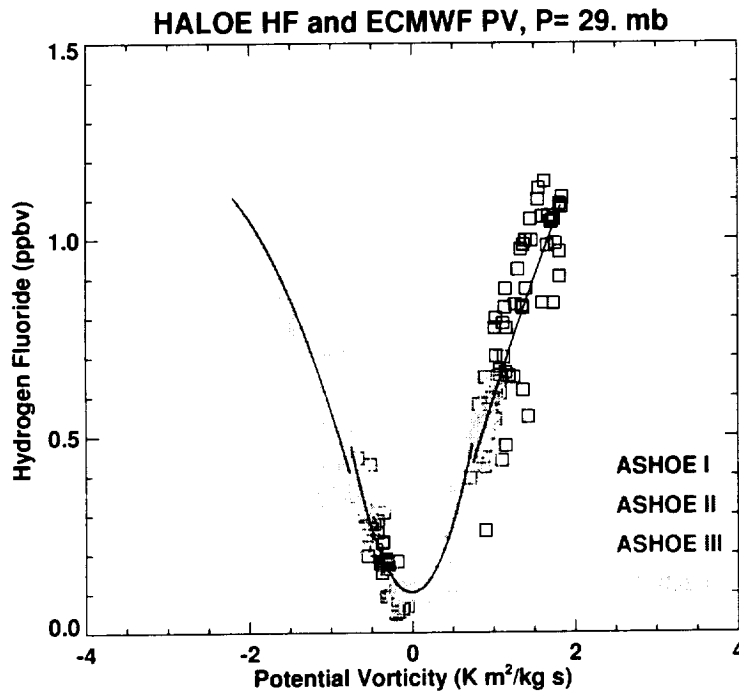


Figure 3.5: Same as in Figure 3.1 but at the 29 mb pressure level.

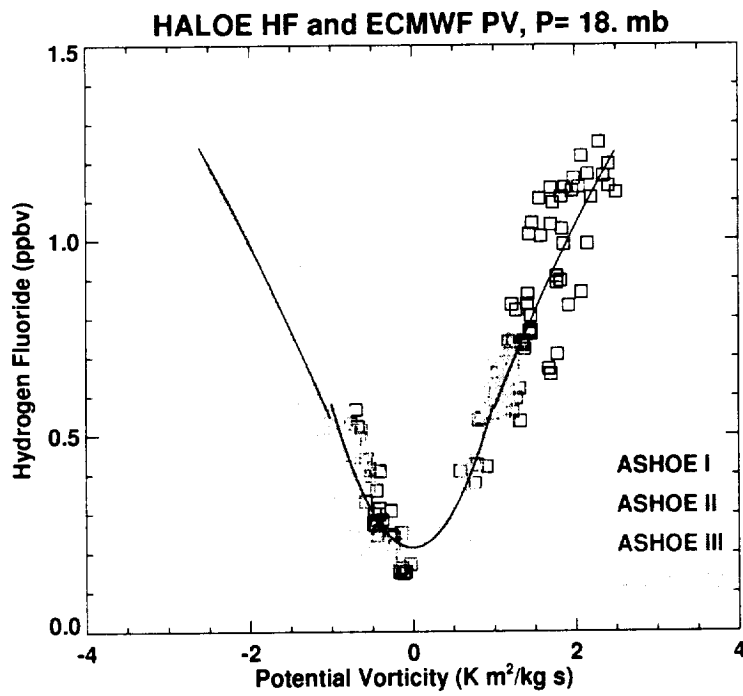


Figure 3.6: Same as in Figure 3.1 but at the 19 mb pressure level.

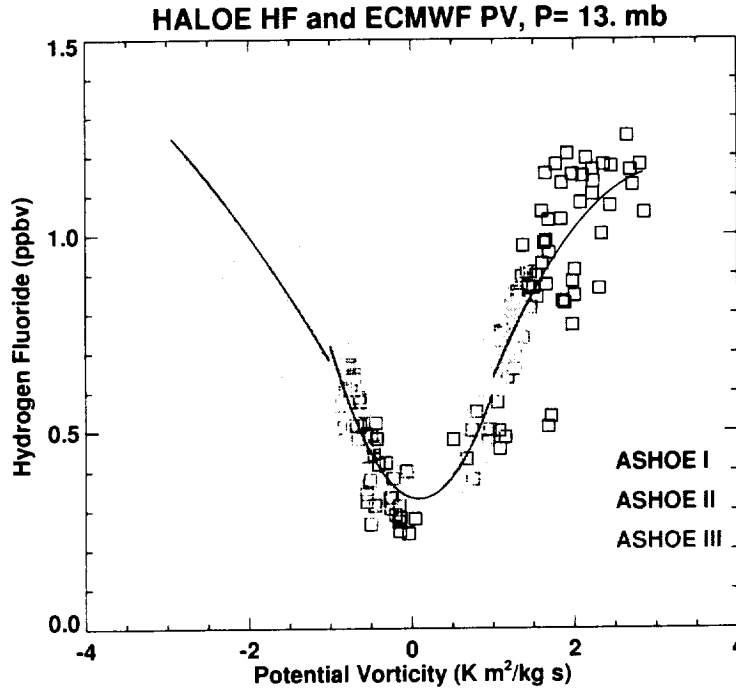


Figure 3.7: Same as in Figure 3.1 but at the 13 mb pressure level.

only the HF pressure levels (and after interpolation, the PV pressure levels too) nearest the GCM pressure levels are used. At each pressure level, all data points are plotted on a scatter plot as in Figures 3.1 through 3.7. The data at each pressure level is then divided into regions according to potential vorticity values. These regions each have a unique polynomial fit to allow for the best polynomial fit possible for the entire data set at that pressure level. As an example, in Figure 3.2 for curve fitting, the data is separated into three regions, PV data less than $-0.1 \frac{Km^2}{kgs}$, PV data between $-0.1 \frac{Km^2}{kgs}$ and $.1 \frac{Km^2}{kgs}$, and PV data greater than $0.1 \frac{Km^2}{kgs}$, each with a different curve fit. The abnormally high values in HF near 0 PV in Figures 3.1 and 3.2 are the result of interfering clouds and are ignored in the polynomial fit.

The curve fits become the means to reconstruct HF in the GCM, using model potential vorticity. For each segment of polynomial at the seven pressure levels there is a different function describing HF in terms of PV ($HF=fcn(PV)$). In the GCM

potential vorticity is known globally and can be used to define HF globally with the use of the functions derived from the observational HF and PV.

As stated earlier, the method of reconstruction can only be used for seven of the 34 model levels due to the limited vertical coverage of the ECMWF potential vorticity. Above and below the reconstruction area different methods were employed to initialize HF. For all model levels below the lowest reconstruction level (pressure greater than 180 mb), model HF is set to .01 ppbv. This simple method is used since HF values drop off dramatically as altitude decreases.

Above the highest reconstruction level (approximately 10 mb) a more complex method is utilized for HF initialization. The same HALOE HF data employed in the reconstruction is sorted into latitude bins. The vertical profiles are each at a different latitude and longitude. In fact the data points within a sounding are all at slightly different geographical locations since the occultation measurement is not instantaneous. All the profiles within a latitude band are then averaged over longitude. The result is two vertical profiles per latitude region, one for sunrise and one for sunset. Initially there were 18 latitude bins which were 10° wide swaths (e.g. 79°N to 70°N , 69°N to 60°N , 59°N to 50°N , etc.). The averaged vertical profiles for certain latitude bands were similar enough to allow some of the bands to be combined forming larger swaths. Since this method of extending the HF initialization upward of 10 mb is fairly crude anyway, some enlargement of the bin size is not expected to significantly impact the experiment. The number of latitude bins was reduced to four: the equatorial region (19°S to 19°N), southern midlatitudes (20°S to 39°S), northern midlatitudes (20°N to 39°N), and the high latitudes and polar regions (40°N to 79°N and 40°S to 79°S).

After averaging the vertical profiles, a second degree polynomial is fit to the two

(sunrise and sunset) curves above 10 mb. In the equatorial region, one polynomial fit could be used for the entire region above 10mb. For the other three latitude regions, a closer approximation to the vertical profiles could be achieved if the profiles were separated into two altitude regions and each altitude region had a separate polynomial fit. These polynomials define the HF mixing ratio above 10 mb. Note that in this region there is no variation in longitude and minimal variation in latitude.

The three initializations methods described above were then combined to create a three-dimensional grid of HF mixing ratio. The three dimensional grid was smoothed using a five-point boxcar average. This ensured a smooth transition between the various initialization regions, and within those regions since some were subdivided. The smoothed three-dimensional grid of HF values was read into the GCM and transformed to spectral coefficients for model integration.

The GCM is initialized with hydrogen fluoride in early July of the second model year (the end point of the GCM integration described in Section 3.3). The model is integrated for another year to allow the tracer field (HF) to align with model dynamics. The tracer must be related to the model dynamics since the dynamics are responsible for modulating tracer distribution. This is especially important above and below the reconstruction region where the initialization techniques are independent of model dynamics. Since the reconstruction technique relates HF to model potential vorticity, in that region the HF distribution is fairly closely tied to the GCM dynamics through potential vorticity.

A one year simulation was completed. Since there were no sources for HF during the simulation, the mixing ratio in the upper stratosphere began to dissipate. As the simulation progressed, the region of low HF mixing ratios propagated downwards. The effect of this can be seen in a comparison of the zonal mean HF distribution two

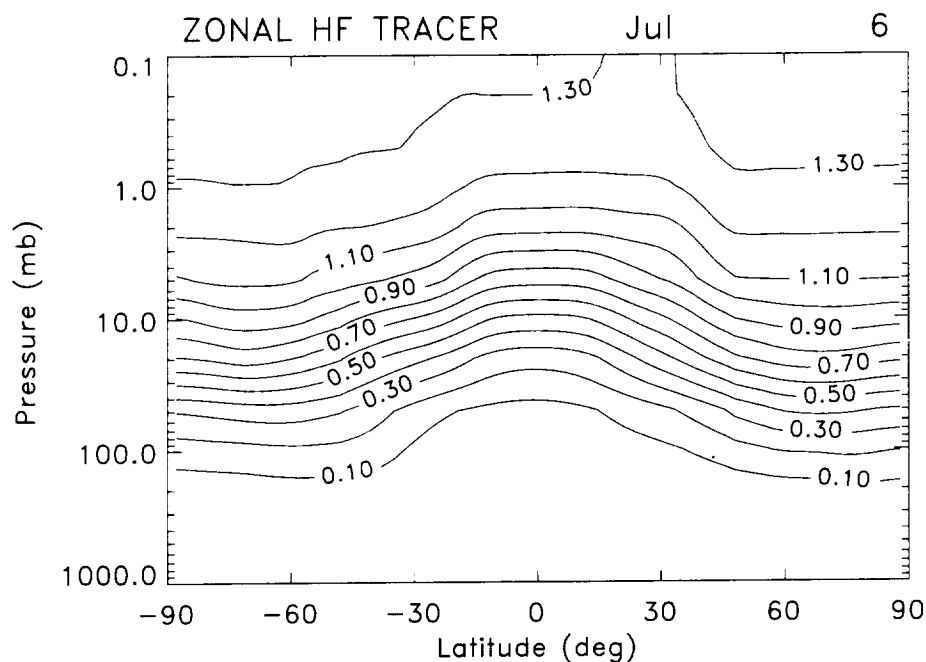


Figure 3.8: Zonal mean hydrogen fluoride (ppbv) on model day July 6, two model days after model initialization.

days after initialization and in mid June, after almost one year of simulation.

Figures 3.8 and 3.9 illustrate the changes in the HF distribution during the year-long integration. Notice that in Figure 3.8, just after the model is initialized, there is no evidence of subsidence in the southern polar region, as would normally be expected. The subsidence, however, is present in Figure 3.9. This is a result of the manner in which HF was initialized in the model. The subsidence is mainly above 10 mb as shown in Figure 3.9. Recall that this region was initialized using an average vertical profile for a latitude swath. In this case it was the same profile for 40° to 70° north and south. As a result, the subsidence normally expected in the high latitude southern hemisphere is not present in the tracer at the time of initialization. After the tracer was given a year to adjust to model dynamics, the subsidence is present as shown in Figure 3.9.

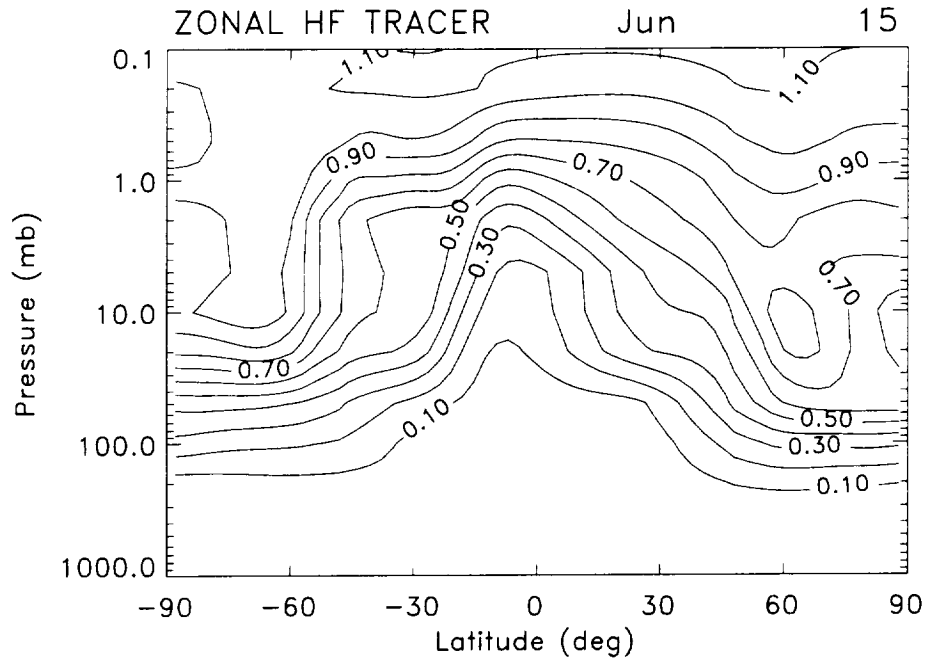


Figure 3.9: Zonal mean hydrogen fluoride (ppbv) on model day June 15, almost one year after model initialization.

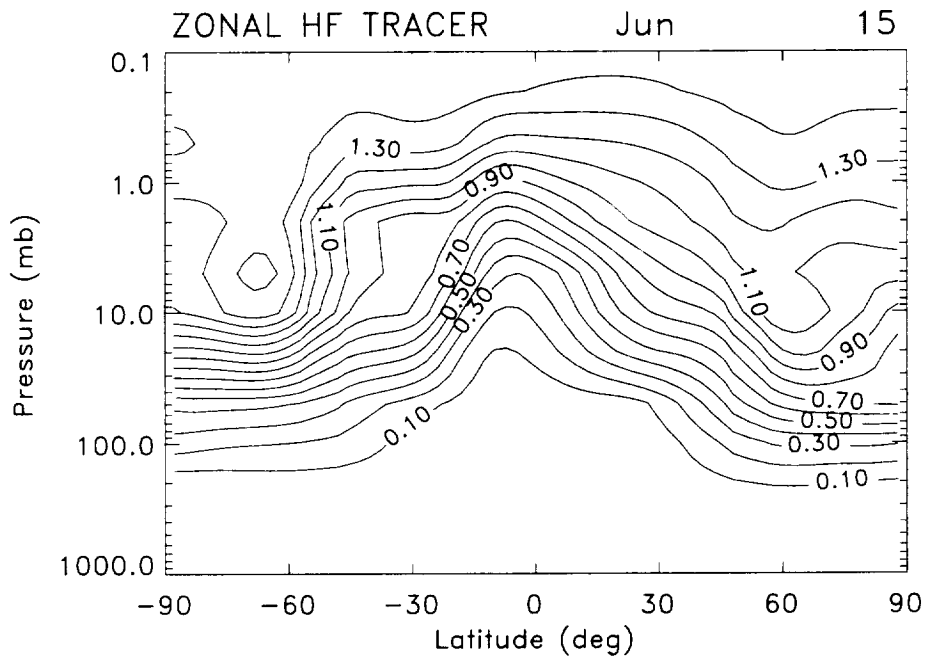


Figure 3.10: Corrected zonal mean hydrogen fluoride (ppbv) on model day June 15, almost one year after model initialization.

The dissipation of HF at higher levels is also illustrated in these two figures. In Figure 3.8 HF mixing ratios are about 1.3 ppbv or higher above 1 mb. By June 15 these mixing ratios drop to between 0.9 and 1.1 ppbv above 1 mb, as seen in Figure 3.9. As discussed above, this is a result of not having a chemical source for HF in the GCM. In order to counteract the dissipation of HF, an artificial source for HF is included. This source is found by plotting the first spectral coefficient of the tracer variable (HF) versus time for the year long simulation at each model level. The first spectral coefficient is equivalent to the zonal mean and this enables an examination of the time trend in the zonal mean at all model levels. As suspected, this trend is negative for most model levels. Next a straight line is fit to each time trend curve. The nondimensionalized negative of this slope is added to the tendency equation for HF before HF is updated. Appendix A lists the values added to the HF tendency equation at each model level. In the real atmosphere the stratospheric source for HF is CFC's however there is no appreciable chemical loss [3]. The hydrogen fluoride distribution in the real atmosphere is therefore basically determined by surface emission of fluorine containing gases, photochemical destruction of these gases, and dynamics [3]. The 'sources' listed in Appendix A are not intended to simulate the sources in the real atmosphere, but rather to prevent the dissipation of HF in the stratosphere as illustrated in previous figures. The year long simulation is then rerun with this 'source' for HF included. The impact of this correction can be seen in Figure 3.10. Including the correction for HF in the model did not impact the structure of the HF distribution, but it did impact the levels of HF. Near .1 mb in Figure 3.9 HF has a value of about 1.1 ppbv (compared to 1.3 when initialized as seen in Figure 3.8). However, after including a crude source term, and rerunning the year long adjustment period, the value of HF at .1 mb about 1.35 ppbv (Figure 3.10). Instead of

a .2 ppbv decrease there is a .05 ppbv increase in HF at .1 mb. It is possible that the source term was a bit too large, however further refining of the source is not attempted since the HF distribution is considered reasonable.

3.4.2 Diabatic Heating Perturbation

The heating rate enhancement was selected based on the geographical coverage and temporal evolution of the aerosol cloud from which the heating rates are calculated so that the large scale features agree reasonably well with observations. In addition the radiative transfer calculations should be on par with other similar studies. Since the purpose of this study is to study the effect of the heating enhancement due to the volcanic aerosols only, other processes which could impact the heating rates are not included (such as changes in ozone). Brasseur and Granier [5] calculate a 5.6% decrease in ozone over the equator at 25 km. Since at that altitude the total contribution to the heating by absorption of radiation by oxygen and ozone is about 1 K/day [3], a 5.6% change is not expected to impact these results.

The heating enhancement data included in the LaRC model conforms to these standards and is the product of three computational models from NASA Ames Research Center described briefly in Chapter II, [24]. The three models used to create the heating enhancement were a three dimensional primitive equation circulation model, [72], a three dimensional microphysical/transport model, [73], and a radiative transfer model, [74]. The transport model was run off line with wind and temperature fields produced by the circulation model.

The circulation model had 26 equally spaced pressure levels with approximately a 2 km resolution. The lowest level was at 300 mb, highest level at .2 mb. The uppermost levels contained a sponge layer to prevent reflection of wave energy back

into the model domain. National Meteorological Center (NMC) 24 hour analyses at the appropriate times were used to derive geopotentials at 300 mb which provided the dynamic forcing for the rest of the model. Spectral representation to zonal wave number 6 were computed from the NMC 2.5° grid analyses. For each zonal wave number the meridional variations were represented by 25 Legendre functions.

NMC zonally averaged tropospheric temperatures and model derived stratospheric temperatures were used to compute radiative exchange between the stratosphere and troposphere. Climatological water vapor distribution from NMC and ozone distribution from McPeters et al. [75] were used in the radiative transfer model. The time integration of the circulation was started from balanced winds and temperatures on June 1, 1991.

Injection of the volcanic plume as a uniform concentration occurred between model levels corresponding to 22 and 26 km. Twenty megatons of SO_2 were injected which and were eventually converted to about 40 megatons of H_2SO_4 . The microphysical model did not compute coagulation, sedimentation, or nucleation. Sedimentation should be unimportant during the first few months following the eruption since the particle sizes were small. A cloud layer with a large optical depth was assumed at the 700 mb level to prevent overestimation of aerosol heating. The cloud optical depth was a Gaussian centered at 5° with a width of 15° and a peak value of 3. This parameterization was based on the zonal average of the emitted longwave flux from analysis of satellite data (see [24] and references cited within). The heating of the aerosol cloud was allowed to feed back into the circulation. Following the results of Kinne who found solar heating of the aerosol plume to be negligible [13], only longwave heating of the aerosol cloud was calculated.

Daily averages of the three-dimensional enhanced heating rate distribution from

the Ames GCM are used as input into the LaRC 3-D GCM to simulate the additional heating resulting from the Mt. Pinatubo eruption. The heating rates are in units of Kelvin per day and represent the additional heating produced by the volcanic aerosol only. The heating rate distribution is interpolated to the LaRC grid, then read into the simulation and updated once per day beginning June 15. The simulation ends at the end of December due to limitations in the microphysical model which yield unreliable results after December.

A comparison of the aerosol distribution from the Ames model simulation and the actual aerosol distribution as measured by the Stratosphere Aerosol and Gas Experiment (SAGE) II, [76] has been made to determine how closely the model simulation replicates the actual distribution. First a comparison in latitude and longitude is made and then a zonal comparison is discussed.

The comparison in latitude and longitude is done using different forms of aerosol data. The SAGE II data is the extinction ratio taken at the 750 K surface, while the modeled aerosol data (from Ames) is total column density. In addition, SAGE II data covers a range of days (about a month) to achieve near global coverage while the modeled data is taken as a snapshot on specific days. Since more consistent data was not available for a precise comparison, and the limitations of the SAGE II data (with respect to synoptic snapshots) is unavoidable, this comparison is to evaluate the large scale features of the aerosol distribution.

Both the simulated Pinatubo plume and the actual plume exhibit the same general features. The SAGE II aerosol distribution encircled the earth within two weeks of the eruption, [21] while the simulated aerosol distribution took 20 days. During this time the aerosol cloud remained bounded between 30°N and 20°S for both the SAGE II and the modeled plume, [21]. In mid July SAGE II measurements show

regions of high aerosol concentration over the Atlantic Ocean and over southern and eastern Asia, [76]. These features are also apparent in the simulated aerosol distribution, however the region of enhanced aerosol levels over the Atlantic Ocean is more extensive in the simulation. SAGE II data also shows a protrusion of enhanced aerosol levels in the southern Atlantic across the southern tip of Africa and east to about 90°E and south to between 40°S and 45°S , [76]. The simulated plume exhibits a similar protrusion, however it only extends eastward to about 45°E and southward to 30°S . In addition, in early July SAGE II data shows relatively low levels of aerosol to the north of 10°N from the east coast of the United States eastward past India. By mid July this region is dominated by high aerosol levels, especially over Africa. By comparison, the modeled aerosol coverage on July 4 shows low values of aerosol over eastern Africa and eastward to Indonesia and the Philippines (farther east than SAGE II observed). While the latitudinal coverage of the SAGE II and simulated aerosol clouds was consistent, transient synoptic features observed by SAGE II were not accurately reproduced in the Ames simulation.

A comparison of the zonal distributions shows the two aerosol clouds exhibiting similar general features as well. During July, both the simulated plume and the SAGE II plume have a maximum over the equator, SAGE II maximum at 21 km and the simulated plume maximum at about 23 km. In the SAGE II zonal plots, several SAGE II profiles were truncated in the stratosphere due to the optically thick volcanic plume. Because of this, the altitude of the plume maximum was estimated from lidar measurements, [76]. Both the simulated plume and the plume observed by SAGE II extend from about 15°S to 30°N . Poleward of 15°N the altitude of the maximum of the modeled plume is at a lower altitude than over the equator (23 km at the equator and about 20 km at 20°N). This trend is also apparent in the SAGE

II data, with the region of high aerosol levels decreasing in altitude north of the equator, [76].

In the late August and September time period, above the equator the maximum remains at about 26 km for both the modeled and SAGE II distributions. However, at 15°N the maximum of the SAGE II plume is lower in altitude, near 23 km. The modeled distribution does not show such an obvious difference with the maximum between 24 and 25 km. For both distributions, the top of the plume is at about 32 km, [76]. In addition, by the end of September, the SAGE II aerosol distribution reaches as far south as 50°S, while the simulated distribution extends to about 35°S.

For the October and early November comparison, both the SAGE II and the simulated distributions have a maximum over the equator at about 26 km. The SAGE II data still shows a more severe decrease in altitude northward than the modeled data. At 15°N the SAGE II maximum is 2 to 2.5 km lower, while for the modeled data it is a 1 km or less difference. There is fairly good agreement on the location of the top of the plume, both distributions are near 32 km. The plume has greater latitudinal coverage in the SAGE II data than is simulated in the Ames model. SAGE II data shows relatively high levels of aerosol from about 60°S to 50°N, [76]. The modeled plume extends from about 35°S to 50°N.

In general there is reasonable agreement between the modeled aerosol distribution and the aerosol distribution measured by SAGE II for the large scale features. There are some discrepancies, however, the most serious being the failure of the modeled plume to descend in altitude north of the equator. Both distributions agree fairly well in latitudinal coverage, however the SAGE II data shows the plume extending somewhat farther south than was simulated. In attempting to calculate the additional diabatic heating from Mt. Pinatubo there are several uncertainties that

could potentially have a greater impact on the calculation of the diabatic heating enhancement (such as the importance of the contribution to the heating due to solar radiation and other uncertainties in radiative and microphysical properties as well as approximations made for computational reasons). Since the goal was to include a heating enhancement with reasonable large scale features (temporal and geographical) and this dataset fulfills those requirements, the heating enhancement is deemed acceptable to simulate the large scale circulation effects of the Mt. Pinatubo eruption.

3.5 Summary

The LaRC GCM is a version of the model described by Grose et al., [42], and Blackshear et al., [43]. It is a three dimensional spectral primitive equation model in sigma coordinates. There are 34 vertical levels extending from the surface of the earth to approximately 95 km (top 15 kilometers are a ‘sponge’ layer). Horizontal coverage is global with 2.8° resolution in longitude and latitude. Above 100 mb (about 16 km) the radiative transfer scheme of Shine is used which includes the effects of water, ozone, and carbon dioxide for both solar and long wave radiation. Below 100 mb the diabatic heating is estimated using a climatology derived from data from the First GARP (Global Atmospheric Research Program) Global Experiment (FGGE). Horizontal representation of prognostic variables is spectral and vertical representation is finite difference. Time integration is a semi implicit method with a 15 minute time step.

Two changes are made to the GCM. A hydrogen fluoride tracer is initialized in the GCM. The purpose of this tracer is to use it to investigate possible changes in the circulation resulting from the eruption of Mt. Pinatubo. The HF distribution

is based on version 17 HALOE data and ECMWF isentropic potential vorticity. An ad hoc source term for HF is added to improve the HF distribution. The second modification is the addition of a diabatic heating enhancement. A three dimensional distribution of the heating enhancement (K/day) due only to the Pinatubo aerosols is provided by Ames Research Center.

CHAPTER IV

COMPARISON OF MODELED HYDROGEN FLUORIDE DISTRIBUTION WITH OBSERVED HYDROGEN FLUORIDE DISTRIBUTION

This chapter is devoted to an evaluation of the LaRC GCM hydrogen fluoride distribution. Hydrogen fluoride is included as an inert tracer so that changes in HF which occur as a result of the heating enhancement in the model simulation can be compared to changes in HF which were observed by HALOE. These changes can then be used to study changes in the circulation. As mentioned earlier, this distribution was initialized in early July, then allowed to adjust to model dynamics for one year. The following data is taken from the second year of the simulation (with correction) and is the control HF distribution which will be compared to the HF distribution perturbed by the Mount Pinatubo eruption.

To evaluate the unperturbed HF distribution in the model, summer and winter comparisons of model HF and HALOE HF are examined for both the zonal distribution and vertical profiles at selected latitudes. For the zonal comparisons, 1994 HALOE data is used and for the vertical profile comparisons, 1993, 1994, and 1995 HALOE data is used. Since the HALOE measurements were not at exactly the same locations and times in 1993, 1994, and 1995, it was decided to only use the 1994 data

for the zonal comparison. Recall that the HALOE data used to initialize the model was the 1994 data.

For version 17 of the HALOE dataset (the version used in this dissertation), HALOE precision is between .04 ppbv and .06 ppbv throughout the stratosphere [77]. The total error varies according to pressure level. At 1 mb, 3 mb, and 10mb the error is 15%. At 5 mb the total error is 14%. There is an error of 18% at 30 mb, 21% at 50 mb and 27% error at 100 mb [77].

4.1 Zonal Comparison

The HALOE profiles used in the zonal plots are averages of all the events (vertical profiles) taken for that occultation. Typically 15 vertical profiles are measured which range over less than 1 degree in latitude near the poles to around 5 degrees in latitude near the equator. To obtain model data with a similar temporal sampling as the HALOE data, daily zonal averages of model data are calculated. Next, the model latitude nearest the location of the sunrise HALOE occultation on that particular day is selected. This is repeated for all days in each seasonal HALOE dataset (for example, July 4 through August 20 for the summertime).

For all the zonal plots, HALOE HF data is at sunrise, while the model data is near midnight. This should not impact the comparisons since HF has no significant diurnal variation.

4.1.1 July

The July/August HALOE hydrogen fluoride distribution is shown in Figure 4.1 and summertime model hydrogen fluoride distribution is shown in Figure 4.2. Figure 4.3 is the fractional difference between the HALOE and LaRC GCM HF distributions. The very high values for HALOE HF in the tropical northern latitudes

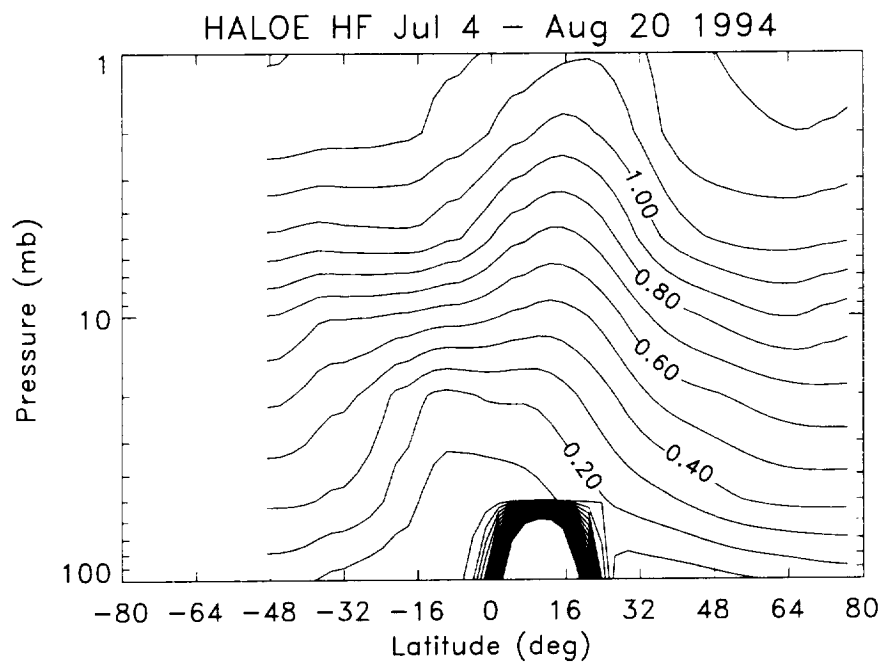


Figure 4.1: Sunrise HALOE hydrogen fluoride (HF) distribution, July 4 through August 20, 1994. Contour levels are in parts per billion by volume (ppbv).

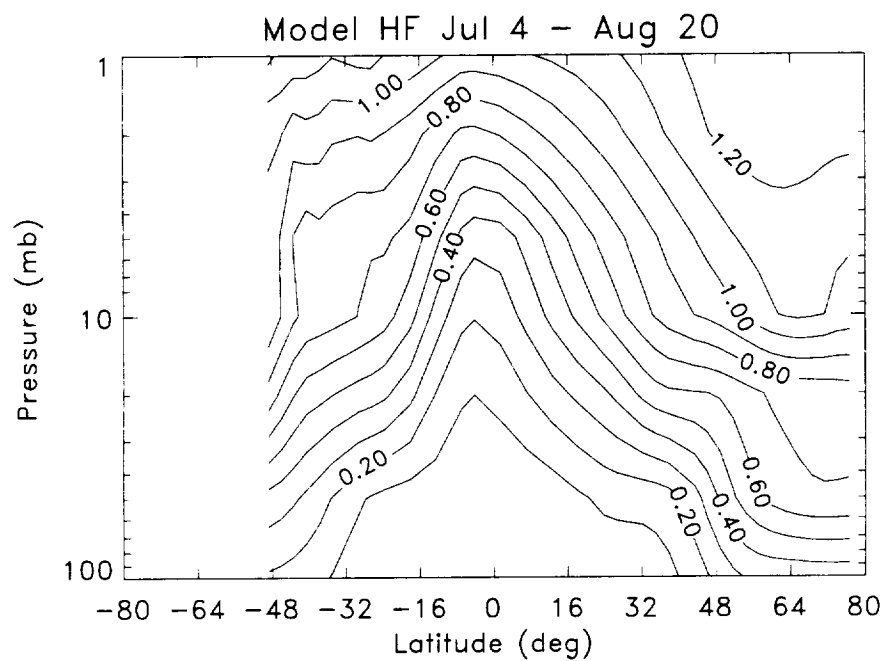


Figure 4.2: Summertime LaRC GCM HF distribution.

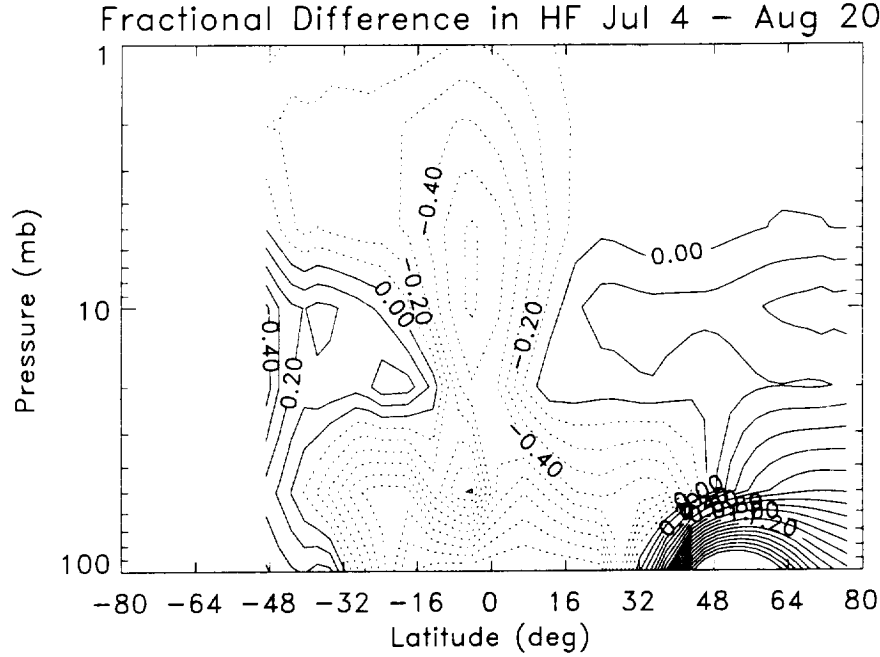


Figure 4.3: Fractional difference divided by 100 between HALOE and model HF distributions for the July-August time period. Dashed (negative) contours indicate model values lower than HALOE values, solid (positive) contours indicate model values higher than HALOE values.

between 50 mb and 100 mb are due to cloud interference.

The general features of Figures 4.1 and 4.2 are similar. Both HALOE and the model show a ridge of HF near the equator, with decreasing values to the north and south of the ridge. Poleward of 32°N both HALOE and LaRC data decrease at all pressure levels, then increase slightly at high latitudes above 20 mb. The LaRC data however, decreases more sharply than the HALOE data and not as uniformly. The HALOE data shows a second, smaller peak below 20mb at tropical latitudes, approximately centered over the equator. This feature is not present in the model data.

South of 16°S and below 20 mb, both HALOE HF values and LaRC HF values decrease toward the pole. Above 20 mb in the same latitude region HALOE values

remain mostly constant with latitude. The LaRC HF levels have more variability, but still decrease gradually toward the pole until about 48°S where they begin to drop precipitously.

Figure 4.3 depicts the fractional difference (percent difference divided by 100) between the HALOE HF distribution and the LaRC GCM HF distribution. For example a value of .2 indicates a 20% difference. Positive contours (solid lines) indicate model values greater than HALOE values and negative contours (dashed lines) indicate model values less than HALOE values. In general fractional differences less than 30% are considered acceptable since HALOE total error ranges between 15% and 27% depending on pressure level.

The differences between the two HF distributions are more clearly illustrated here. Model HF values are lower than HALOE values over all relevant pressure levels in the equatorial region. Below about 25 mb model values are significantly lower than HALOE values (by more than 100% at some pressure levels) from about 40°S to 40°N. Between about 25mb and 5mb model values are lower than HALOE values in tropical latitudes, and higher than HALOE values poleward of that, both to the north and south by as much as 40%.

The biggest difference between model and HALOE distributions is below 50mb, poleward of 32°N. This is due to the fact that HF isopleths from the model decrease faster toward the pole than the isopleths from HALOE. Changes of the same magnitude as at higher pressure levels on relatively low HF values result in a larger percent change than at higher altitudes where HF values are greater.

Although the two HF distributions appeared qualitatively similar, it is clear that quantitatively they are quite different. There is some interannual variability in the HALOE HF data, and the model does not attempt to replicate the circulation pat-

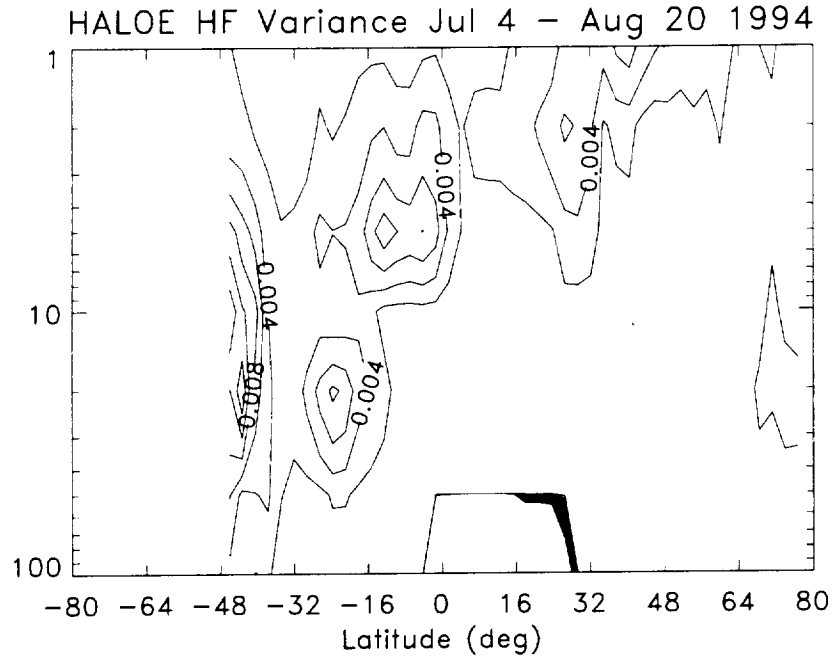


Figure 4.4: Longitudinal variance in HALOE HF distribution for the time period July 4 through August 20, 1994.

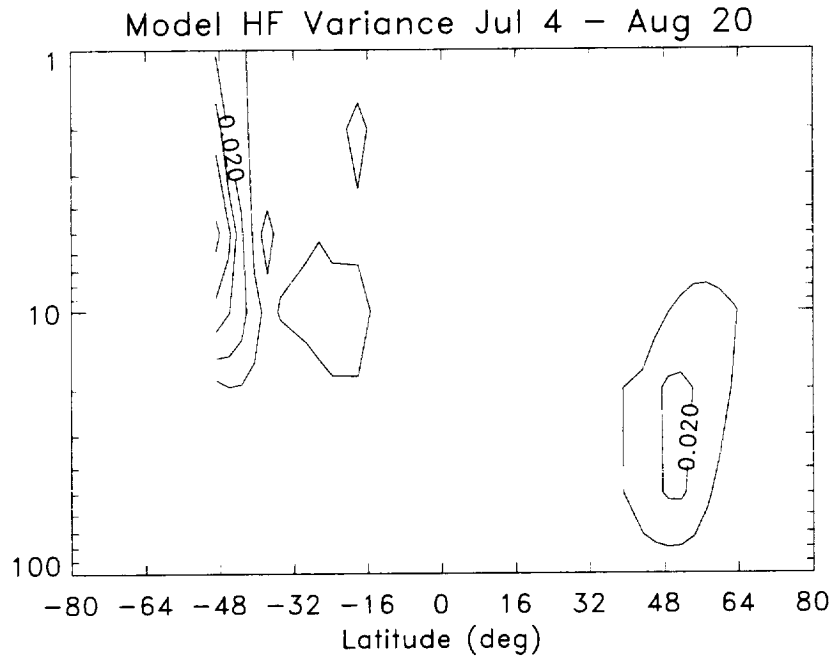


Figure 4.5: Longitudinal variance in MODEL HF distribution for the time period July 4 through August 20.

terns that were present in the real atmosphere in 1994. Even with these considerations, the differences are larger than can be explained by interannual variability in the model or HALOE data. In addition, over the course of a one year simulation, the globally integrated value of HF decreased by only .2%, so that these differences are not due to loss of HF in the model simulation. However, these differences can largely be explained by examining model and HALOE HF variance and the vertical component of the diabatic circulation. The vertical component of the diabatic circulation is derived from the model parameters and also from UKMO (United Kingdom Meteorological Office) data corresponding to the dates of the HALOE measurements. Model data is sampled the same way HALOE sampled the atmosphere, as was described previously. In this way the vertical component of the diabatic circulation in the LaRC GCM can be compared to the actual atmospheric quantity.

Figures 4.4 and 4.5 illustrate HALOE and model longitudinal (or wave) variances in HF. At low latitudes between 1 mb and 4 mb HALOE HF variance is greater than the variance in model HF. This indicates that more wave activity was present in the real atmosphere than was simulated in the model in that region. The effect of enhanced wave activity in the HALOE data can be seen in the HF distributions (Figures 4.1 and 4.2). Model HF contours have a sharper peak in the equatorial region than the HALOE HF contours. The HALOE HF contours are flatter because the enhanced wave activity allowed for more mixing.

At 48°N between 80 mb and 8mb and near 48°S above 20 mb model variance is greater than HALOE variance. Hence, there is more wave activity in model HF than in HALOE HF. The differences in the wave activity are related to the differences observed in the zonal distributions of HF (Figure 4.3) near 10 mb at extra-tropical latitudes.

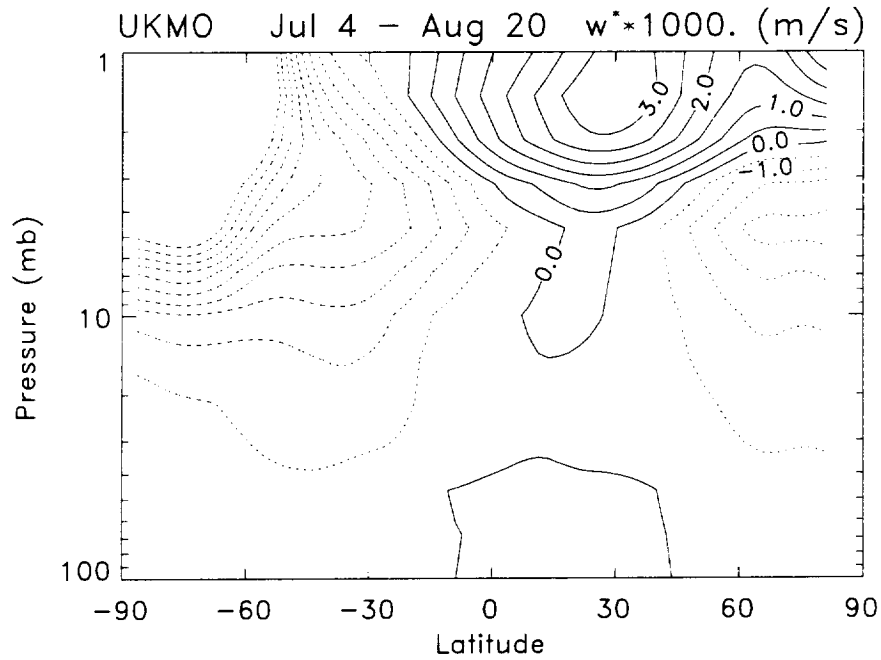


Figure 4.6: Vertical component of the diabatic circulation calculated from UKMO data for the time period July 4 through August 20, 1994.

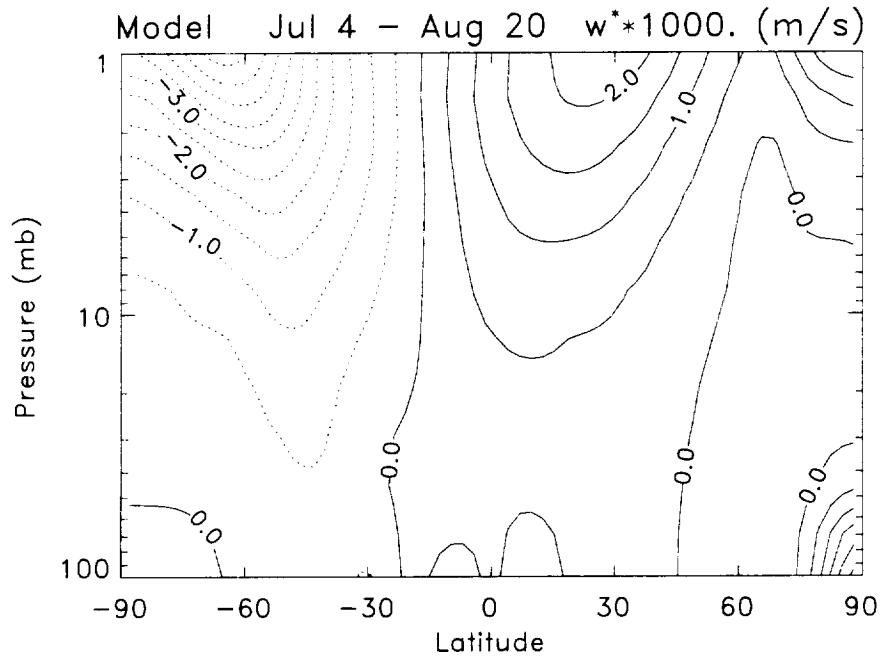


Figure 4.7: Vertical component of the diabatic circulation calculated from model data for the time period July 4 through August 20.

The vertical component of the mean diabatic circulation (w^* , as defined in [78]) for the July/August time period is shown in figures 4.6 and 4.7. Up to about 2 mb in the equatorial region model w^* is greater than UKMO w^* . Since model w^* is greater, there is stronger ascent in the model in that region. Thus the lower values of HF in the model in the equatorial region are the result of transport of HF weaker air from below.

4.1.2 January

Figure 4.8, Figure 4.9, and Figure 4.10 are analogous to Figures 4.1 through 4.3 except that they are for the January 5 to February 22 time frame. As before the most general features are seen in both HALOE and LaRC GCM distributions. There is a ridge of HF in the equatorial region, with decreasing values toward the poles. As in Figure 4.1, Figure 4.8 exhibits a secondary ridge feature below 10mb which is broader than the main ridge and located over the equator as well. The very high HALOE hydrogen fluoride values located below 50 mb in the tropical region are interference from clouds.

Figures 4.8 and 4.9 also illustrate some major differences between HALOE and model HF distributions. In general HALOE HF values are higher than model values in the equatorial region and lower at midlatitudes between about 40mb and 5mb. In the model distribution there is a swath of high HF values between 32°S and 48°S at 1mb which extends down to about 20 mb at 80°S. The maximum is located at 10mb at about 70°S.

In the northern (winter) hemisphere the model data has an anomalous feature similar to what was seen in the the winter hemisphere during July. Near 30°N between 10mb and 5mb model data is is higher than would be expected from the

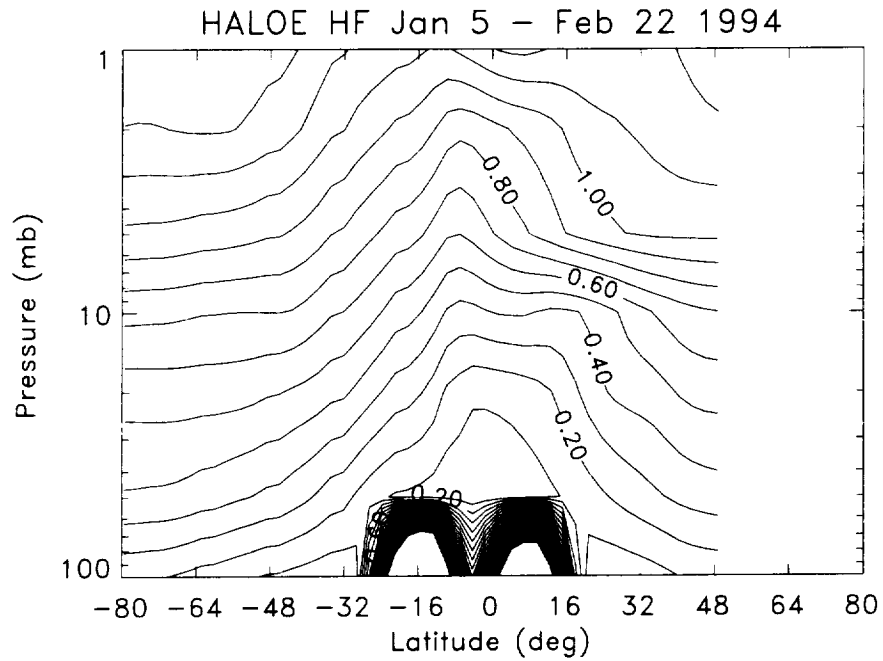


Figure 4.8: Same as in Figure 4.1 except for the time period January 5 through February 22, 1994.

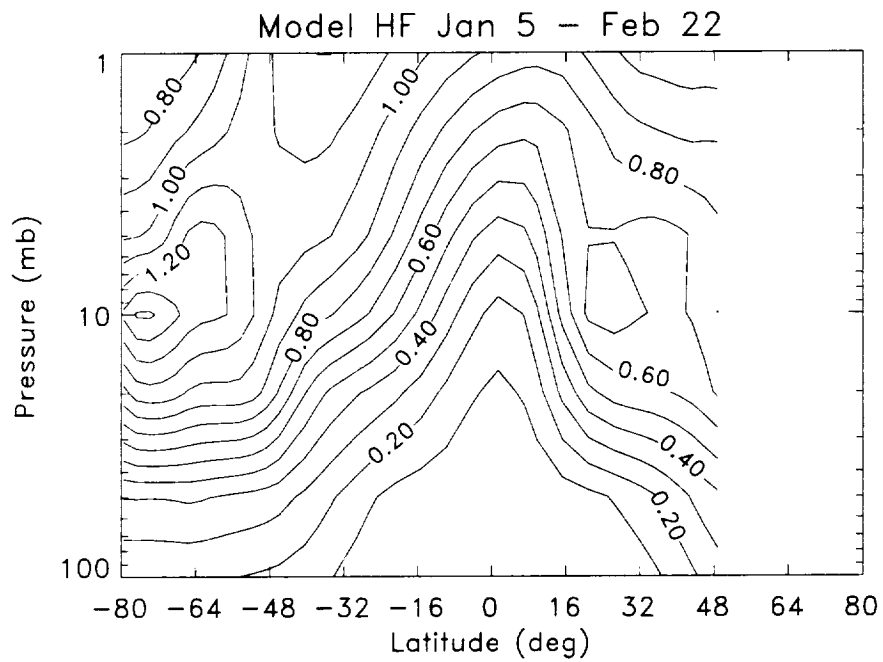


Figure 4.9: Same as in Figure 4.2 except for the January 5 - February 22 time period.

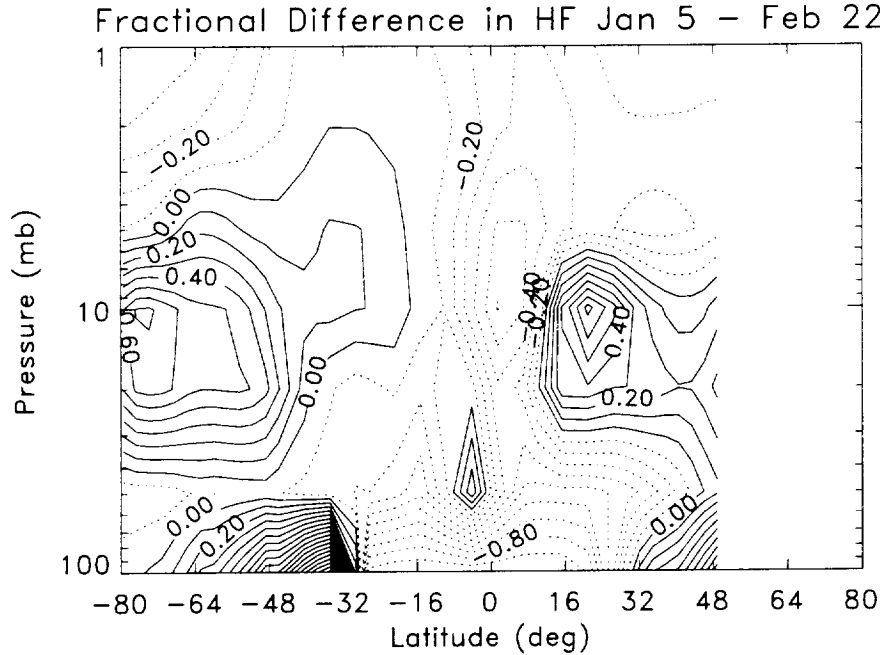


Figure 4.10: Same as in Figure 4.3 except for the January 5 - February 22 time period.

HALOE data. Also, poleward of this region of high HF values, there is a very steep drop off in HF. Another similarity with the July data is model isopleths of HF decrease faster toward the poles than the HALOE data indicates.

Figure 4.10 depicts the fractional difference between the HALOE and LaRC GCM HF distributions. This figure is also similar to July (Figure 4.3). Model HF is lower than HALOE HF in the equatorial region (spanning a larger latitude region below 30 mb, than above 30mb). In both January and July, wintertime low and midlatitudes between 30mb and 7mb model data is higher than HALOE data, though the difference is greater in January than July. The summertime hemisphere poleward of 16° also shows model values of HF greater than HALOE values of HF in both July and January with a maximum near 10mb. However, in January, the difference between HALOE and model HF is considerably greater than in July, and also cover

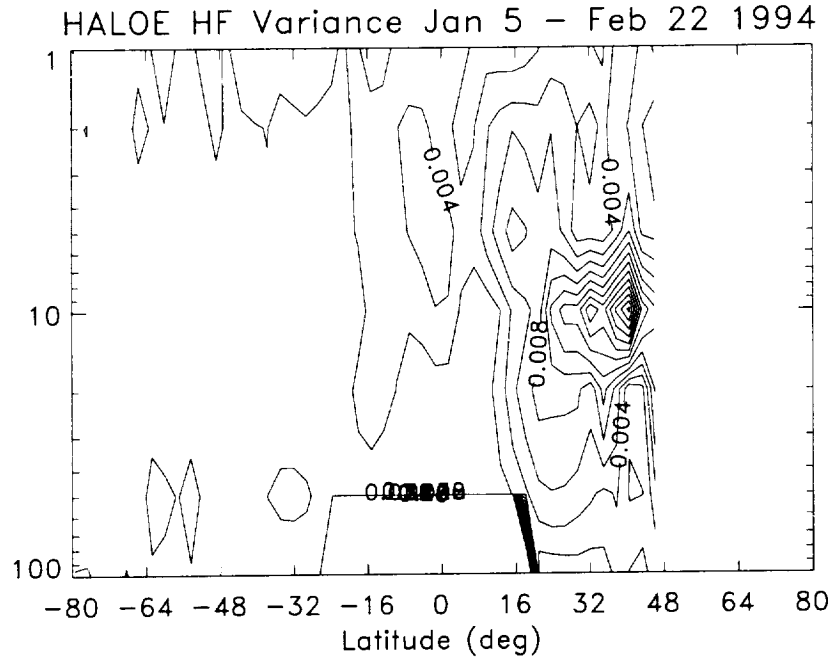


Figure 4.11: Longitudinal variance in HALOE HF distribution for the time period January 5 through February 22, 1994.

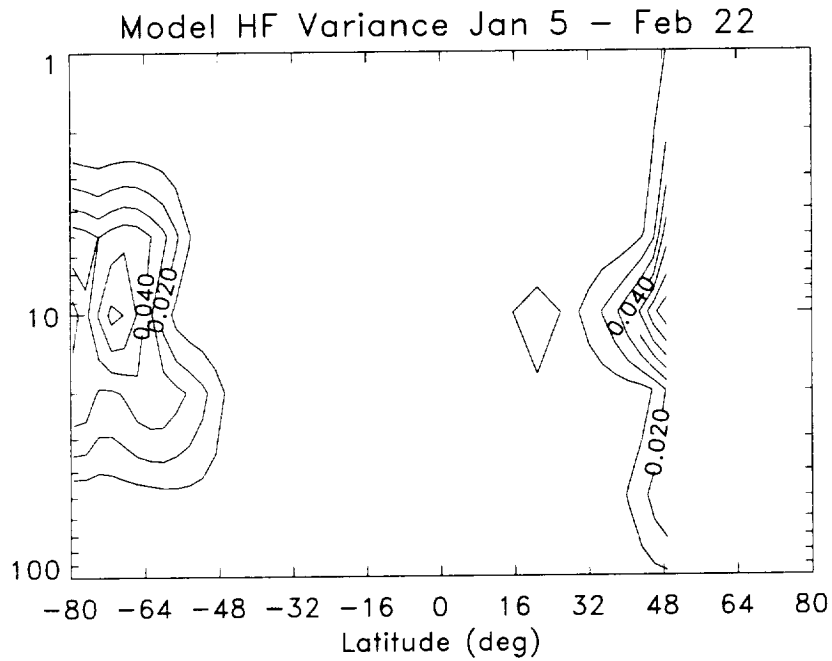


Figure 4.12: Longitudinal variance in MODEL HF distribution for the time period January 5 through February 22.

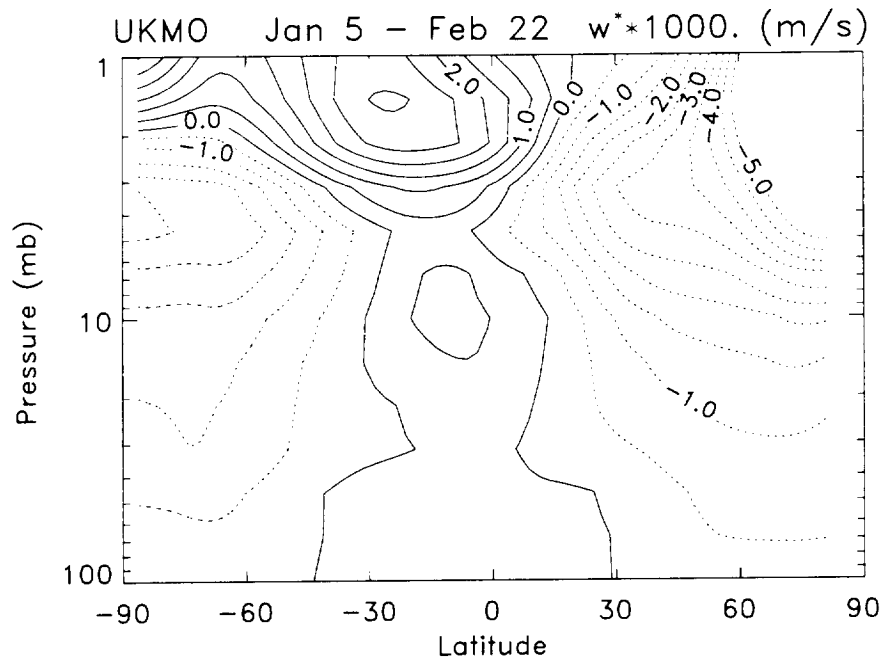


Figure 4.13: Vertical component of the diabatic circulation calculated from UKMO data for the time period January 5 through February 22, 1994.

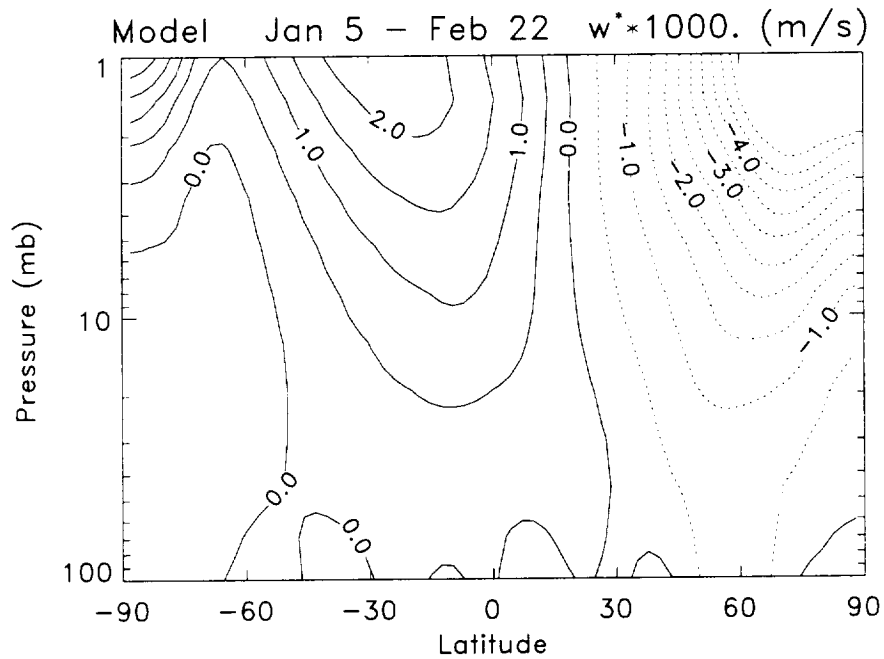


Figure 4.14: Vertical component of the diabatic circulation calculated from model data for the time period January 5 through February 22.

a larger region. As in July the January figure depicts a large percent difference below 50mb in the mid to high summer latitudes.

Figures 4.11 and 4.12 are analogous to Figures 4.4 and 4.5 except for the time period January 5 through February 22. As in the July time period, there is more wave activity in the HALOE HF data than in the model HF data at low latitudes above 10 mb. This results in HALOE HF contours being flatter than model HF contours at low latitudes (Figures 4.8 and 4.9).

There are differences in the variance at extra-tropical latitudes as well. Centered at about 10 mb near 40°N model variance is greater than HALOE variance. Also centered at 10 mb and 80°S there is evidence of enhanced wave activity in the model that was not present in the HALOE HF data. The impact of this extra-tropical wave activity present in model dynamics, but not the real atmosphere can be seen in the differences between model and HALOE HF distributions. The relationship between this enhanced wave activity and the maximum in model HF at high southern latitudes (and low HF above the maximum) is not precisely known and could be a complex interaction of model dynamics. Further analysis of this relationship is beyond the scope of this dissertation. In Figure 4.10 centered at 10 mb outside low latitudes there is up to a 60% difference between the two HF distributions.

The vertical component of the diabatic circulation (w^*) calculated from the mean circulation for the time period January 5 through February 22 is shown in Figures 4.13 and 4.14. As seen in Figures 4.6 and 4.7, model ascent is stronger in the equatorial region below 2mb than in the atmosphere in 1994. This again helps explain the lower model values of HF in the equatorial region which are transported upward more so in the model than actually occurred.

4.2 Vertical Profile Comparison

The vertical profiles shown here offer an additional evaluation of the LaRC hydrogen fluoride distribution. In these comparisons, HALOE data from 1993, 1994, and 1995 are used, allowing for consideration of annual variation in the HF distribution.

The HALOE vertical profiles shown for each year are an average of the all the vertical profiles retrieved on the days indicated for the specified occultation. The horizontal lines indicate the standard deviation of the unaveraged data at those pressure levels. In this way we can account for the variability observed by HALOE and assess whether or not the model data is consistent with it. Note that some comparisons are made with sunrise HALOE data, and some are made with sunset HALOE data. This is a result of choosing the occultation that provided data at the desired latitude or on the desired date. There is very little difference between the sunrise and sunset data.

Model profiles are extracted from daily zonal averages of model data. The latitude chosen is the one nearest the center of the HALOE latitude range. The date chosen for the model data is also the one nearest the middle of the range of HALOE dates. Except where noted, varying the date by a few days or the latitude by a few degrees in the model data had no significant impact on the comparison.

4.2.1 July

Figure 4.15 is a comparison of model and HALOE data at the end of July. HALOE data span the latitude 41.4°S to 45.9°S. Model data is at 43.3°S. The general profile shapes are similar, however exhibiting a few variations. The model data decrease slightly between 10mb and 5 mb, while the HALOE data are consistently increasing between 20mb and .3 mb. Some of the unaveraged HALOE profiles ex-

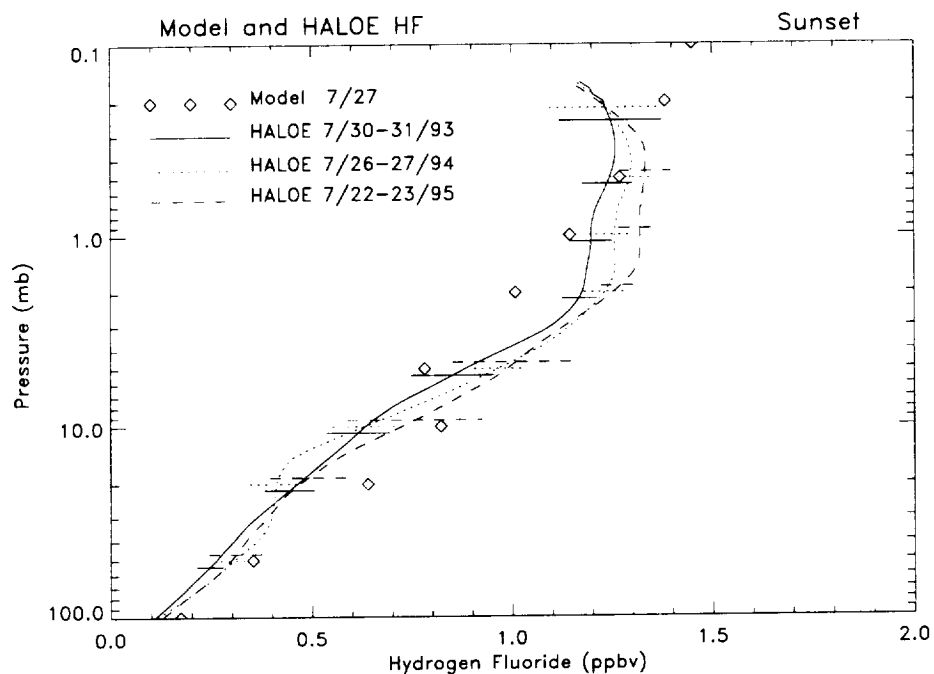


Figure 4.15: A comparison of July hydrogen fluoride (HF) data from HALOE and the LaRC GCM. The HALOE data is from 1993 (solid), 1994 (dotted), and 1995 (dashed), averaged over the days indicated and spans the region 41.4S to 45.9S. The horizontal lines indicate the standard deviation of the unaveraged vertical profiles at those altitudes. Model data is at 43.3S.

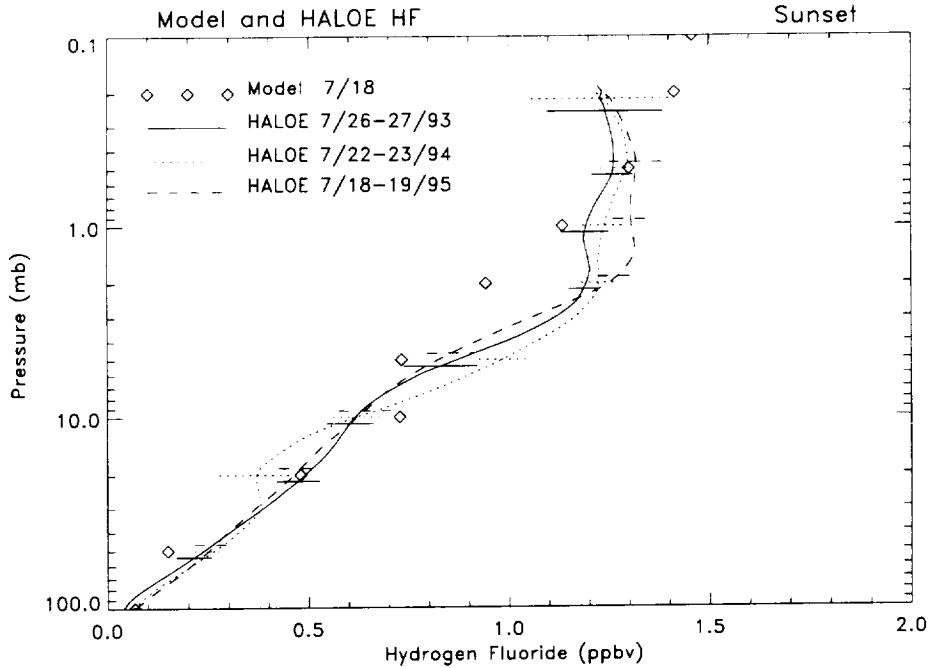


Figure 4.16: Same as in Figure 4.15 except HALOE data spans 27.3S to 35.9S and model data is at 32.1S.

hibited evidence of this behavior (decrease between 10 mb and 5 mb), however not consistently enough to impact the averaged profiles. This feature occurs in the model at the same latitude where there are differences between HALOE HF variance and model HF variance. Thus it is most likely due to differences in wave activity. Near the top of the HALOE profiles, model data continue to increase, while the HALOE profiles show a decrease beginning near .2 mb. At .2 mb this difference is within the standard deviation. The value of model HF is lower than HALOE HF by more than one standard deviation at 2mb and higher than HALOE data by more than one standard deviation at 20mb.

The HALOE vertical profiles in Figure 4.16 range in latitude 27.3°S to 35.9°S while the model profile is at 32.1°S. Below 10 mb the model HF and HALOE HF show fairly good agreement, however model HF is a little high at 10mb. The model

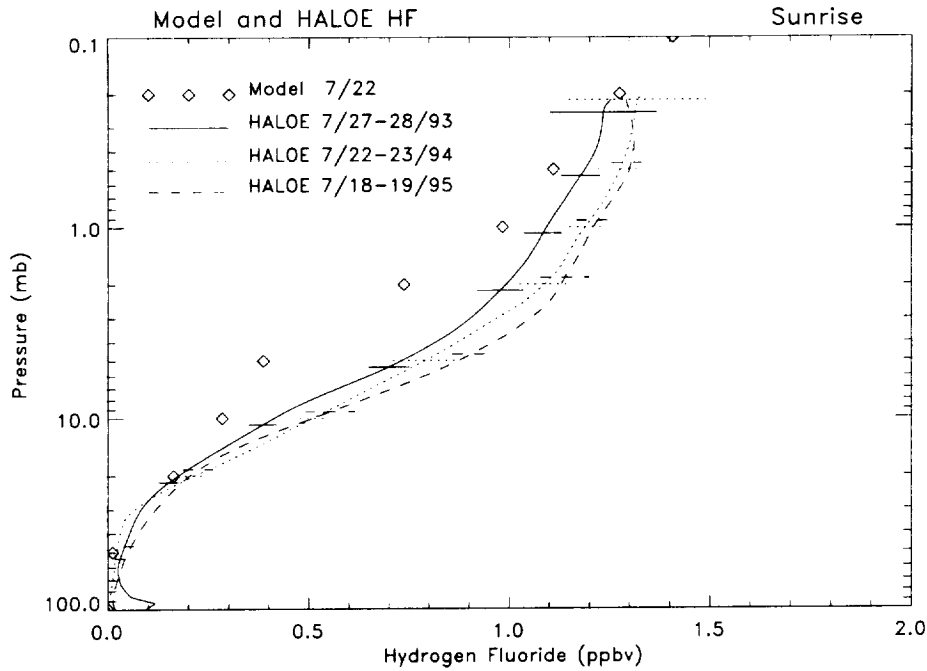


Figure 4.17: Same as in Figure 4.15 except HALOE data spans 5.2S to 7.7N and model data is at 4.2N.

data points are very close to the range of HALOE data at those pressure levels as indicated by the standard deviation (horizontal lines). Above 10 mb model HF is nearly constant up to 5 mb whereas HALOE data exhibit an increase with altitude, similar to Figure 4.15. Some of the unaveraged profiles in 1995 show this same behavior in the same altitude region even though it is not apparent in the averaged profile. Between 5 mb and 1 mb model HF levels are too low. Above 1 mb model HF is consistent with HALOE HF, consistent with the standard deviation of the unaveraged profiles. Note, however, that the trend in HALOE HF is a decrease with increasing altitude, while model HF continues to increase with height.

The summertime equatorial region is examined in Figure 4.17. Model HF values are at 4.2°N while HALOE data are between 5.2°S and 7.4°N. The model HF is in reasonably good agreement with HALOE hydrogen fluoride below 20 mb and above

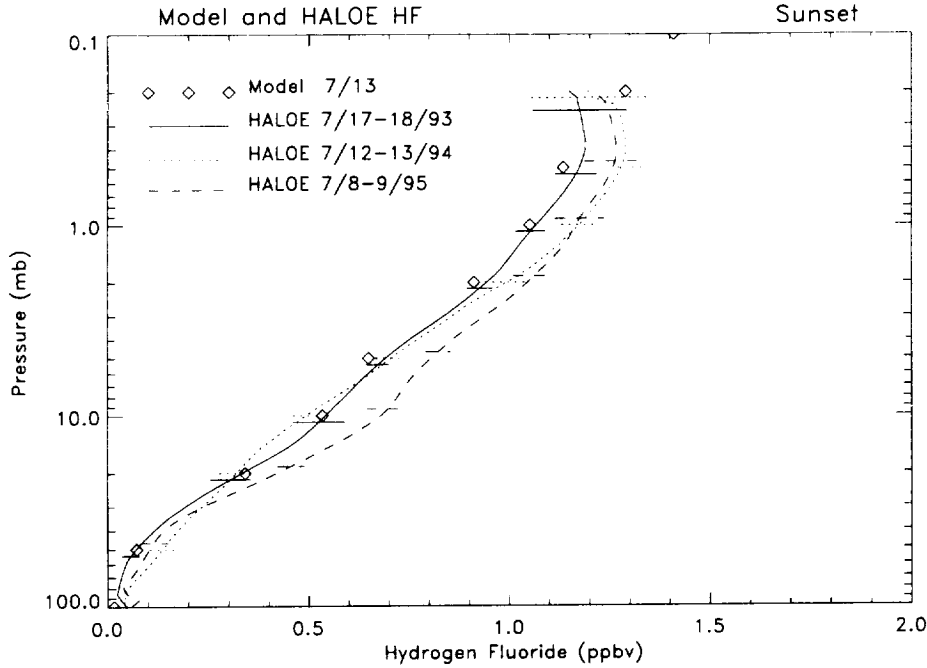


Figure 4.18: Same as in Figure 4.15 except HALOE data spans 9.7N to 22.0N and model data is at 18.1N.

.5 mb. However, from 10 mb to .5 mb model HF values are considerably lower than the HALOE measurements and not within one standard deviation of the HALOE data. The general trend of HF increasing with altitude is consistent in all the profiles. This feature (model values below HALOE values) was also illustrated in the zonal plot of Figure 4.10.

The comparison for northern hemisphere low to mid-latitudes in July is shown in Figures 4.18 and 4.19. Figure 4.18 shows the model data at 18.1°N with HALOE data ranging from 9.7°N to 22.0°N. Figure 4.19 shows model data at 34.9°N and HALOE hydrogen fluoride between 29.5°N and 38.9°N. Both figures show excellent agreement between HALOE and model hydrogen fluoride at all pressure levels.

Figure 4.20 is a higher latitude comparison with HALOE hydrogen fluoride spanning latitudes 52.1°N to 54.4°N and model HF at 54.4°N. Below 20 mb model HF

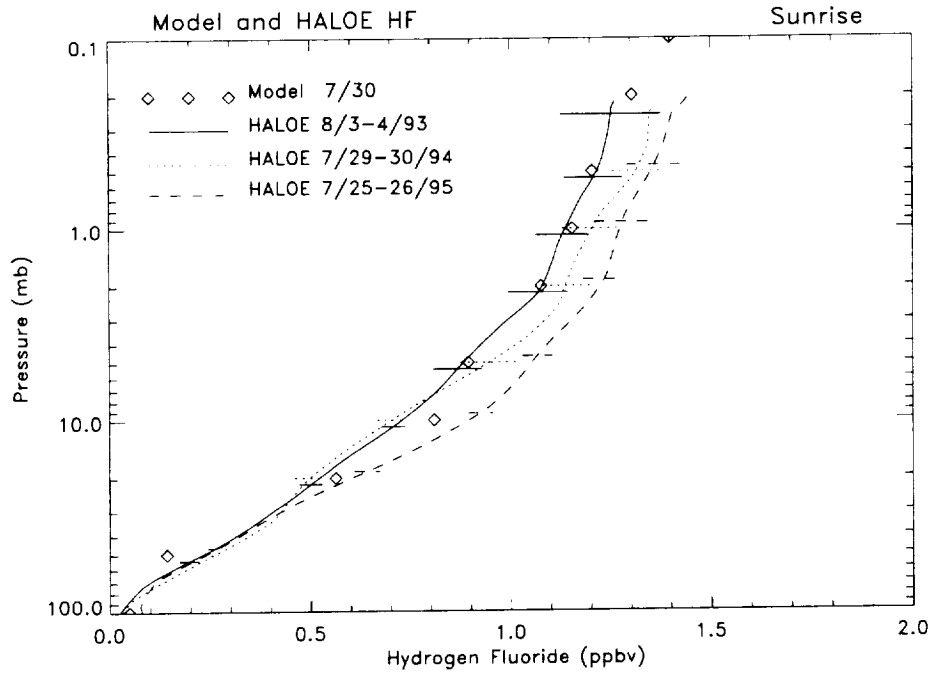


Figure 4.19: Same as in Figure 4.15 except HALOE data spans 29.5N to 38.9N and model data is at 34.9N.

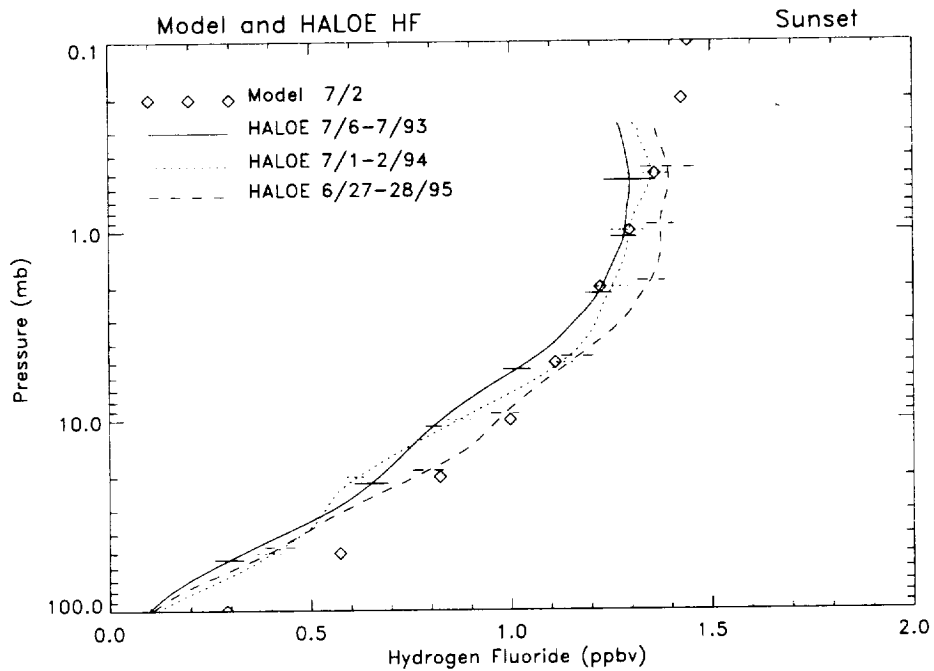


Figure 4.20: Same as in Figure 4.15 except HALOE data spans 52.1N to 58.0N and model data is at 54.4N.

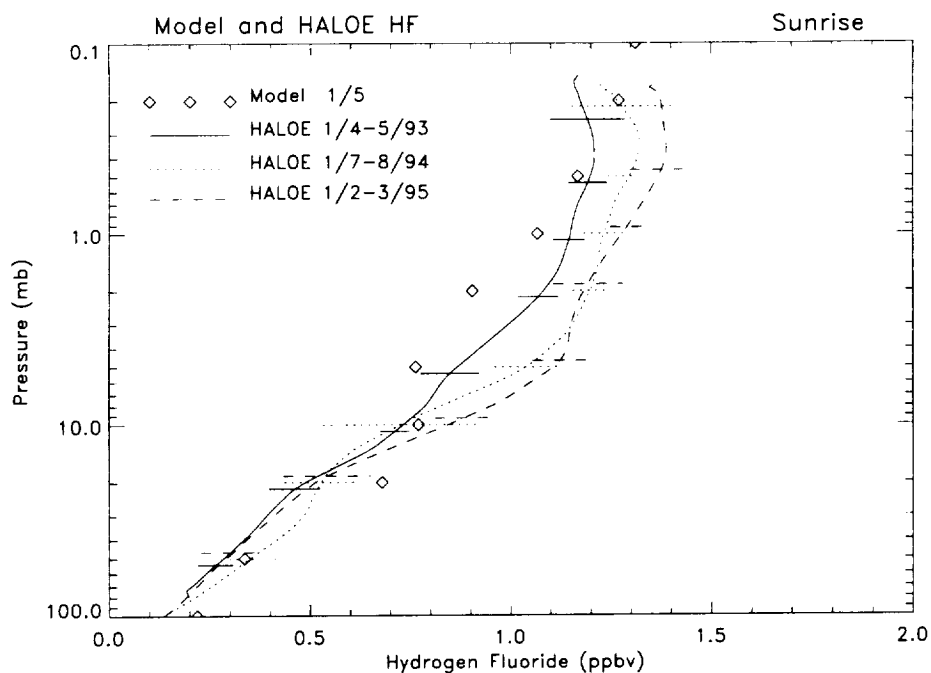


Figure 4.21: Same as in Figure 4.15 except in January, HALOE data spans 46.6N to 48.0N and model data is at 46.0N.

values exceed those measured by HALOE in 1993, 1994, and 1995 and are not within one standard deviation of the mean. Above .2 mb model HF also tends to be higher than HALOE HF. However, for the rest of the profile (10mb to .3 mb) there is excellent agreement with the model data falling very close to the HALOE data.

4.2.2 January

The northern mid-latitude wintertime comparison is shown in Figures 4.21 and 4.22. The HALOE data in Figure 4.21 span the latitude region 46.6°N to 48.0°N with model data at 46.0°N while the HALOE data in Figure 4.22 extend from 29.7°N to 37.6°N with model data at 32.1°N. The annual variation in the vertical profiles retrieved by HALOE in January (Figures 4.21 and 4.22) is greater than the annual variation shown in the same latitude region in the southern hemisphere winter in July (Figures 4.15 and 4.16). From 10 mb downward model data compares well with

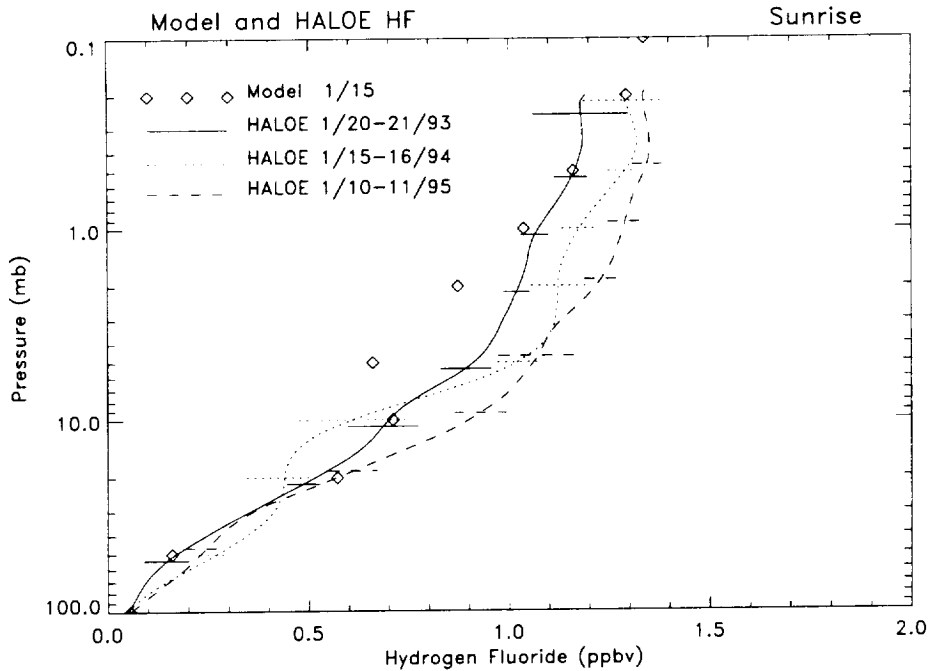


Figure 4.22: Same as in Figure 4.21 except HALOE data spans 29.7N to 37.6N and model data is at 32.1N.

the HALOE data. Except at 20 mb in Figure 4.21, the data in this region remain within one standard deviation of the mean of the HALOE data. Between 10 mb and 1 mb however, model data are lower than HALOE data. The comparison is slightly better at 46°N than at 32.1°N. Above 1 mb model data again agree well with the HALOE data. Approximately the same result was found in the southern hemisphere wintertime comparison (Figures 4.15 and 4.16), although the southern hemisphere comparison was somewhat better.

The January equatorial region is examined in Figure 4.23. HALOE data profiles range from 7.2°S to 7.1°N and model hydrogen fluoride profiles are at 1.4°S. For the full range of the vertical profiles, the model profile shape is consistent with the HALOE profile shape. However, for most of the vertical region being examined model HF values are too low. Below 20 mb the two data sets compare well and for

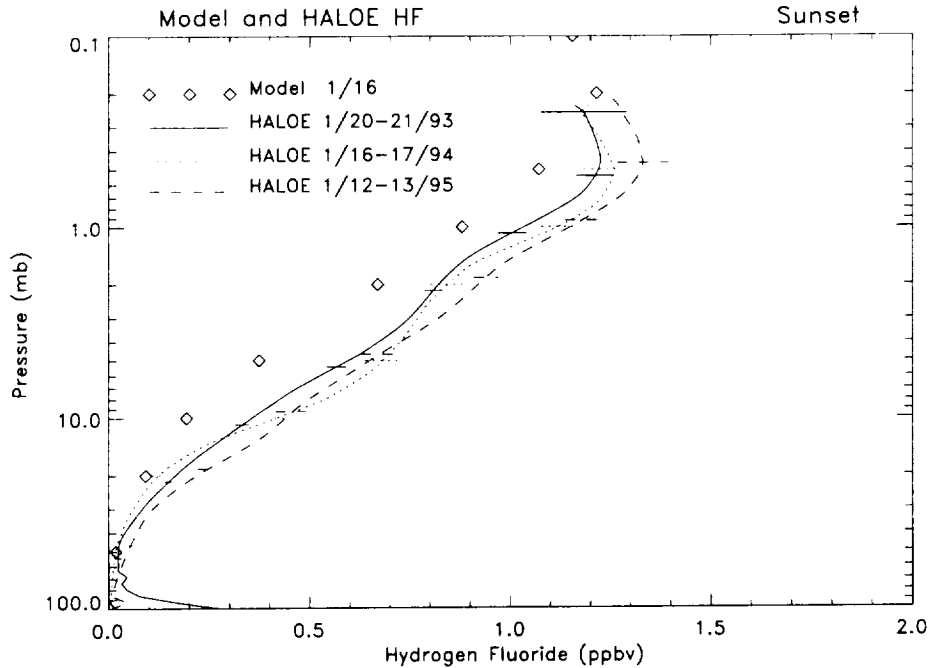


Figure 4.23: Same as in Figure 4.21 except HALOE data spans 7.2S to 7.1N and model data is at 1.4S.

.2 mb and above the comparison is also good. Again, the results of this comparison are similar to the results of the July equatorial comparison (Figure 4.17), with the January comparison being somewhat better.

The low to mid-latitude southern summer comparison is shown in Figures 4.24 and 4.25. In Figure 4.24 HALOE hydrogen fluoride profiles range from 12.5°S to 24.7°S with model HF profiles at 18.1°S. In Figure 4.25 HALOE HF profiles span the latitude region 29.3°S to 39.2°S with model HF profiles at 34.9°S. Both figures show model and HALOE profiles with similar shapes and values for HF, although there is slightly more annual variation in the higher southern latitudes from HALOE. The comparison in this region (29.3°S to 39.2°S) is slightly better than for the lower latitudes, with almost all model data points falling within one standard deviation of the mean in the HALOE data. The northern hemisphere summertime comparison

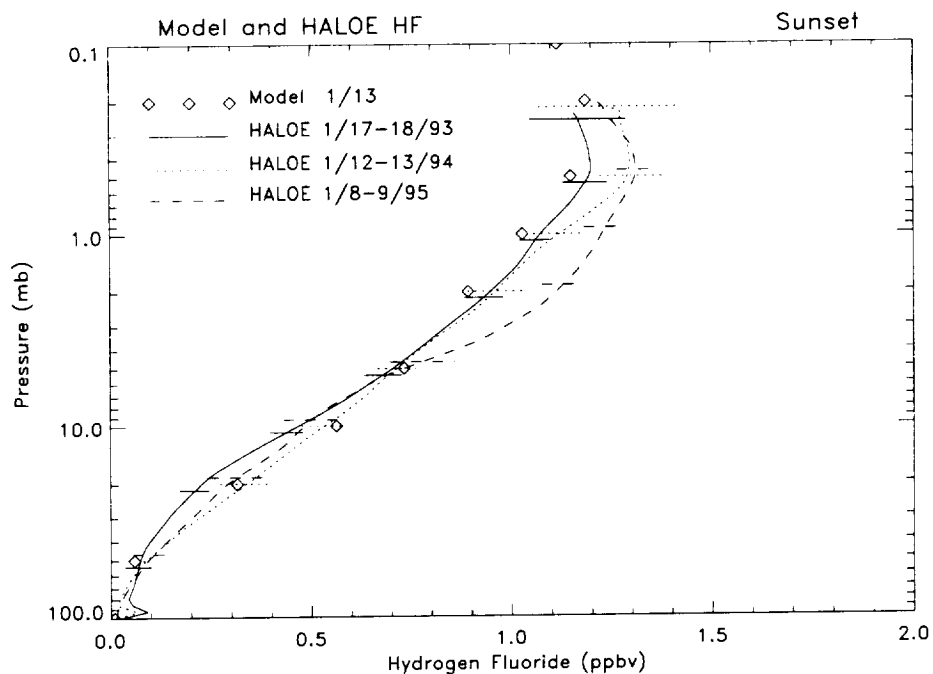


Figure 4.24: Same as in Figure 4.21 except HALOE data spans 24.7S to 12.5S and model data is at 18.1S.

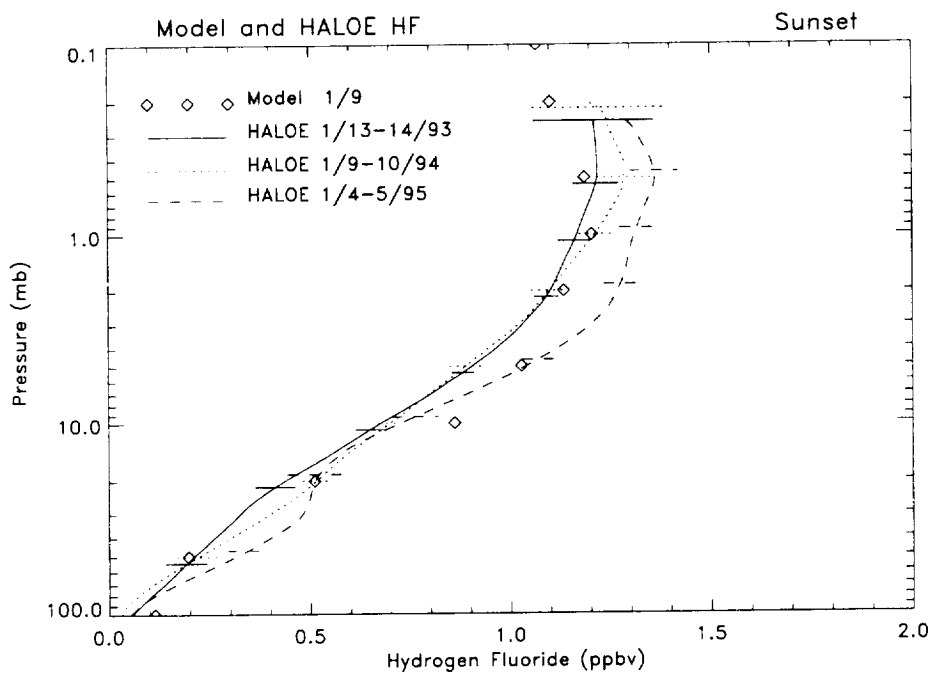


Figure 4.25: Same as in Figure 4.21 except HALOE data spans 39.2S to 29.3S and model data is at 34.9S.

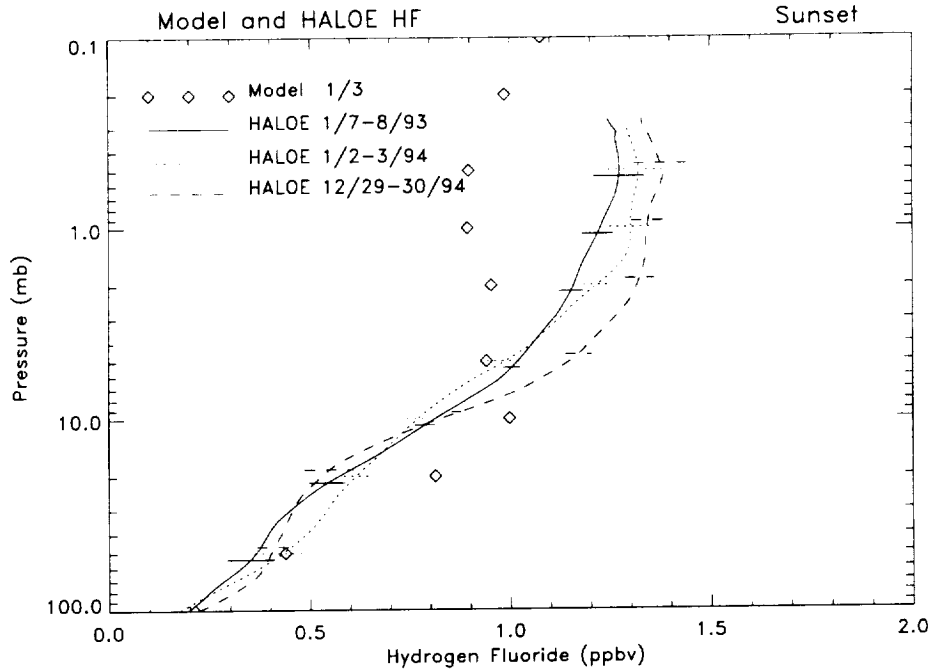


Figure 4.26: Same as in Figure 4.21 except HALOE data spans 57.5S to 51.3S and model data is at 54.4S.

for the midlatitudes (Figures 4.18 and 4.19) also showed excellent agreement between model and HALOE HF, even though the shapes of the vertical profiles are slightly different.

Finally, Figure 4.26 depicts the comparison at high southern latitudes. HALOE data cover the latitude region 51.3°S to 57.5°S and model profiles are at 54.4°S. It is clear that there is a significant difference between HALOE and model data above 5mb. Below 5mb the trend in model and HALOE data is the same, however model data is higher between 10mb and 20 mb. Above 5mb while HALOE hydrogen fluoride continues to increase with decreasing pressure, model HF decreases with decreasing pressure. This disparity between the two hydrogen fluoride distributions was also apparent in the zonal plots (Figures 4.9 and 4.8) in the high southern latitudes. The reason for this feature is not completely understood, except that it is related to wave

activity as was discussed previously concerning the zonal plots.

4.3 Conclusions

For the most part HALOE and model hydrogen fluoride distributions showed the same basic features in the July and January comparisons. One obvious exception to this is in the higher latitude southern hemisphere summer where model HF begins to decrease with increasing altitude while HALOE HF continues to increase with increasing altitude. Since the model does not attempt to simulate a specific calendar year, but rather a generic year, it can not be expected to reproduce exactly the HF distribution from 1994. The major differences between the model and HALOE HF zonal means have been attributed to differences in the wave activity and diabatic circulation.

To account for some annual variability, the vertical profiles were compared. The vertical profiles used HALOE data from 1993, 1994, and 1995 when most of the aerosol from Mt. Pinatubo had been removed from the stratosphere. This enabled a comparison of model and HALOE HF taking into account at least some of the normal annual variations in hydrogen fluoride. The horizontal bars also took into account variations in the HF profiles which would not have been apparent from just the averaged profiles. These comparisons further illustrated the strengths and weaknesses of the model HF distribution. The model exhibits the same general shape of the vertical profile as shown by HALOE and sometimes even very closely reproduces the values of HF (as is the case in the midlatitude region). One shortcoming is the model HF values are consistently lower than HALOE HF values in the equatorial region, more so than can be explained by error in the HALOE data. This could be due to model ascent over the equator being stronger than the actual atmosphere. The

difference noted in the southern hemisphere high latitude summer zonal plot is due to difference in wave activity as was shown in the HF variance plots.

This analysis showed that there were some obvious differences between the modeled HF distribution and the HF distribution observed by HALOE. These differences were due to several factors. First, the model is not an assimilation model. It does not attempt to reproduce the meteorological conditions which existed in 1994 (when the comparison HALOE observations were made). As a result differences between the two distributions were expected. Second, the differences which were discovered were attributed to differences in wave activity, lofting over the equator, and the absence of HF chemistry in the model. The differences in wave activity and ascent could partly be a result of shortcomings in the model and partly a result of just different meteorology. The ad hoc HF source term which was added helped somewhat with the HF distribution, but was not intended to completely remedy the problem. It is believed that these differences are well enough understood to continue on to the next step and use this HF distribution in the control and perturbed simulations so that hopefully conclusions about dynamical changes (due to the heating perturbation) can be made.

CHAPTER V

COMPARISON OF CONTROL AND PERTURBED MODEL SIMULATIONS

The GCM as well as the modifications made to it for this study have been discussed and analyzed in previous chapters. In this chapter a brief discussion of model temperature and zonal wind and how it compares to the actual atmosphere is presented first. Then impact of the diabatic heating perturbation on model parameters (temperature, zonal and meridional winds, and geopotential height) is presented. As stated in Chapter III, the heating perturbation is included in the LaRC GCM beginning June 15 and continuing through the end of December for a six and a half month perturbed simulation.

5.1 Comparison of Modeled and Actual Temperature and Zonal Wind

The January and July monthly averages of temperature and zonal wind from the LaRC model control simulation are compared to 12 year (1979-1990) climatological mean of NMC (National Meteorological Center) data to evaluate the accuracy of the unperturbed model. The NMC data is obtained from an NCAR (National Center for Atmospheric Research) technical note (see [79]).

In January, the zonal mean modeled temperature agrees reasonably well with the

NMC climatology. Both show a minimum (200K) over the equator centered at about 80 mb. Below this, The temperature gradually increases (maximum slightly south of the equator) as pressure increases to a maximum of about 290 K for both model and NMC data again. Above the equatorial minimum the temperature increases (favoring the southern hemisphere) to a maximum of 290 K at southern polar latitudes (modeled maximum at about 1.5 mb while NMC maximum is about 1 mb). The one difference concerns a temperature minimum at northern polar latitudes. Both the modeled data and NMC data show a minimum however the modeled minimum is centered at a lower pressure level (30 mb instead of 50 mb) and the magnitude of the minimum is greater for the modeled temperature (190 K as opposed to 210 K).

The zonal wind comparison in January is also quite good. Both the NMC and model data have two westerly jets centered at about 200 mb at 30°N and S. The NMC and simulated jets in the southern hemisphere are about the same magnitude (20 m/s) while in the northern hemisphere the modeled westerlies are slightly stronger than the NMC climatology (40 m/s as opposed to 35 m/s). At lower pressure levels both the model data and the NMC data are comprised of easterlies south of the equator and westerlies north of the equator. The NMC easterly maximum is slightly lower than for the simulated data (50 m/s for NMC compared to 60 m/s for the model). In the northern hemisphere the model westerlies are much stronger (70 m/s for the model versus 40 m/s for the NMC data). This is expected since the modeled temperature gradient was stronger in the model as stated above.

In July the comparison of the NMC and model control temperature is better than in January. The NMC minimum is 210 K at 80 mb while the modeled minimum is 210 K at 70 mb. The maximum at the surface is 290 K in both cases and is also center at about 10°N for both cases. There is a maximum of 280 K at 1 mb both

in the NMC data and the simulated data. As with the January comparison, the minimum at high latitudes in the summer hemisphere is stronger in the modeled data than in the NMC data (170 K for modeled data and 190 K for the NMC data). The modeled minimum is again at a lower pressure level (about 15 mb versus 40 mb for NMC).

The July zonal wind comparison illustrates the same features seen in the January comparison. Both datasets have westerly jets at 200 mb (at 30°S and 40°N). Maximum winds in the southern hemisphere (at 200 mb) are about 40 m/s in the modeled data and 35 m/s in the NMC data. Maximum winds in the northern hemisphere (at 200 mb) are 10 m/s in the modeled data and 15 m/s in the NMC data. Above this the northern hemisphere is dominated by easterlies while the southern hemisphere is dominated by westerlies for both datasets. The easterlies are somewhat stronger in the simulated data (40 m/s instead of 30 m/s). As with the summertime westerlies in January, the modeled westerlies are considerably stronger in the simulated data (130 m/s versus 90 m/s).

This comparison of the modeled control data and the climatological data from the real atmosphere shows that most of the time the agreement is quite good. Both data sets agree on the location of maxima and minima and in most cases even on the magnitude of the maxima and minima. The one area of disagreement is at high latitudes in the summer hemisphere stratosphere when the modeled temperature is much lower than NMC climatology and related to that are the stronger westerlies in the modeled data.

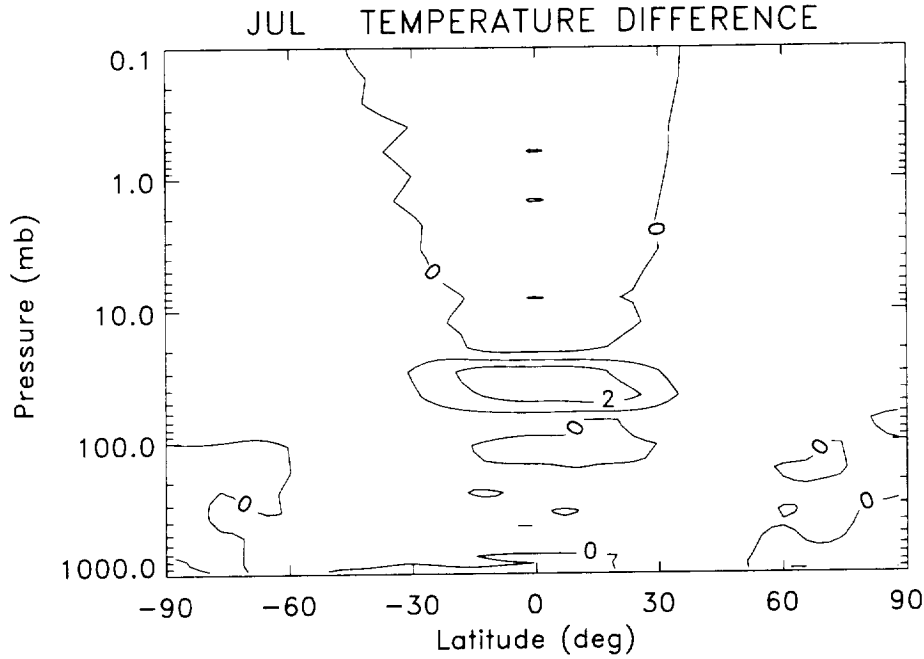


Figure 5.1: July average for the zonal mean temperature difference. Contour interval is 1 K.

5.2 Zonal Mean

5.2.1 Temperature

Figures 5.1, 5.3, and 5.5 illustrate the impact of the heating perturbation on the zonal mean temperature in July, October, and December, respectively. The figures show the difference between the perturbed temperature and the control temperature. A positive value indicates warming (perturbed temperature is higher than control temperature) and a negative value indicates a cooling has occurred. The difference is calculated for each day and then monthly means are calculated. Figures 5.2 and 5.4 illustrate the October and December monthly means in temperature for the control case. The July monthly mean of temperature is not shown since the impact of the heating perturbation is considerably weaker in July. The zonal mean temperature response has two components, one in the equatorial region and one at high latitudes.

Even though the maximum heating perturbation occurred in late June (10 K/day), the greatest impact on temperature did not occur until early October, with the October monthly mean difference showing the greatest temperature increase (Figure 5.3). The maximum heating is over 9 K centered at the equator at 29 mb. This is expected since the largest concentration of enhanced heating rates is at low latitudes.

The extra-tropical response to the perturbation becomes visible in the zonal mean figures in September (not shown) and continues to strengthen through the end of December. This response is predominantly a negative one, indicating a cooling. Notice that in December there is a small region of temperature increases in the southern hemisphere polar region. Initially, the extra-tropical decrease in temperature is only present in the southern hemisphere, however by October a northern hemisphere response begins to develop at about 2 mb. These figures show how the overall impact on the temperature is to increase the equator to pole temperature gradient in both the northern and southern hemispheres at 30 mb by 50% in October and 25% in December.

5.2.2 Zonal Wind

The effects of the heating perturbation on the zonal mean zonal wind are shown in Figures 5.6 through 5.10. As with temperature the quantities shown are the perturbed zonal wind minus the control zonal wind and then averaged over a month. The October and December monthly mean zonal winds for the control case are shown in Figures 5.7 and 5.9. As with July the July monthly mean control zonal wind is not shown since the difference (Figure 5.6) is much weaker than in October and December. Initially, the perturbation is symmetric about the equator and centered at about 20 mb, as seen in Figure 5.6. It consists of two nodes of equal magnitude

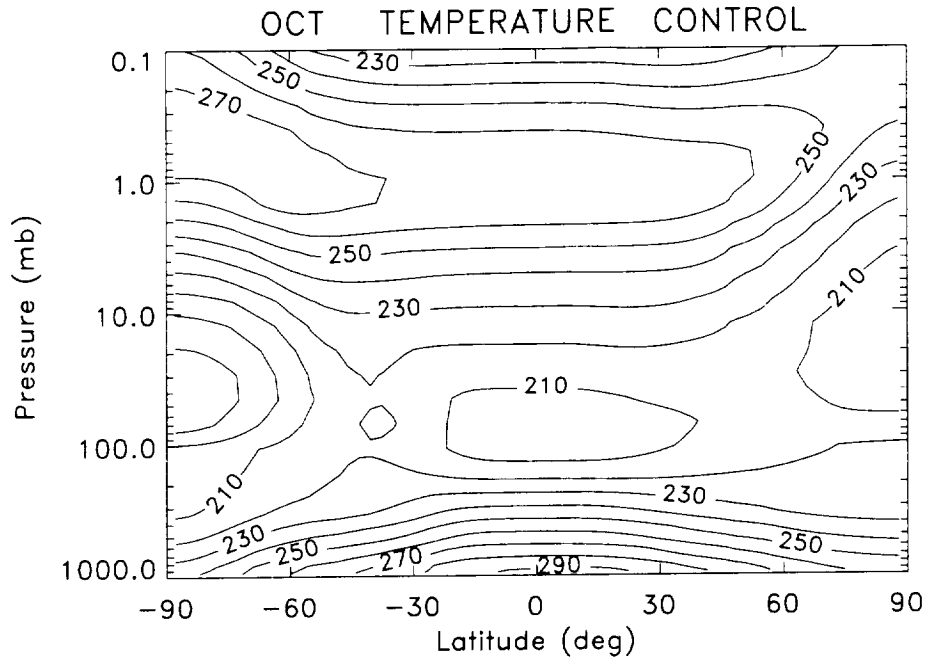


Figure 5.2: October monthly average of temperature for the control case.

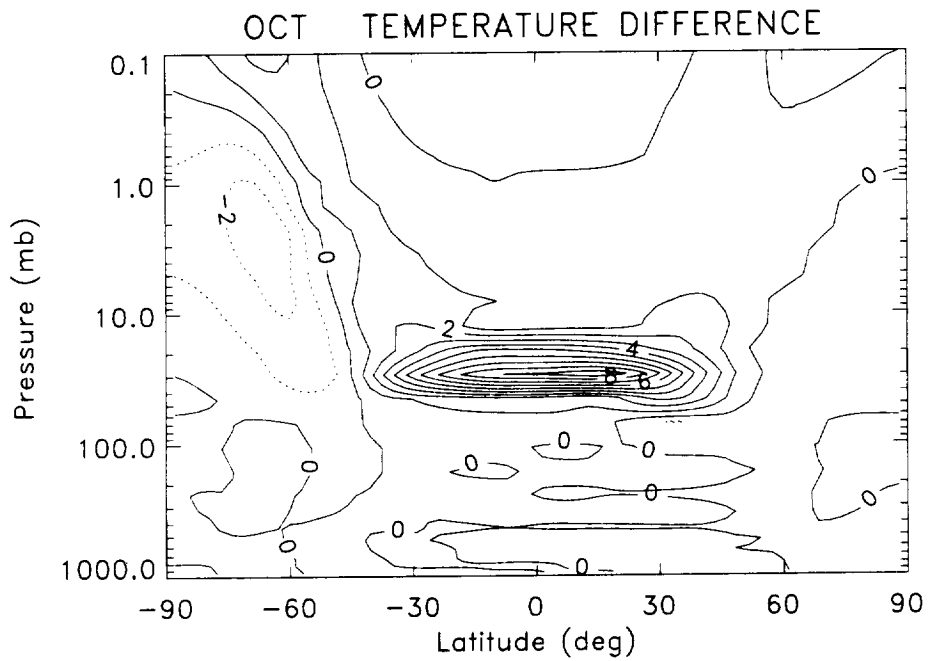


Figure 5.3: Same as Figure 5.1 except for October.

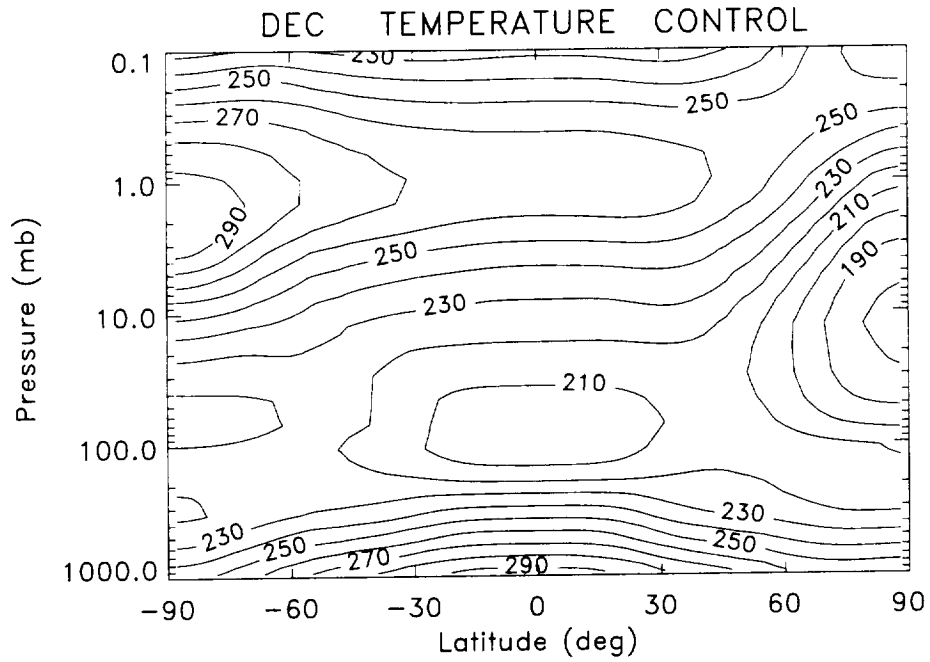


Figure 5.4: December monthly average of temperature for the control case.

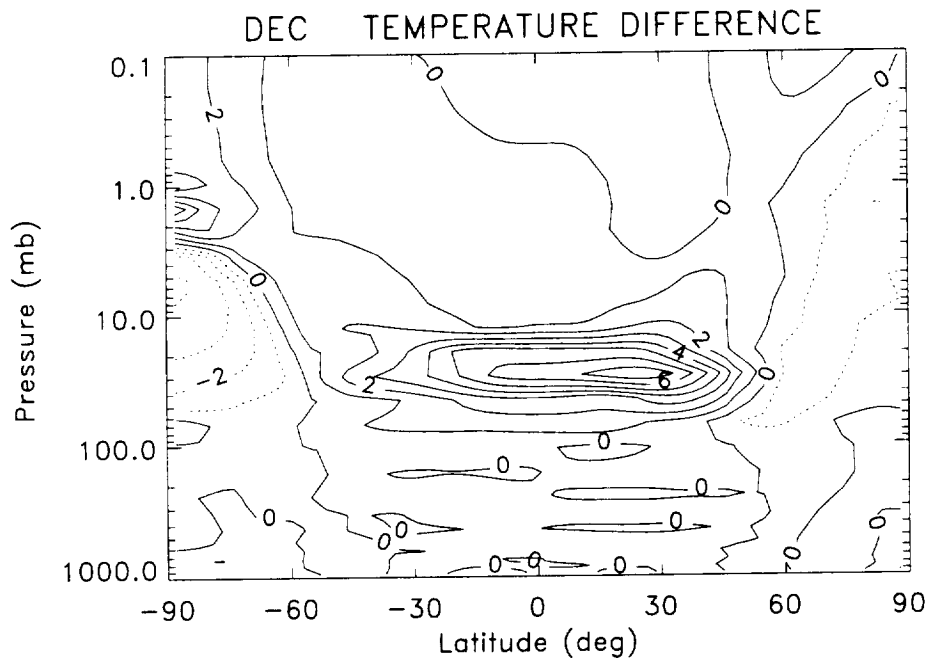


Figure 5.5: Same as Figure 5.1 except for December.

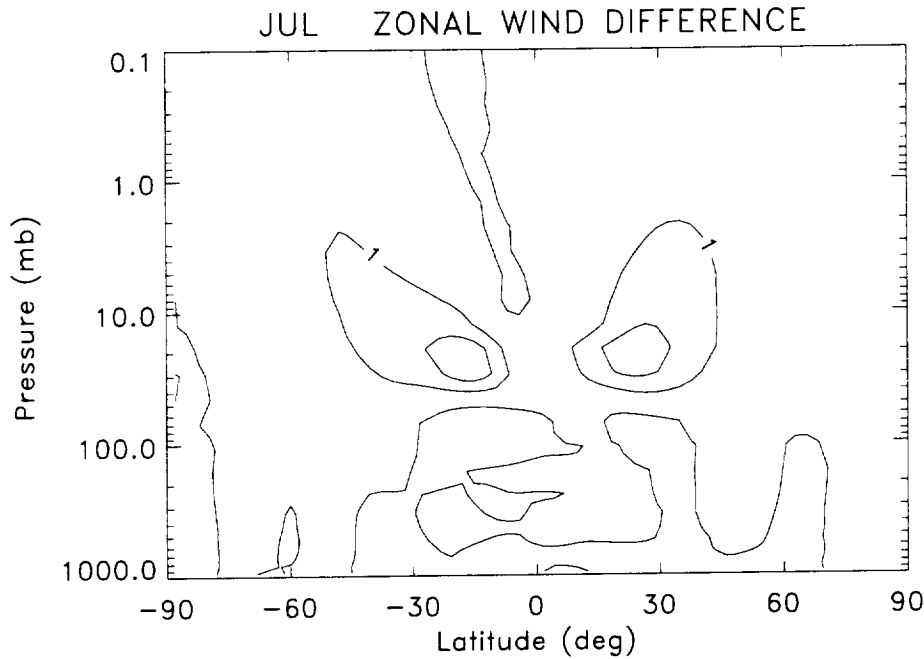


Figure 5.6: July average for the zonal mean zonal wind difference. Contour interval is 1 m/s.

(maximum about 2 m/s). These two nodes do not develop symmetrically, however. The southern hemisphere node increases in magnitude more rapidly than the northern hemisphere node so that by October the southern hemisphere maximum is 12 m/s while the northern hemisphere maximum is 7 m/s (Figure 5.8). In addition the geographical coverage differs somewhat. In the northern hemisphere the zonal wind perturbation covers a slightly larger area, with the maxima in a different location than the southern hemisphere. In October the southern hemisphere maximum is at about 50°S and .6 mb, while the northern hemisphere maximum is at 40°N and a pressure level of about 6 mb. In addition a negative perturbation has developed at high southern latitudes by October with a minimum of -3 m/s. This has the effect of strengthening the westerly jets in both the northern and southern hemispheres with the southern hemisphere being shifted north.

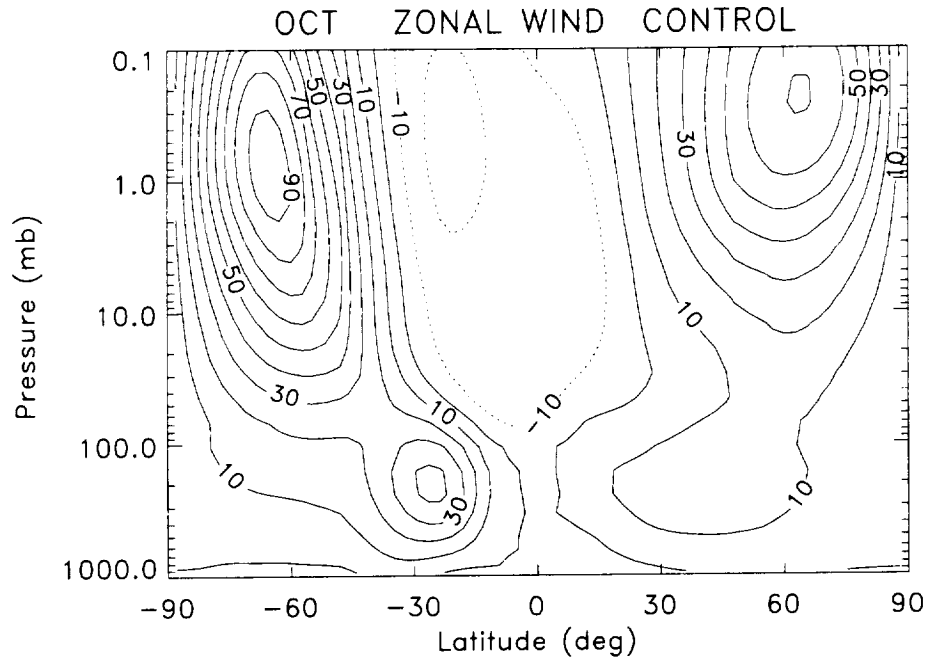


Figure 5.7: October monthly average of zonal wind for the control case.

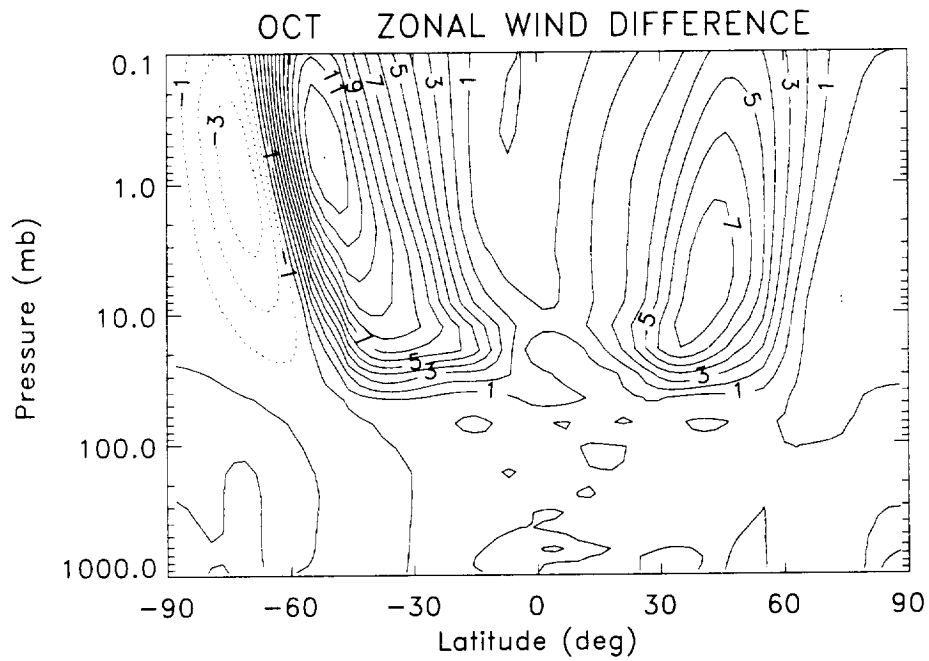


Figure 5.8: Same as Figure 5.6 except for October.

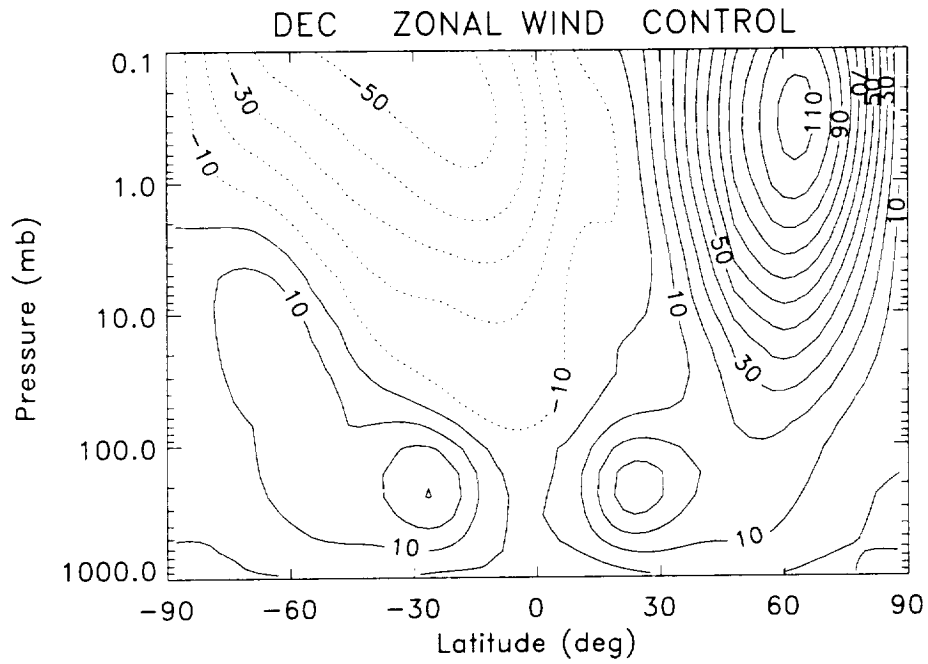


Figure 5.9: December monthly average of zonal wind for the control case.

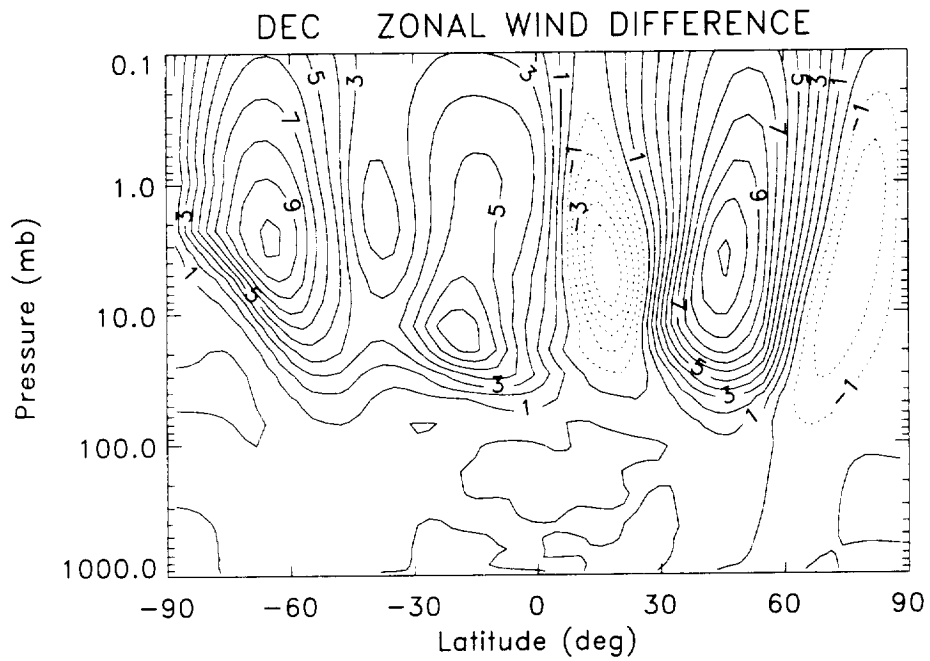


Figure 5.10: Same as Figure 5.6 except for December.

Through November (not shown) and December (Figure 5.10), the southern hemisphere maximum decreases in magnitude and the pressure level of the maximum increases (lower altitude) so that by December, the maximum is at 3 mb. The southern hemisphere maximum also shifts farther south so that by December it is centered poleward of 60°S . Simultaneously a secondary southern hemisphere maximum develops at lower latitudes (centered between 30°S and the equator). This maximum is smaller in magnitude and at a higher pressure level (about 20 mb). These changes result in weaker southern hemisphere summer easterlies.

The northern hemisphere also undergoes significant change between October and December. The maximum at about 45°N remains there, however its magnitude increases from 7 m/s to 11 m/s and decreases in pressure level slightly (rising to 3 mb). In addition, the geographical coverage of the positive values decreases from between the equator and 70°N to between 30°N and 60°N . This is the result of two regions of negative zonal wind perturbation developing to the north (between 60°N and the north pole) and to the south (between the equator and 30°N). The minimum in the tropical latitudes is stronger than the minimum in the polar latitudes. These perturbations strengthen the northern hemisphere westerlies and condense the jet somewhat.

5.2.3 Meridional Wind

There are no figures shown depicting the changes in the zonal mean meridional wind resulting from the heating perturbation because the zonal mean meridional wind remained essentially unchanged. The maximum change was between 1 m/s and -1 m/s until December when the maximum reached 3m/s at the high northern latitudes above 1 mb.

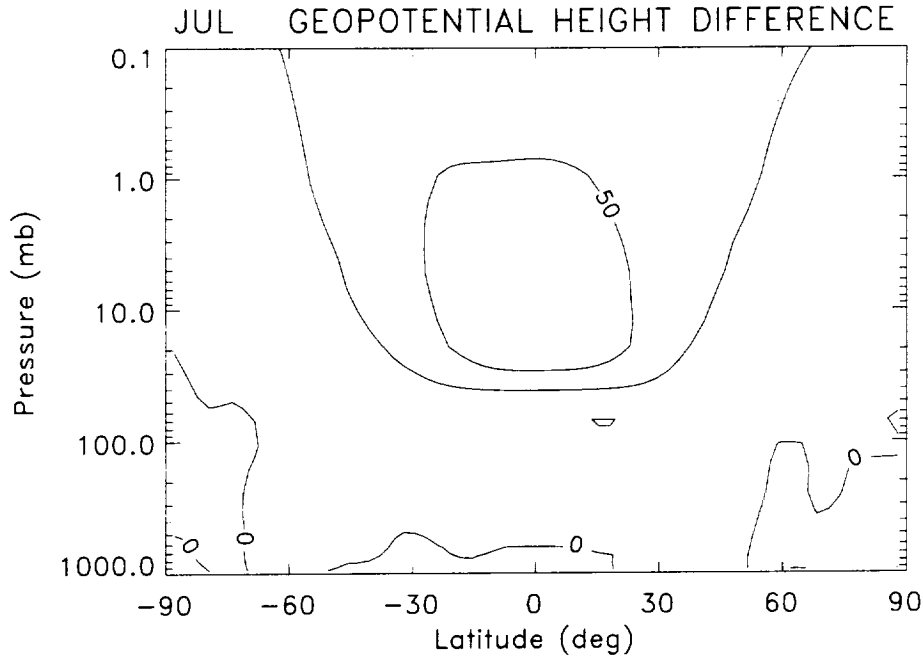


Figure 5.11: July average for the zonal mean geopotential height difference. Contour interval is 25 km.

5.2.4 Geopotential Height

Figures 5.11, 5.12, and 5.13 depict the changes to the zonal mean geopotential height that result from the diabatic heat enhancement. The data are differenced the same way the temperature and zonal wind data were. The perturbation to the zonal mean geopotential height begins centered over the equator (between 60°N and S) at about 5 mb with a maximum of 50 km (Figure 5.11). This perturbation continues to increase through November when a maximum of 250 km is reached (not shown). During this increase, the maximum remains essentially symmetric about the equator through October (Figure 5.12). By December however, the northern hemisphere is favored and the perturbation values are greater there (Figure 5.13).

In addition to the enhancement to the geopotential height in the low and mid-latitudes, beginning in August (not shown), a negative perturbation becomes visible

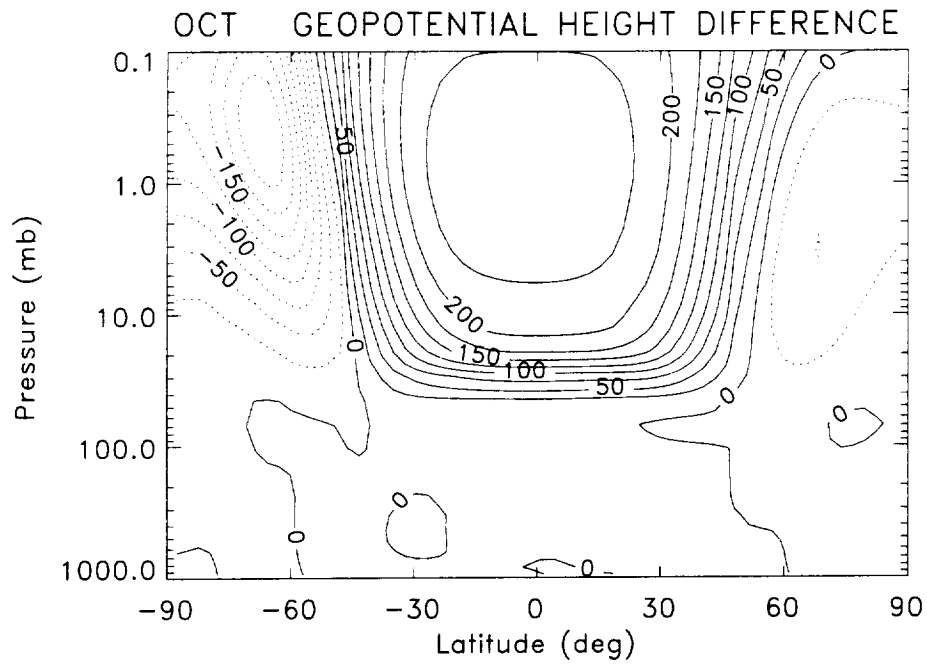


Figure 5.12: Same as Figure 5.11 except for October.

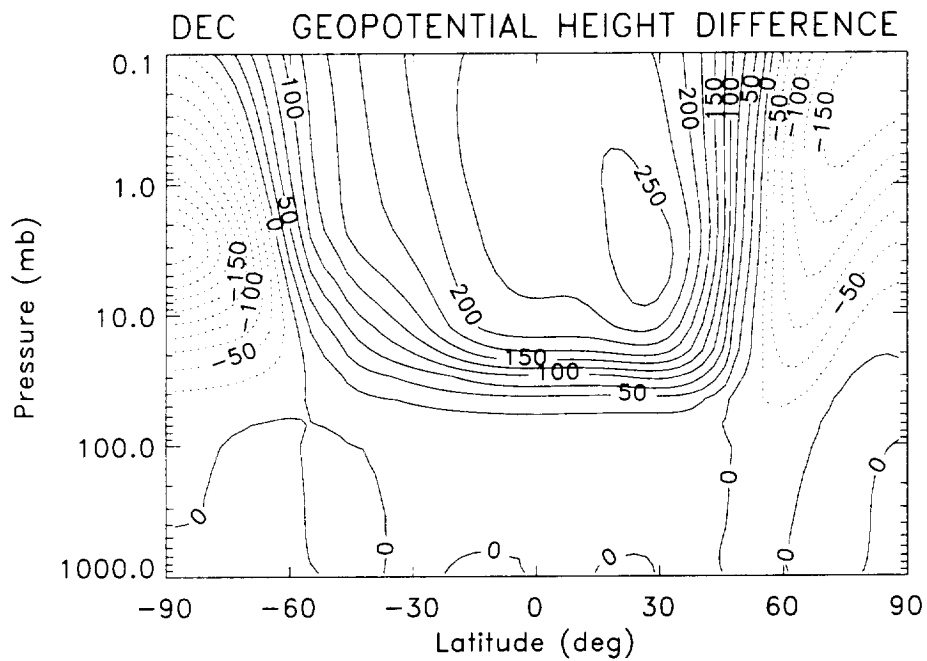


Figure 5.13: Same as Figure 5.11 except for December.

in the southern hemisphere. This region of negative changes to geopotential height is weaker than the enhancement and located at a slightly higher level (.3 mb and 60°S in October, Figure 5.12). In October, another weakening of geopotential height begins to develop in the northern hemisphere at high latitudes. Both of these regions of weakening geopotential height continue to increase in magnitude through December. Note that all changes to the geopotential height occur above the 50 mb level.

5.3 Climatological Variance

In the previous section changes in the zonal mean for temperature, zonal wind, and geopotential height due to the diabatic heating enhancement were presented. It is clear that some large deviations from the control values developed. What is not clear is how these perturbations in the model parameters compare to climatological variations in the LaRC GCM. To investigate this a ten year climatological run of the LaRC GCM was completed. The first year of this simulation corresponds to the control run used for comparison with the perturbed run. The remaining nine years are a continuation of the control run (no heating perturbation). The following is a presentation of the climatological and perturbation variances. The climatological variance shows how much variability there is during the ten year climatology for a given month. The perturbation variance indicates how much the perturbed simulation varied from the climatology. The climatological and perturbation variances for the meridional wind are not shown because they have almost no variation at all. For temperature, zonal wind, and geopotential height the climatological and perturbation variances are shown for October and December. July is not presented since the perturbations in the model parameters were less pronounced earlier in the simulation as shown in the previous section.

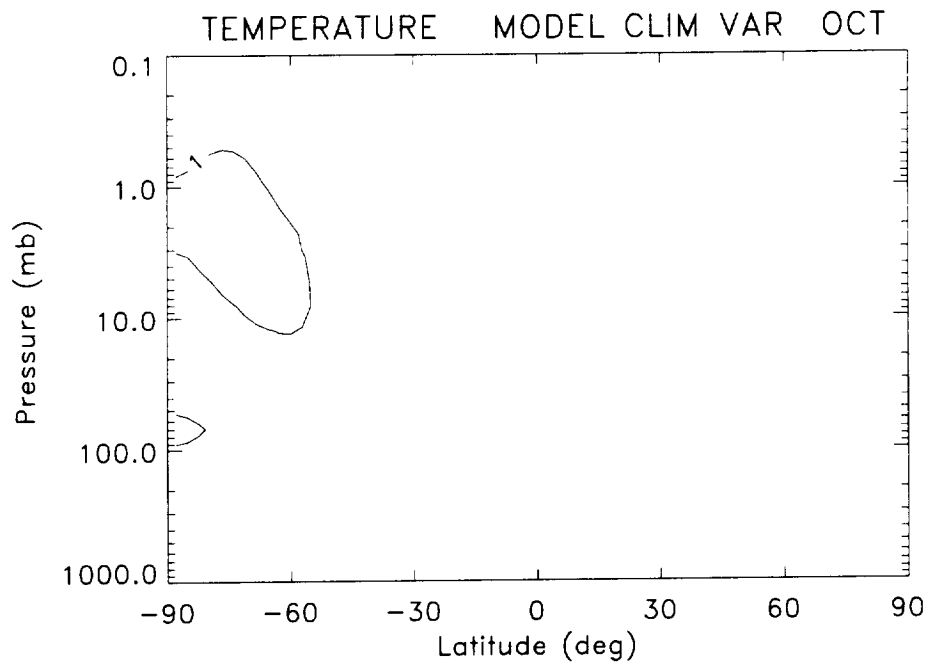


Figure 5.14: Climatological variance in ten consecutive October monthly means of zonally averaged temperature. Contour levels are 1, 10, and 100 K^2 .

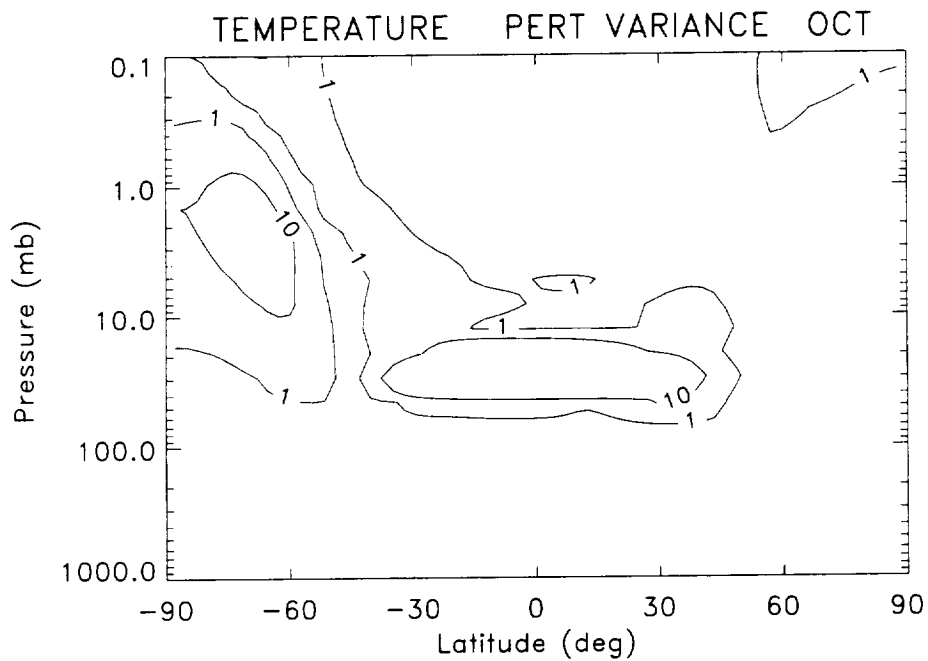


Figure 5.15: Perturbation variance for October monthly mean of zonally averaged perturbed temperature data. Contour levels are 1, 10, and 100 K^2 .

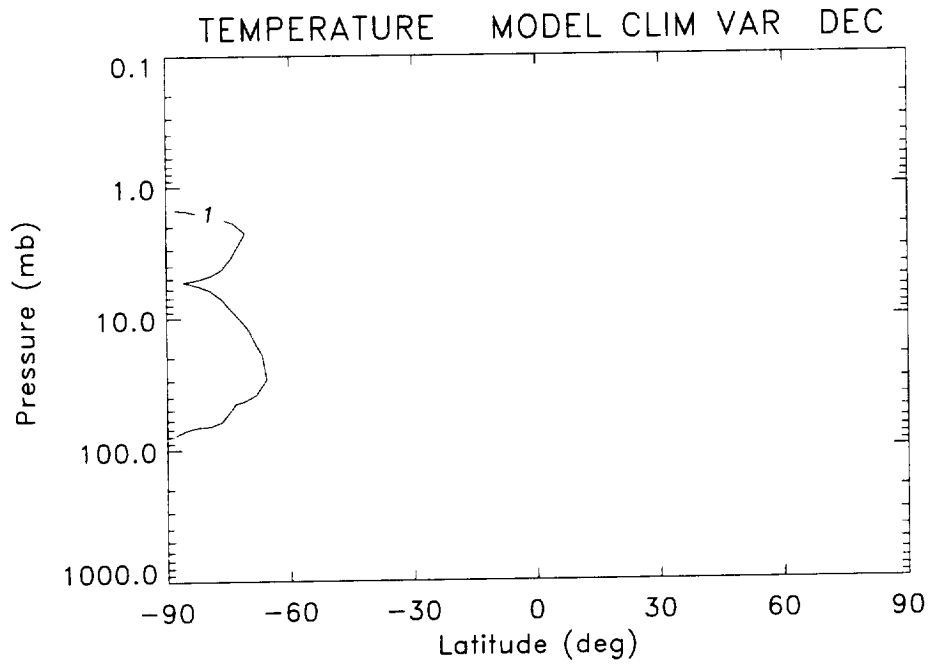


Figure 5.16: Same as Figure 5.14 except for December.

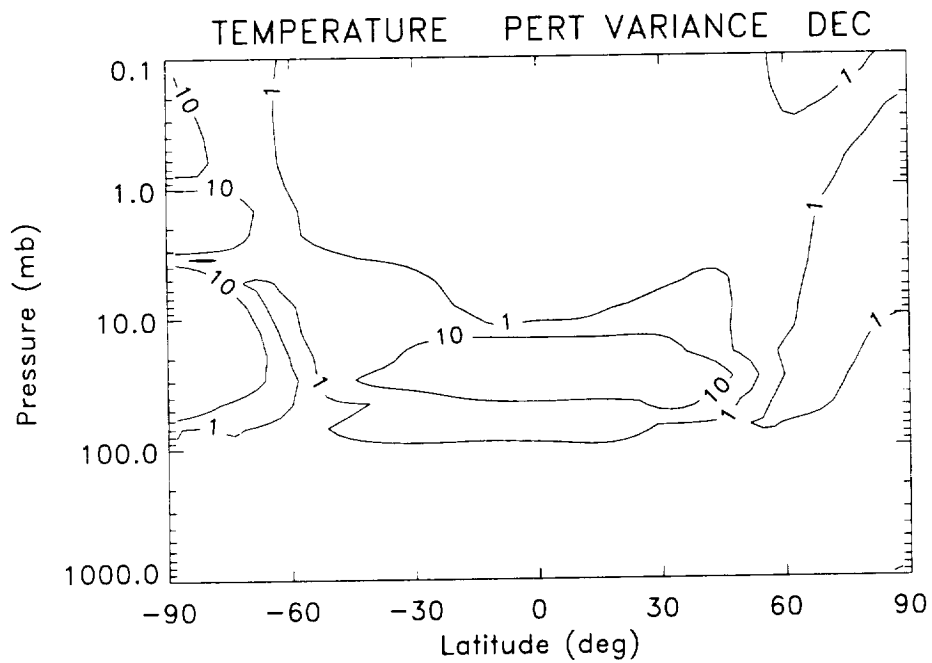


Figure 5.17: Same as Figure 5.15 except for December.

5.3.1 Temperature

The climatological and perturbation variances for October and December are depicted in Figures 5.14 through 5.17. Figures 5.14 and 5.16 show the climatological variance in monthly means of zonally-averaged temperature for October and December. Figures 5.15 and 5.17 show the perturbation variance for zonally-averaged temperature for October and December. The contour levels are on a log scale due to the large range of values. As early as July the perturbation variance is greater than the climatological variance in the equatorial region and at high southern latitudes (not shown). This is clearly the case by October (Figures 5.14 and 5.15). The climatological data shows no significant variance in the equatorial region where the perturbation variance is the greatest, both in October and December. The large perturbation variance in the equatorial region corresponds with the large temperature increases seen in the zonal mean temperature differences.

The only significant climatological variance is in the southern hemisphere polar region between 100 mb and 1 mb. The effect of the perturbation is to enhance the variance in this region. The heating perturbation also produces variance in the northern polar region beginning in October and continuing to grow through December (Figures 5.15 and 5.17). The climatological variance is negligible in this region.

5.3.2 Zonal Wind

The climatological and perturbation variances in the zonally averaged zonal wind for October and December are shown in Figures 5.18 through 5.21. There is more climatological variance in the zonal wind than in the temperature (October had a max of 4 K^2 for temperature and 27 (m/s)^2 for zonal wind). Most of the clima-

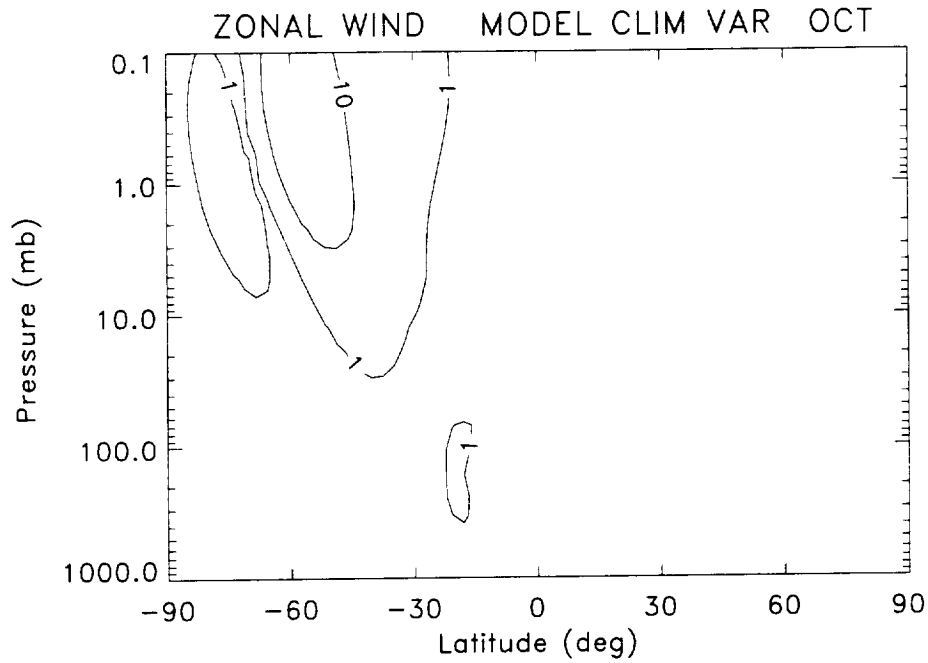


Figure 5.18: Same as Figure 5.14 except for zonal wind. Contour levels are 1, 10, and 100 $(\text{m/s})^2$.

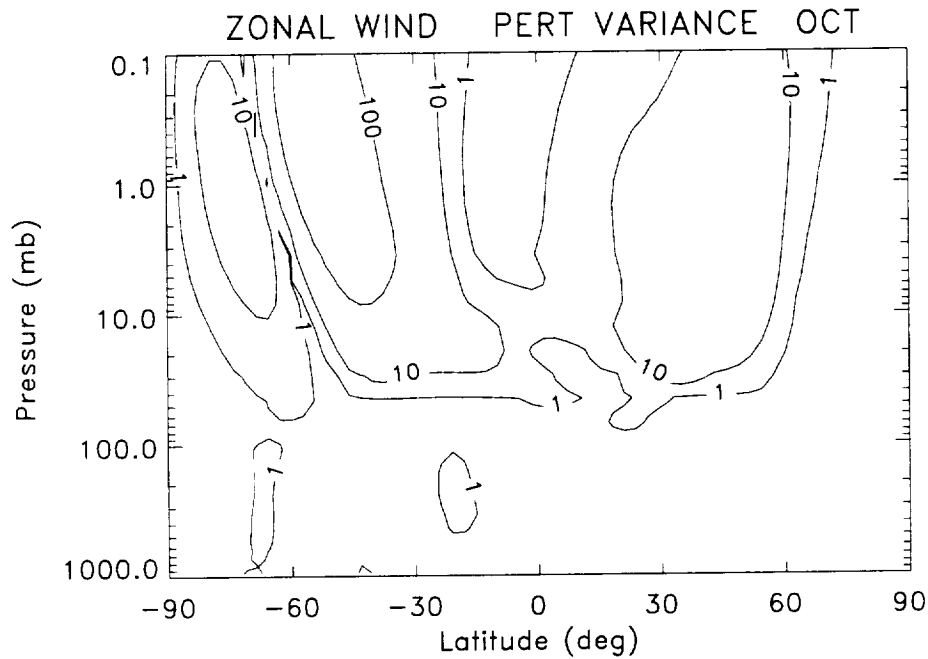


Figure 5.19: Same as Figure 5.15 except for zonal wind. Contour levels are 1, 10, and 100 $(\text{m/s})^2$.

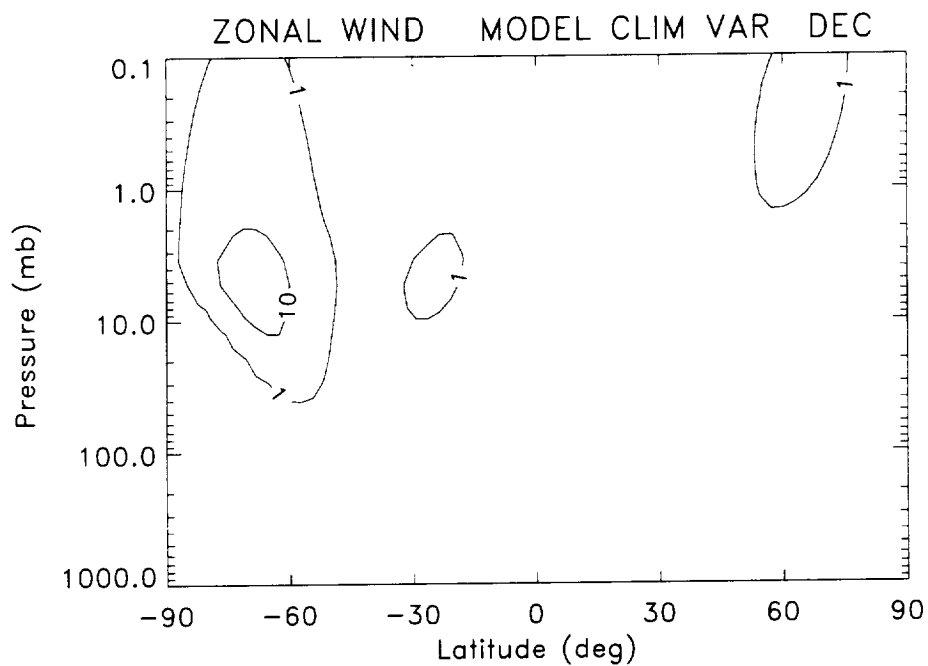


Figure 5.20: Same as Figure 5.18 except for December.

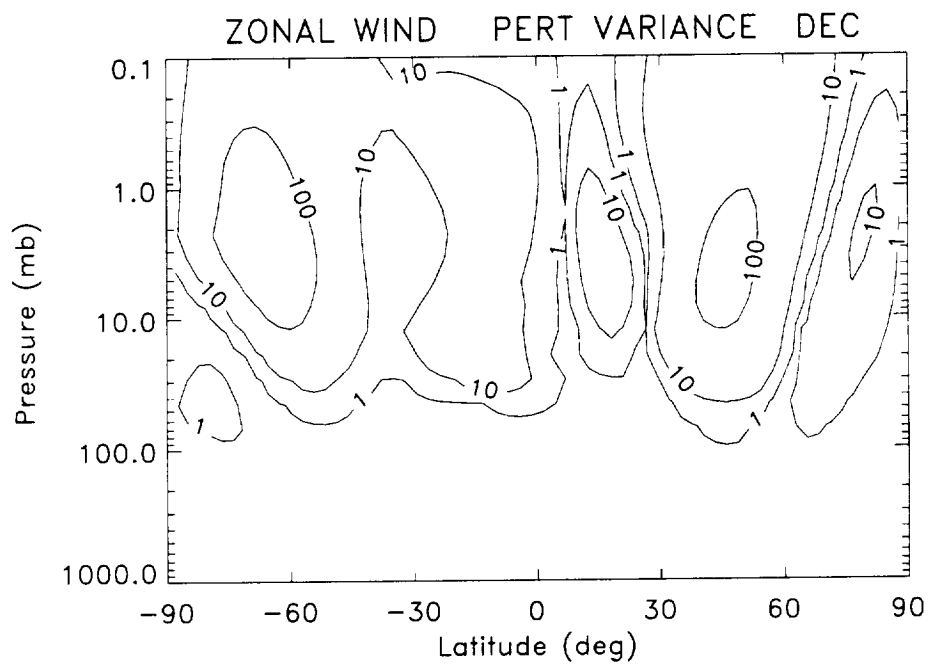


Figure 5.21: Same as Figure 5.19 except for December.

tological variability is in the southern hemisphere for the months considered here (July through December). In December however, some variability appears in the northern hemisphere which may continue to grow as the northern hemisphere winter progresses.

As with the temperature, the largest deviations from the climatological variance is in October. The effect of the additional diabatic heating was to enhance the already present climatological variance in the southern hemisphere and to create significant change in the northern hemisphere. Most of the variability is above 100 mb and centered near 1mb.

5.3.3 Geopotential Height

In Figures 5.22 through 5.25 the climatological and perturbation variances for geopotential height are presented. Most of the variance is in the southern hemisphere above 30 mb. In December, climatological variance begins to become visible in the northern hemisphere at high latitudes above 2 mb. Note that there is no climatological variance in the equatorial region.

Unlike the climatological variance, the perturbation variance is greatest in the equatorial region. This corresponds to where the largest perturbations to the geopotential height occurred (Figures 5.12 and 5.13). In addition, the climatological variance in the polar regions is enhanced well beyond the unperturbed values. All of the significant climatological and perturbation variance is above 100 mb.

5.3.4 Variance in the Real Atmosphere

As shown in [79] variations in the real atmosphere are consistently greater than in the unperturbed model. This is shown for temperature and zonal wind. Monthly zonal means of geopotential height are not shown, however since geopotential height

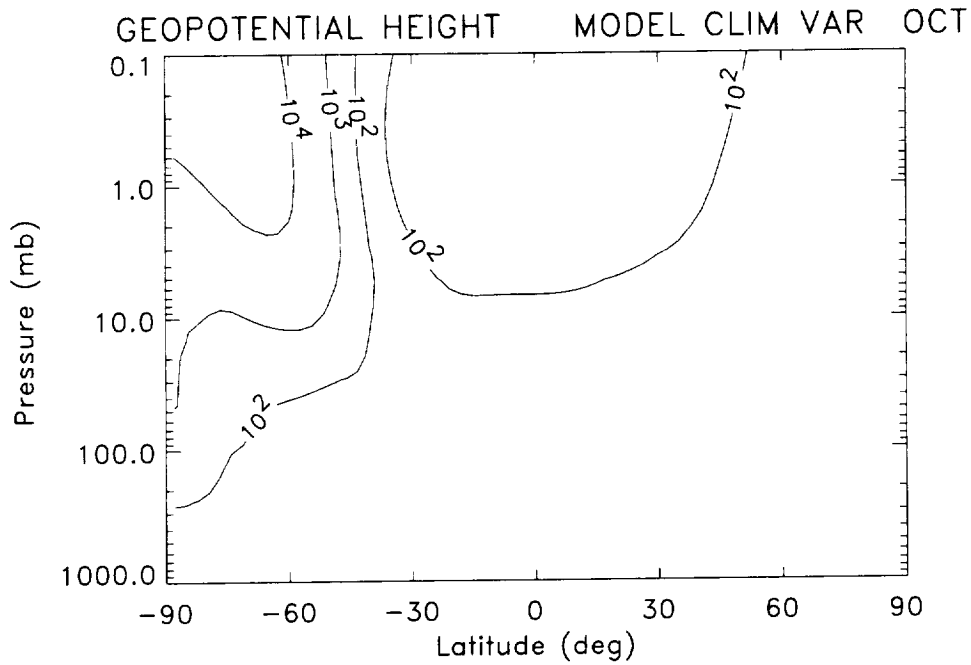


Figure 5.22: Same as Figure 5.14 except for geopotential height. Contour levels are 100, 1000, and 10,000 km².

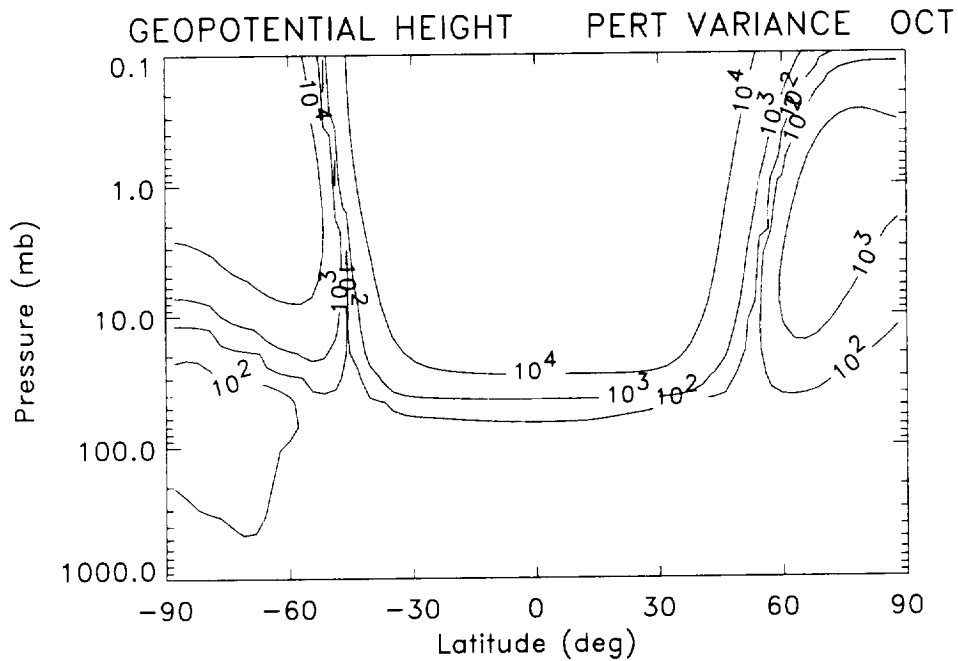


Figure 5.23: Same as Figure 5.15 except for geopotential height. Contour levels are 100, 1000, and 10,000 km².

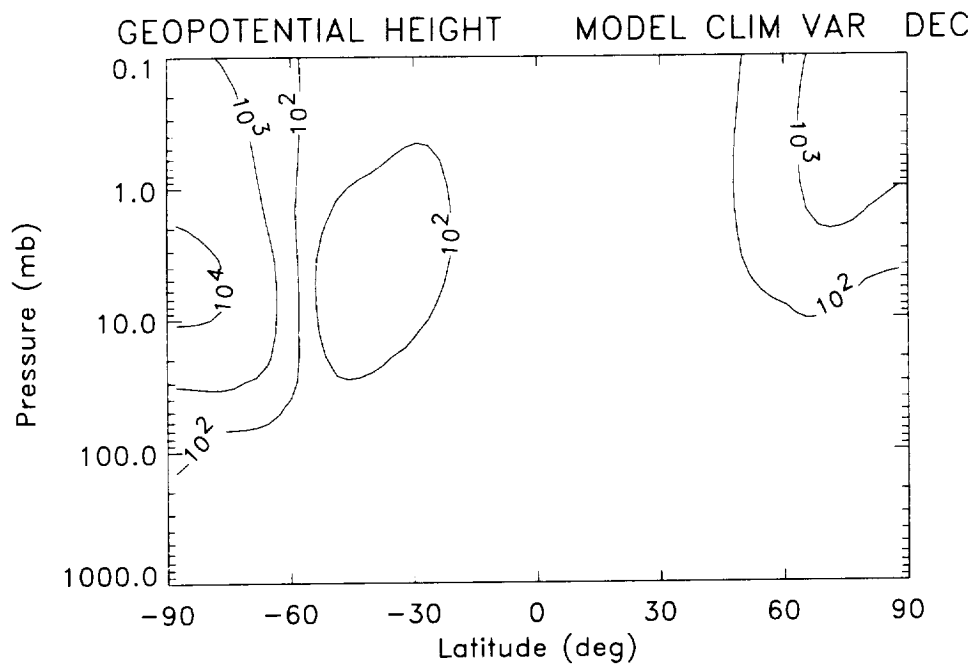


Figure 5.24: Same as Figure 5.22 except for December.

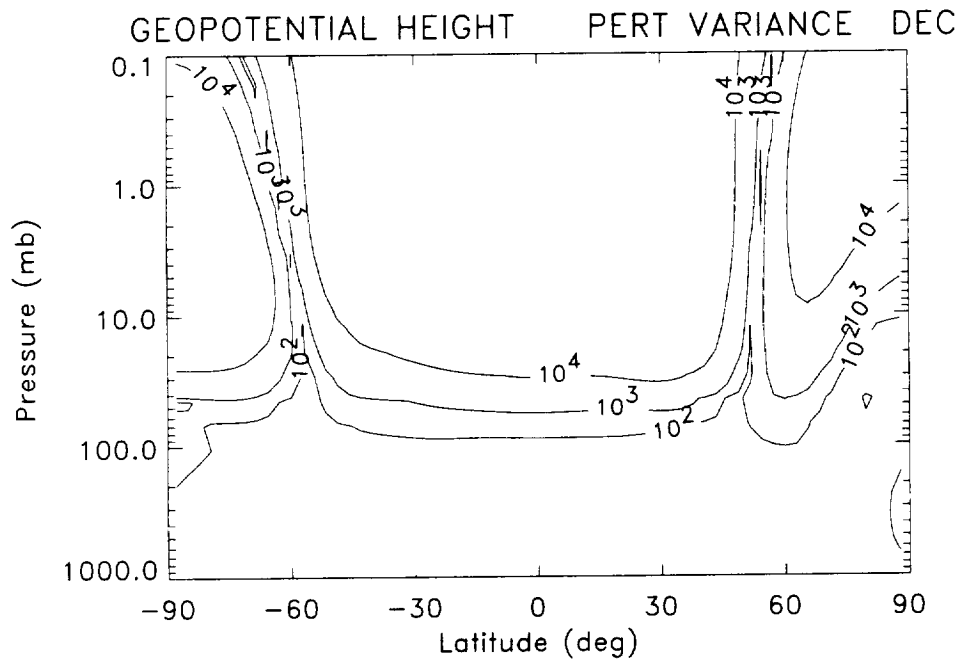


Figure 5.25: Same as Figure 5.23 except for December.

is related to the temperature the same can be concluded for geopotential height.

Comparing the perturbation variance to climatological variance in the real atmosphere yields similar results. For temperature during October, the perturbation variance from the model simulation is greater than climatological variance from the real atmosphere in the equatorial region, but not at high southern latitudes [79]. In December, the perturbation variance from the model simulation is still greater than the variance in the real atmosphere in the equatorial region [79]. However, at higher northern and southern latitudes, climatological variance in the real atmosphere is greater than the perturbation variance in the model simulation [79].

For the zonal wind in October the location of the maximum in the model perturbation variance (between 10 and .1 mb and 30°S and 60°S) the perturbation variance is greater than the actual climatological variance [79]. South of 60°S variance in the real atmosphere is greater than the model perturbation variance. In the equatorial region real atmosphere variance is also greater than the model perturbation variance [79]. In December in the southern hemisphere the model perturbation variance is greater than in the real atmosphere, however in the equatorial region and the northern hemisphere variance in the real atmosphere is greater than the model perturbation variance [79].

From this information it is clear that the unperturbed model does not vary as much as the real atmosphere. It is constrained by the absence of realistic tropospheric physics. As mentioned earlier, the diabatic heating in the troposphere is derived from the FGGE climatology which limits interannual variability. The perturbed variance is clearly greater than the model climatology variance indicating that the heating perturbation had a significant impact on the model simulation. When comparing the model perturbed variance to the variance in the real atmosphere, the equato-

rial temperature response in the model is still significant, however higher latitude temperature changes are not. This is most likely because the GCM will not reflect changes in temperature due to ozone depletion since this model has no chemistry in it (as mentioned earlier).

Concerning the zonal wind, in general the model perturbation variance is greater than the real atmosphere variance in the summer (and to some extent in the spring) hemisphere. This makes sense since in the real atmosphere waves propagate to the stratosphere in the winter and not the summer. The region of the maximum change in the zonal wind is still significant when compared to the variance in the real atmosphere.

5.4 Temporal Evolution

In this section the temporal evolution of certain model parameters is shown as a function of latitude at specified pressure levels and longitudes. As with the zonal mean data, these data are the differences between the perturbed run and the control run, positive values indicating an enhancement in the perturbed simulation, negative values indicating a decrease in the perturbed simulation. The temperature, meridional wind, and geopotential height are shown at 90°E and 270°E , and the zonal wind at 0°E and 180°E . Recall that the location of the initial heating perturbation was at approximately 115°E , traveling westward. The center of the heating perturbation reached 90°E on day 3 of the simulation.

5.4.1 Temperature

The temperature data are shown at the 29 mb level where most of the heating enhancement occurs. Figures 5.26 and 5.27 show that the most significant temperature changes occur in the equatorial region at 29 mb. There is very little response

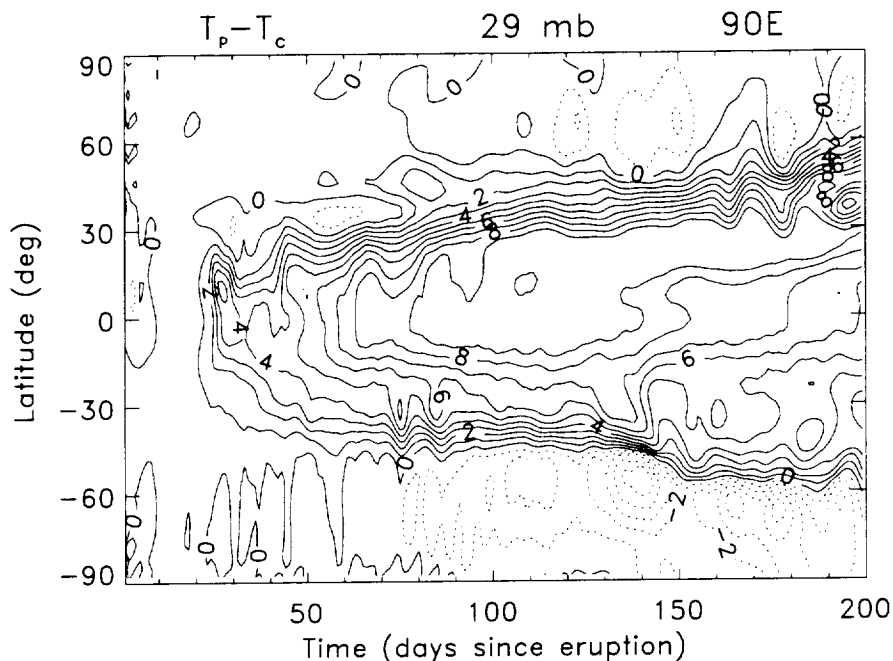


Figure 5.26: Temporal evolution of perturbed temperature minus control temperature at 90°E and 29 mb. Contour interval is 1 K.

the first two weeks of the simulation (corresponding to second half of June). After that time, the perturbation quickly spreads through the low latitudes (between 30°N and S). It is not until around day 80 (early September) that there is a response at the high southern latitudes and even later (late October, about day 130) that there is a response at high northern latitudes. Another feature common to both longitudes is that the largest increases in temperature remain north of the equator for the duration of the simulation. The largest decreases in temperature occur at high southern latitudes at 90°E and high northern latitudes at 270°E.

At higher altitudes which are not shown (2 mb) there is virtually no equatorial response. All the effects of the heating enhancement are felt at mid to high latitudes beginning later in the simulation (early August). The largest decreases in temperature occur at high northern latitudes in December at 90°E. However, at the

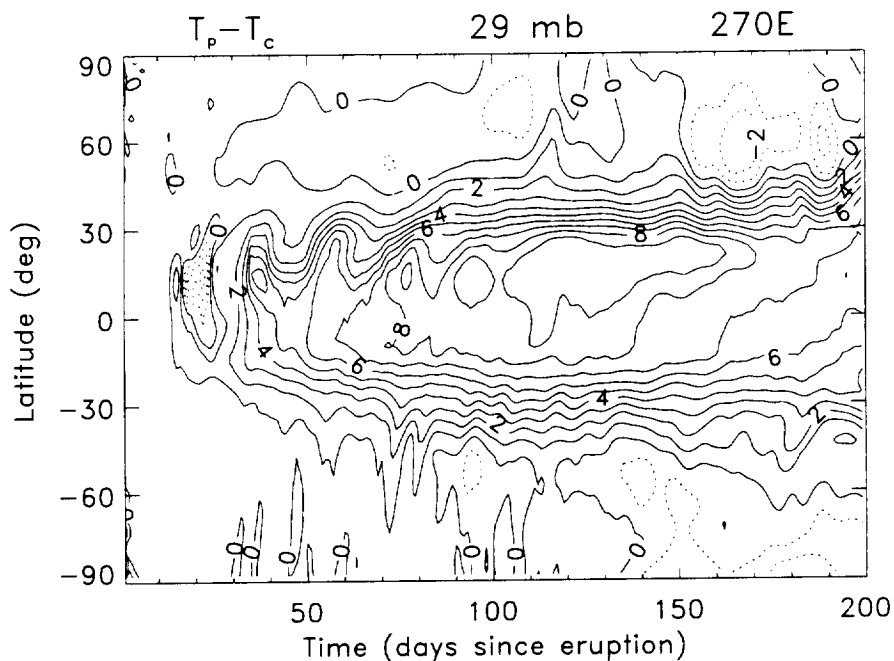


Figure 5.27: Same as Figure 5.26 except at 270°E.

same time and latitude at 270°E there are large temperature increases. The southern hemisphere also alternates between temperature increases and decreases at high latitudes during the second half of the simulation.

5.4.2 Zonal Wind

The temporal evolution of the zonal wind difference at 0°E and 180°E and 19 mb is shown in Figures 5.28 and 5.29. The longitudes chosen here are different than those for temperature, meridional wind, and geopotential height because of the interesting comparison of equatorial winds at these longitudes (subject of future discussion). In general the largest changes to the zonal wind occur at the higher model levels. For example at 29 mb the maximum change in the zonal wind is 6 to 8 m/s but at 2 mb the maximum change greater than 20 m/s. This is in general agreement with the zonal mean figures. Some of the interesting features can be best viewed by examining

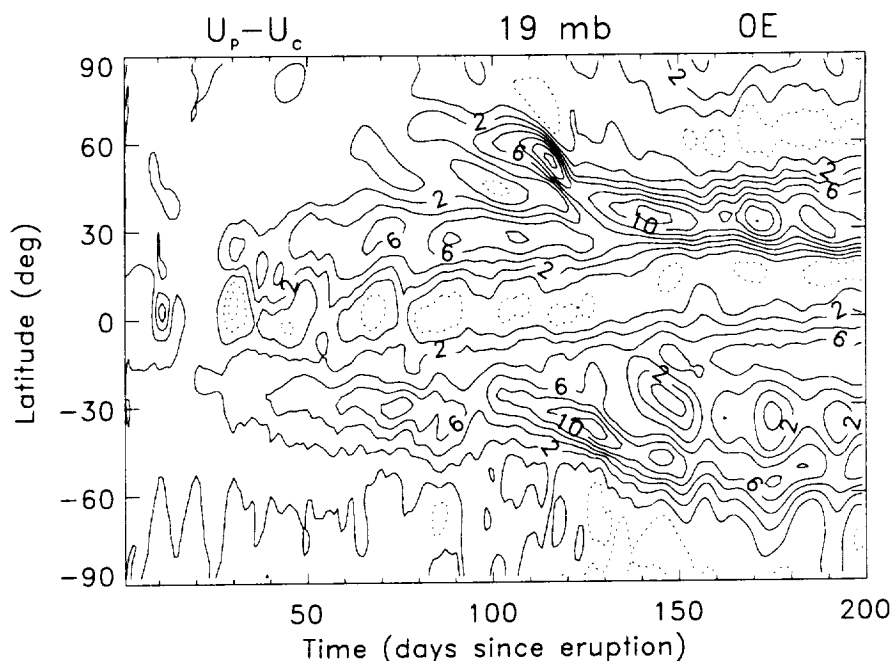


Figure 5.28: Temporal evolution of perturbed zonal wind minus control zonal wind at 0°E and 19 mb. Contour interval is 2 m/s.

the difference between the perturbed and control zonal winds at 0°E and 180°E and 19 mb.

During the early part of the simulation (less than day 50), the changes to the zonal wind are confined to between 45° N and S. At the equator the values alternate between positive and negative both at 180°E and 0°E (though less dramatically at 0°E). At 0°E in the equatorial region the dominant feature is a perturbed zonal wind that is more easterly than the zonal wind in the control run (negative perturbation) after day 50 (early August). Conversely, at 180°E, the dominant feature in the equatorial region is westerly (positive) influence from the heating perturbation.

Both longitudes show a westerly perturbation at mid-latitudes in the northern hemisphere beginning day 120 (mid October). At 180°E this region of more westerly zonal wind is a bit farther north than at 0°E.

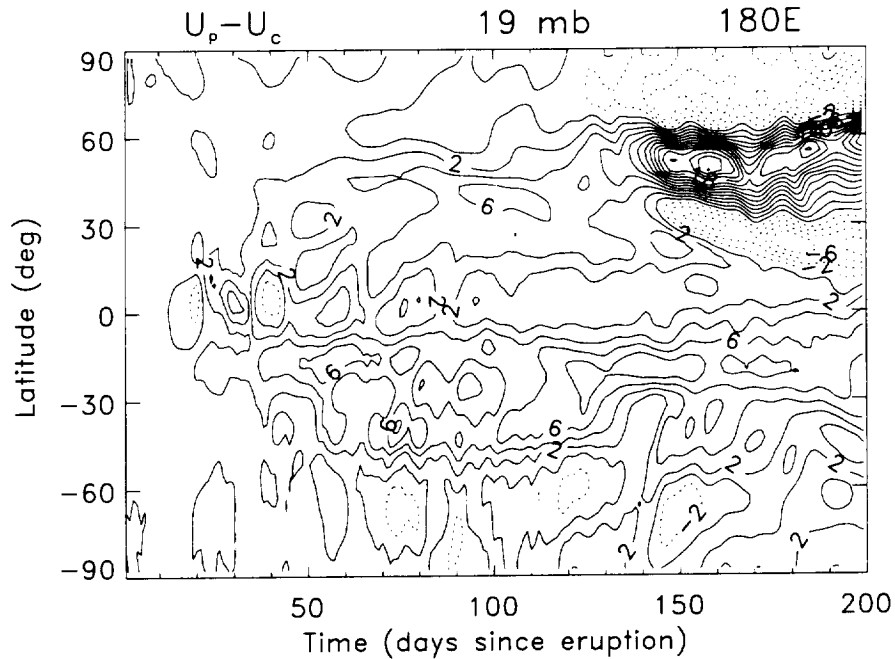


Figure 5.29: Same as Figure 5.28 except at 180°E.

At 180°E poleward of 60°N the change in the zonal wind is an easterly influence. This also occurs at 0°E, however, the perturbation is not as strong and switches to a westerly perturbation at 75°N. Both longitudes show the alternating between positive and negative changes to the zonal wind with respect to latitude beginning at about day 130 in the northern hemisphere.

The southern hemisphere is more disorganized than the northern hemisphere. The changes to the zonal wind are for the most part an increase (indicating a westerly influence). This westerly influence goes all the way to the south pole at 180°E and to about 70°S at 0°E.

As pressure decreases, the equatorial response weakens while the extra-tropical response strengthens. At 2 mb (not shown) there are bands of strong westerly perturbations flanked easterly perturbations at higher and lower latitudes.

5.4.3 Meridional Wind

Even though the changes in the zonal mean meridional wind showed virtually no response to the heating perturbation, by examining the temporal evolution of the meridional that is not zonally-averaged, a response can be seen. Shown in Figures 5.30 and 5.31 are the changes in the meridional wind field at 19 mb, 90°E and 270°E . These changes are not as dramatic as those in the zonal wind. There is essentially no change in the meridional wind at low latitudes (equator ward or 30°N and S), and very little response at any latitude prior to day 80 (corresponding to early August) in the southern hemisphere and prior to day 120 in the northern hemisphere. At 90°E the change in the meridional wind is predominately negative (a southward perturbation) in the northern hemisphere and alternates between positive and negative in the southern hemisphere. At 270°E the northern hemisphere response is weaker and predominately positive while the southern hemisphere alternates between positive and negative.

The changes in the meridional wind at 2 mb (still 90°E and 270°E) show some interesting similarities and differences. The data at this level is shown in Figures 5.32 and 5.33. Perturbations to the meridional wind are first visible in the high latitude southern hemisphere and later at high northern latitudes. An interesting difference is that changes in the meridional wind at 2 mb occur earlier in the simulation than the changes at 19 mb in both hemispheres (by about 40 days in the northern hemisphere and 30 days in the southern hemisphere). At 90°E the perturbation to the meridional wind is larger in magnitude and alternates between positive and negative, though weakly after day 180. At 270°E the southern hemisphere change in the meridional wind is initially somewhat noisy but becomes more organized around day 100. At this time the perturbation to the meridional wind is negative (northerly) and becomes

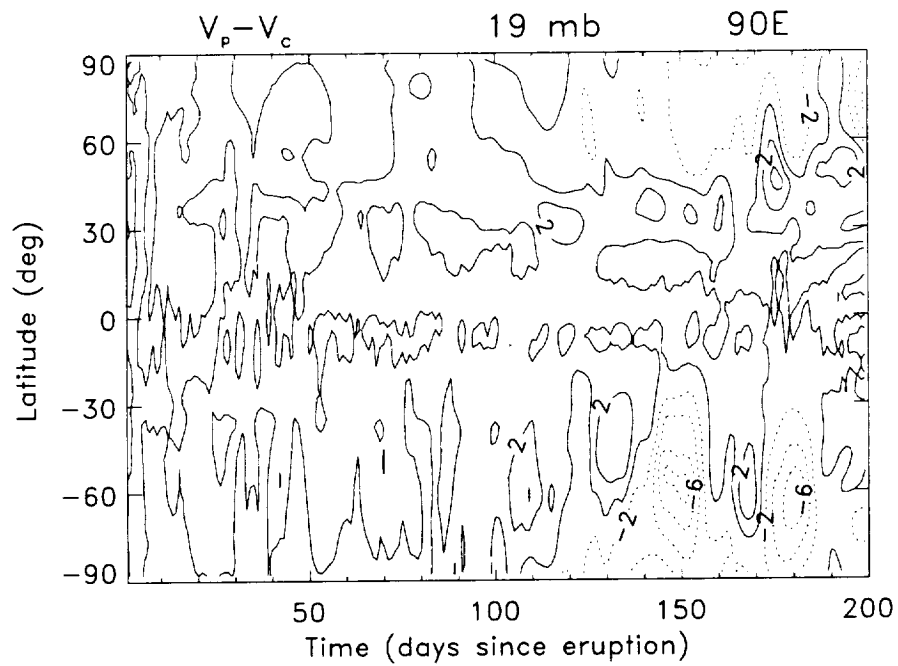


Figure 5.30: Temporal evolution of perturbed meridional wind minus control meridional wind at 90°E and 19 mb. Contour interval is 2 m/s.

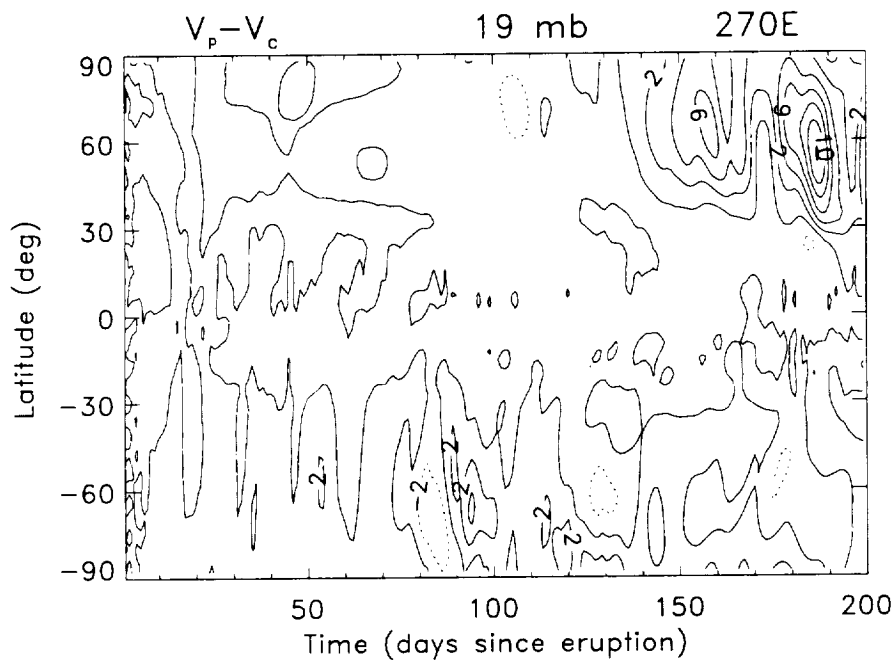


Figure 5.31: Same as Figure 5.30 except at 270°E.

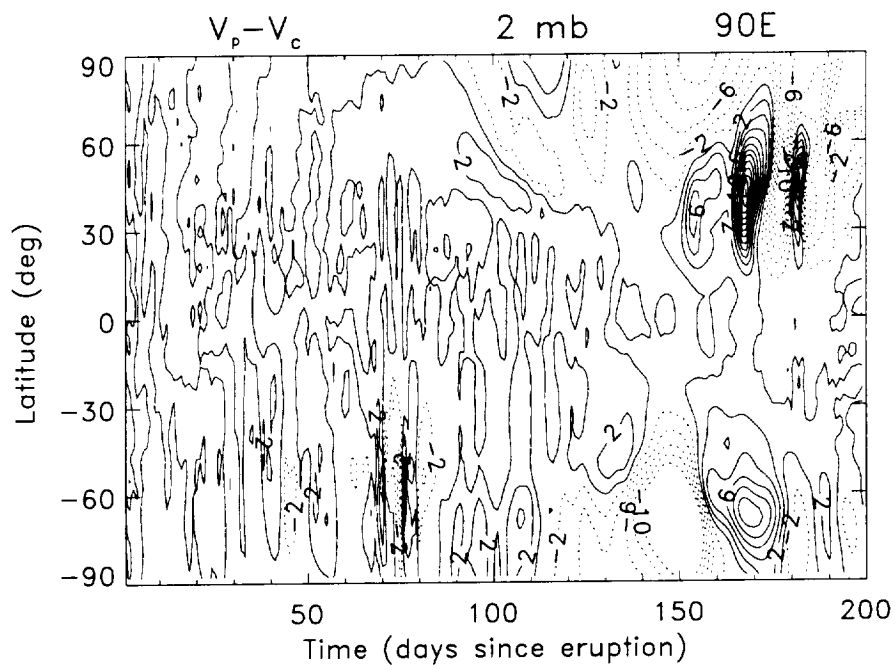


Figure 5.32: Temporal evolution of perturbed meridional wind minus control meridional wind at 90°E and 2 mb. Contour interval is 2 m/s.

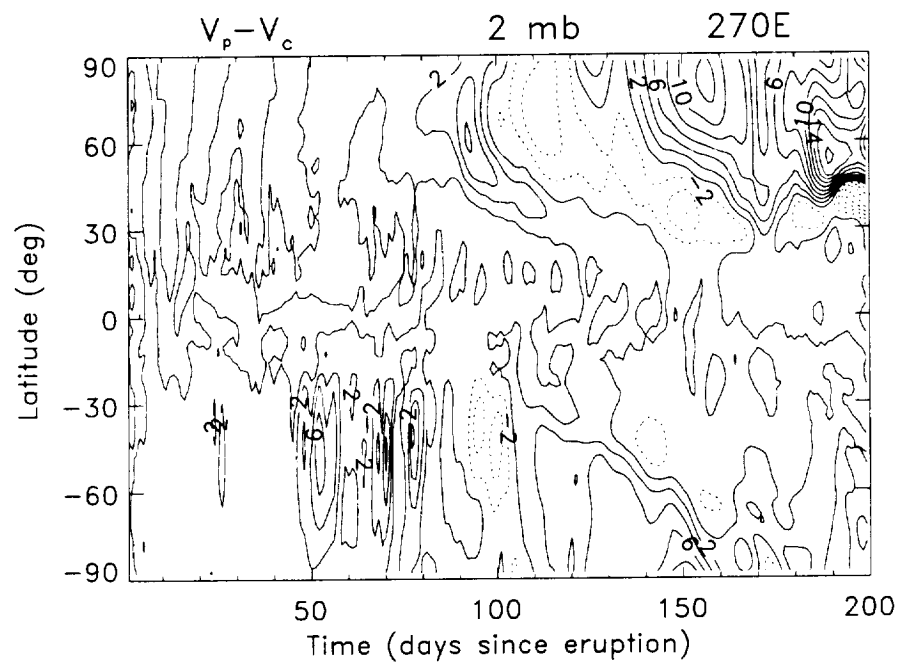


Figure 5.33: Same as Figure 5.32 except at 270°E.

positive (southerly) after about 10 days. After day 160 the southern hemisphere change in the meridional wind is weak at 270°E .

In the northern hemisphere at 2 mb, 90°E from day 80 to 150 the change in the meridional wind is similar to that at 270°E although weaker. After day 150 there are large changes in the meridional wind, both positive and negative, but they are not as well organized. At 270°E the changes in the meridional wind after day 80 are interesting. The changes alternate between positive and negative and migrate equator ward with time (ending at about 30°N).

5.4.4 Geopotential Height

As with the zonal and meridional winds, the changes in the geopotential height increase as pressure decreases. Figures 5.34 and 5.35 show the changes in geopotential height due to the enhanced diabatic heating at 19 mb, 90°E and 270°E . The dominant feature is the gradual increase in perturbed geopotential height in the tropical region beginning about day 30 (mid July). This region of enhanced geopotential height is biased toward the north. The highest values are between 15°S and 30°N at 270°E and between 15°S and 45°N at 90°E . At 90°E the enhancement in geopotential height is greater, most noticeably so beginning day 120. Changes to the geopotential height spread to high and polar latitudes by day 70 at 19 mb (somewhat sooner at lower pressure levels). To the south of the tropical enhancement the impact of the perturbation on geopotential height is to increase it at 270°E and decrease Z at 90°E . In the northern mid and high latitudes, the perturbations to the geopotential height are weak and unorganized.

At 2 mb (not shown) the main difference from the 19 mb figures is a stronger enhancement of geopotential height in the low latitudes and a considerably stronger

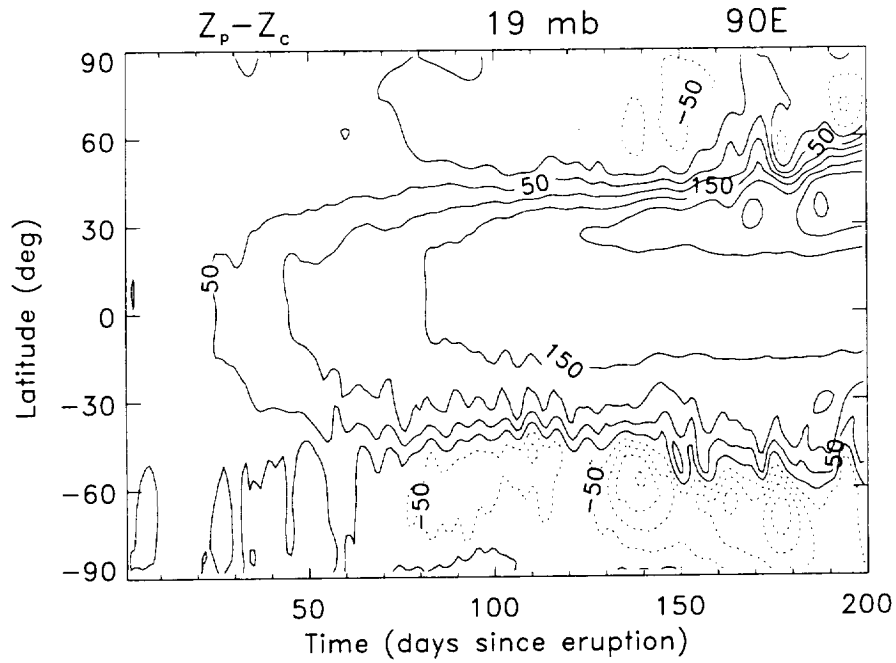


Figure 5.34: Temporal evolution of perturbed geopotential height minus control geopotential height at 90°E and 19 mb. Contour interval is 25 km.

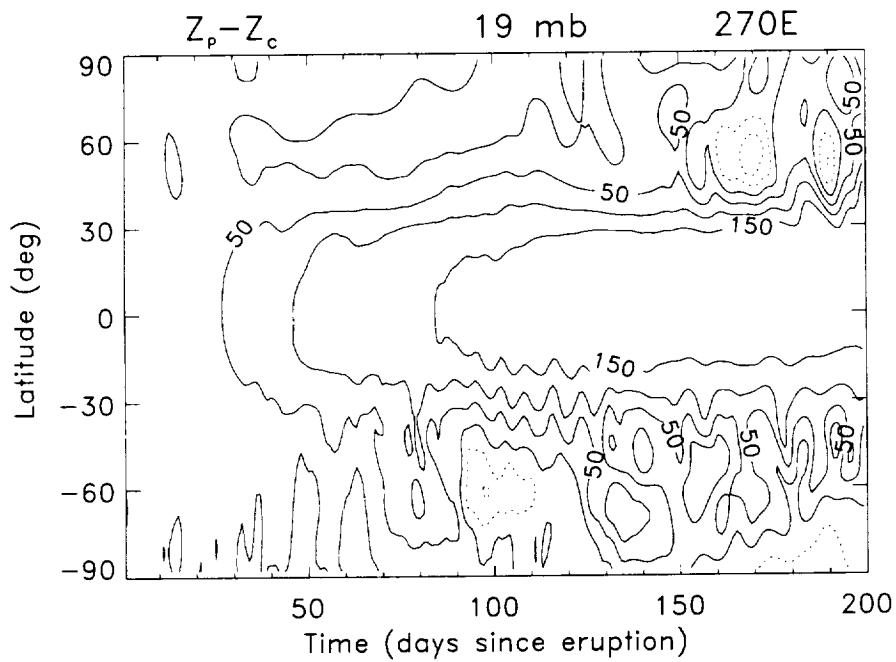


Figure 5.35: Same as Figure 5.34 except at 270°E.

decrease in geopotential height at high southern latitudes at 90°E . The high northern latitudes at 90°E show a much greater impact on geopotential height (predominately a decrease). At 270°E , in the southern hemisphere the enhancement in geopotential height is greater. In addition there is a large swath of decreased geopotential height. To the north at 270°E the enhancement to geopotential height is now greater than the low latitude enhancement.

5.5 Wave Variance

The wave variance is a measure of the amount of wave activity present in the model. It describes the degree to which a given model parameter varies from its zonal mean. The wave variances of temperature, zonal wind, meridional wind, and geopotential height are presented for October and December. July is not shown since the impact of the enhanced diabatic heating on the wave variance was small.

5.5.1 Temperature

Figures 5.36 through 5.39 illustrate the monthly mean wave variance for the control and perturbed simulations. Monthly mean data is shown for conciseness, however the evolution of the wave variance throughout July, October, and December was investigated and will be discussed. During July the wave variance is only present in the southern hemisphere with control and perturbed values being similar. During October the wave variance is biased toward the southern hemisphere. The geographical coverage of the control and perturbed wave variances is similar as is the trend of a decrease in magnitude through October. However, the magnitude of the control wave variance is consistently greater than the wave variance for the perturbed simulation.

During December the location of the wave variance begins shifting to the northern

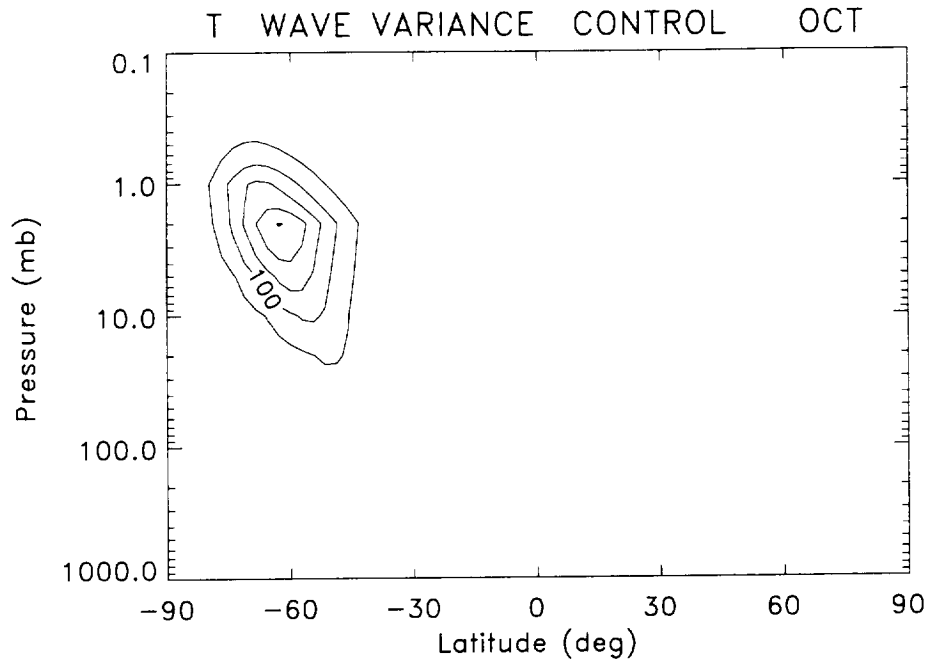


Figure 5.36: October monthly mean of the temperature wave variance for the control simulation. The contour interval is 50 K^2 .

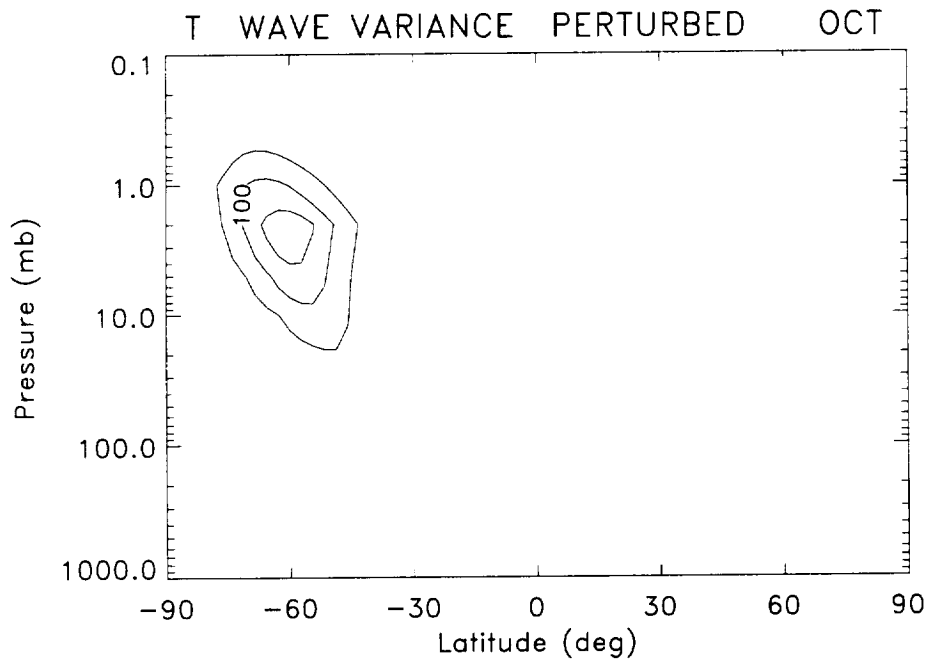


Figure 5.37: Same as Figure 5.36 except for the perturbed simulation.

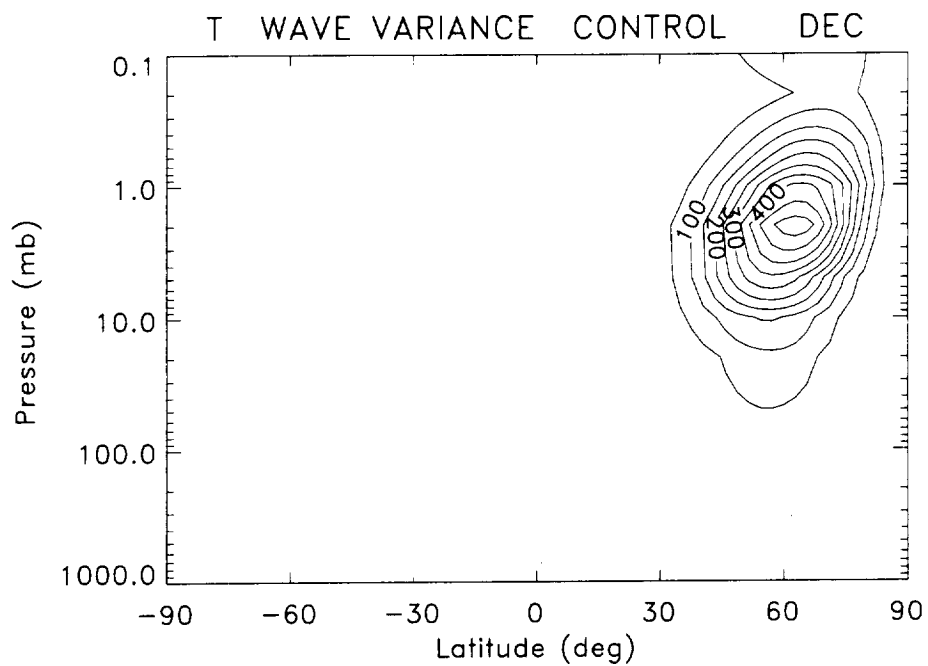


Figure 5.38: December monthly mean of the temperature wave variance for the control simulation. The contour interval is 50 K^2 .

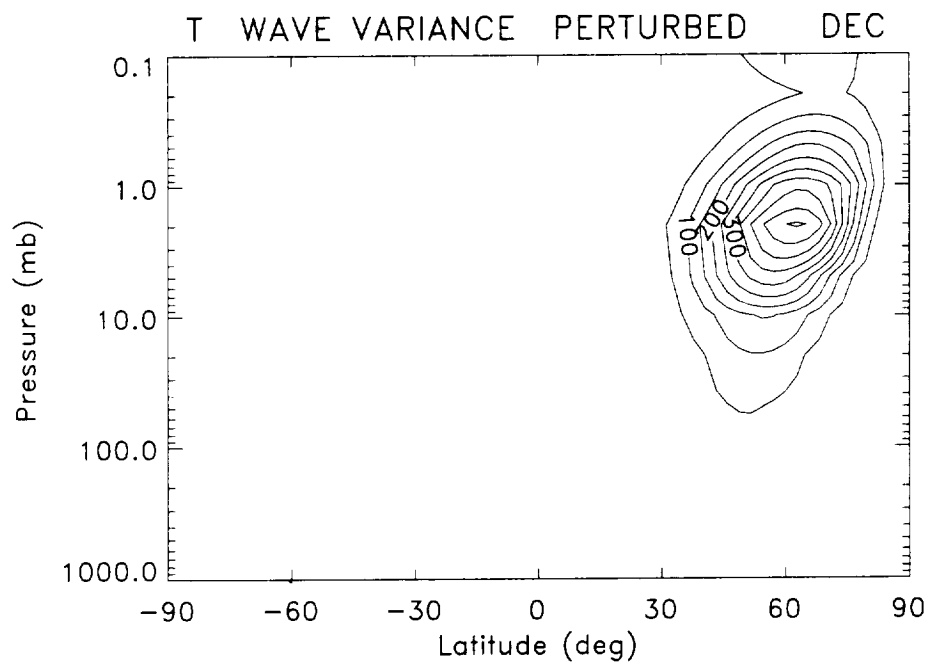


Figure 5.39: Same as Figure 5.38 except for the perturbed simulation.

hemisphere and increasing in magnitude steadily and quickly through December. Again, the geographical coverage for both control and perturbed simulations is very similar. During the last part of December the perturbed wave variance increases more than the control (prior to that it was lower). The pressure level of the maximum remains steady at 2 mb.

5.5.2 Zonal Wind

In Figures 5.40 through 5.43 the October and December monthly mean wave variances are shown for the control and perturbed simulations. The geographical coverage is similar for the control and perturbed runs, however the magnitude of the maximum is greater for the control run. During October, most of the wave activity begins in the southern hemisphere but as the month progresses the southern hemisphere levels decrease while the northern hemisphere levels increase. By December, there is virtually no wave variance in the southern hemisphere and the variance in the northern hemisphere is quite large. During December the effect of the enhanced diabatic heating is to decrease the wave activity even more than in October.

5.5.3 Meridional Wind

During October the majority of the wave activity is at high southern latitudes above 10 mb for both control and perturbed simulations (Figures 5.44 and 5.45). However, October is a transition month for dynamical quantities and as the days progress the level of wave activity in the southern hemisphere decreases while it increases in the northern hemisphere. By the end of October the wave variance in the northern hemisphere is greater than the wave variance in the southern hemisphere. In addition, the magnitude of the variance is consistently greater in the control run than in the perturbed run.

During December (Figures 5.46 and 5.47) the wave variance in the northern hemisphere increases dramatically (by an order of magnitude). The variance is still located at high northern latitudes and above 10 mb for the most part. As in October, the effect of the enhanced heating in the perturbed simulation is to decrease the wave variance.

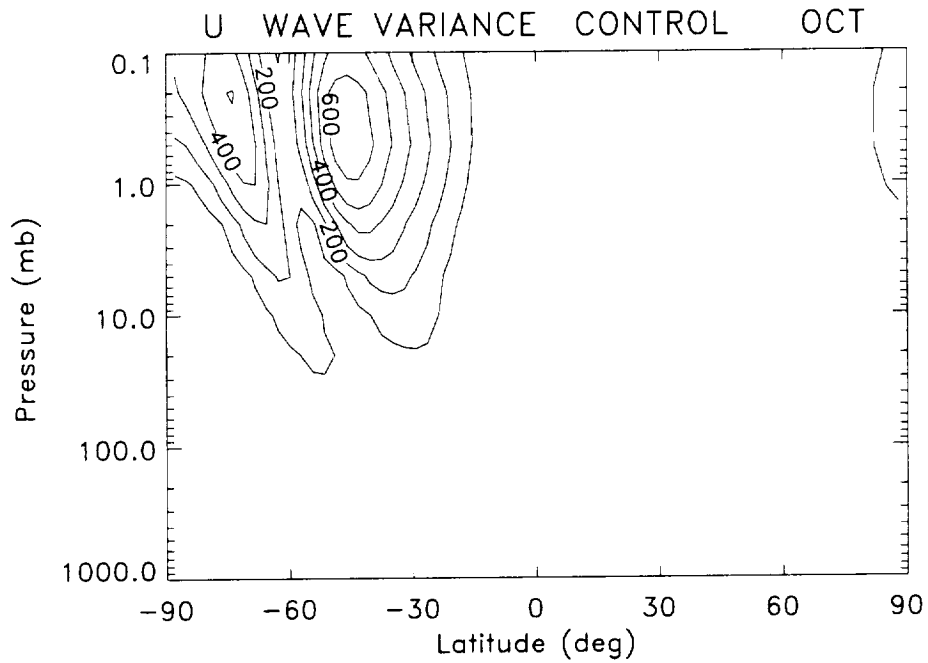


Figure 5.40: October monthly mean of the zonal wind wave variance for the control simulation. The contour interval is $100 (\text{m/s})^2$.

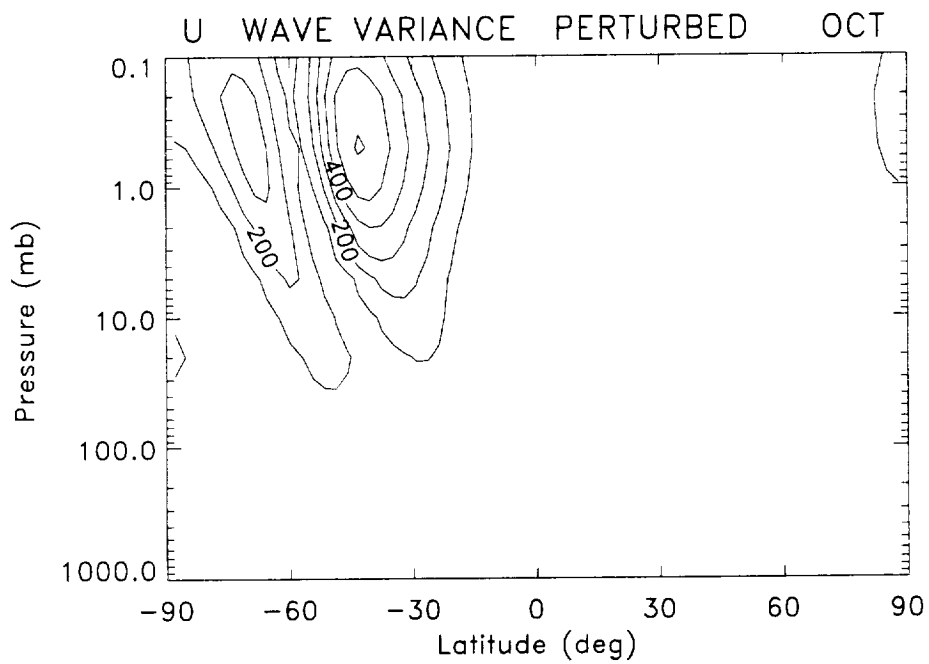


Figure 5.41: Same as Figure 5.40 except for the perturbed simulation.

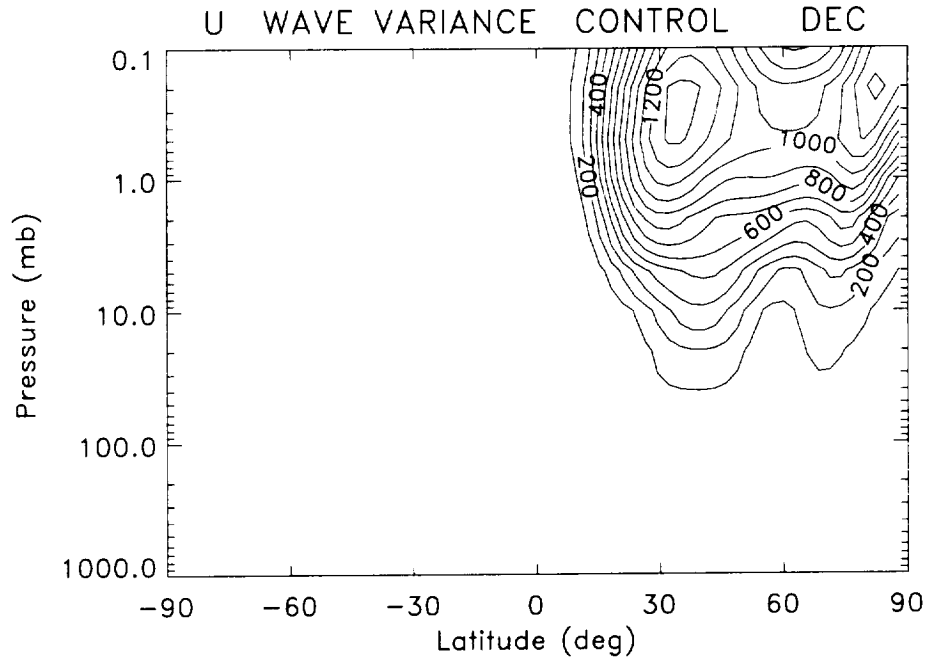


Figure 5.42: December monthly mean of the zonal wind wave variance for the control simulation. The contour interval is 100 (m/s)².

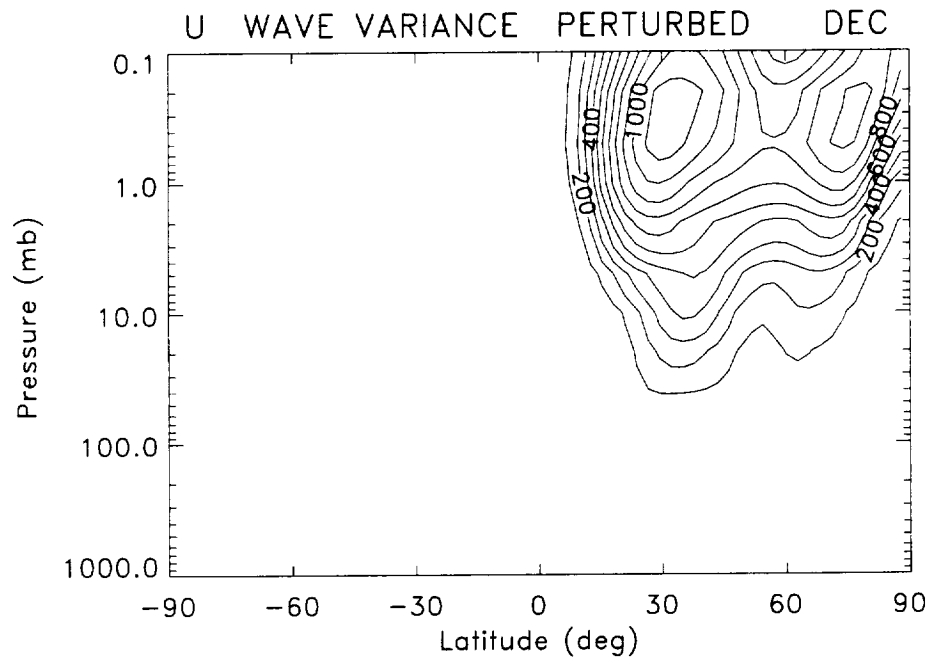


Figure 5.43: Same as Figure 5.42 except for the perturbed simulation.

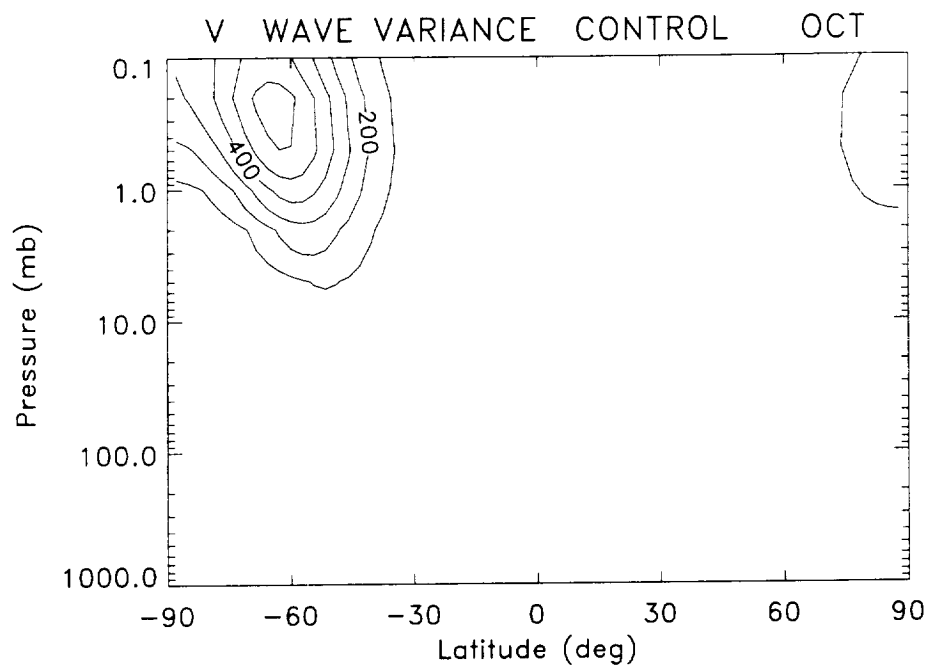


Figure 5.44: October monthly mean of the meridional wind wave variance for the control simulation. The contour interval is 100 (m/s)².

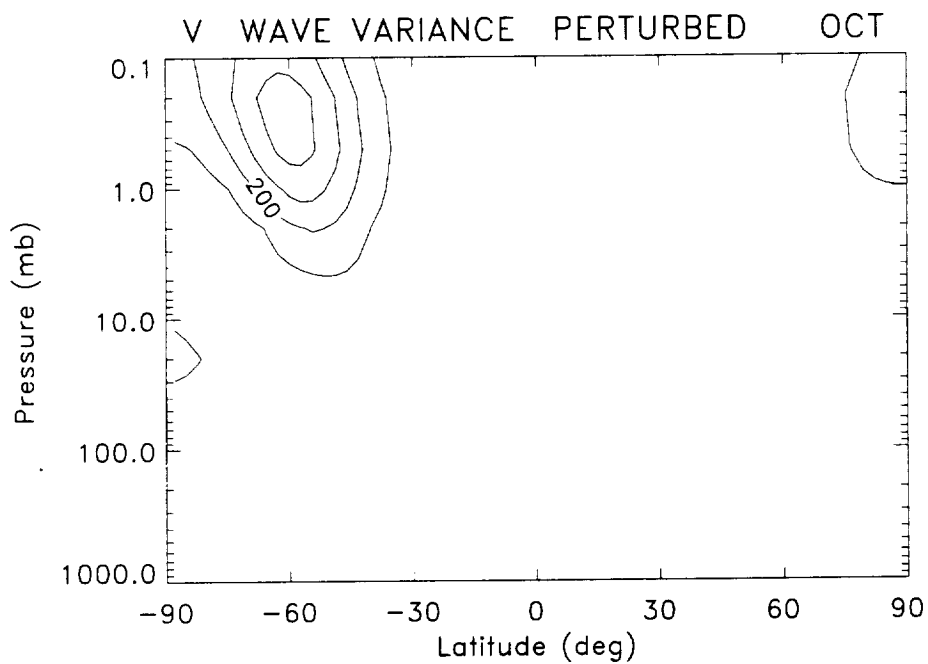


Figure 5.45: Same as Figure 5.44 except for the perturbed simulation.

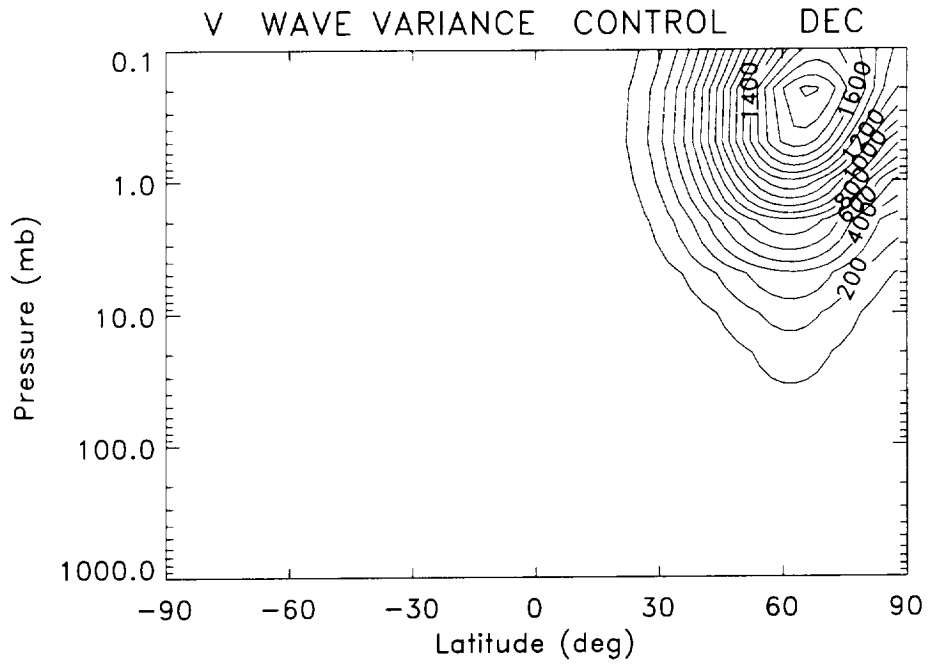


Figure 5.46: December monthly mean of the meridional wind wave variance for the control simulation. The contour interval is 100 (m/s)².

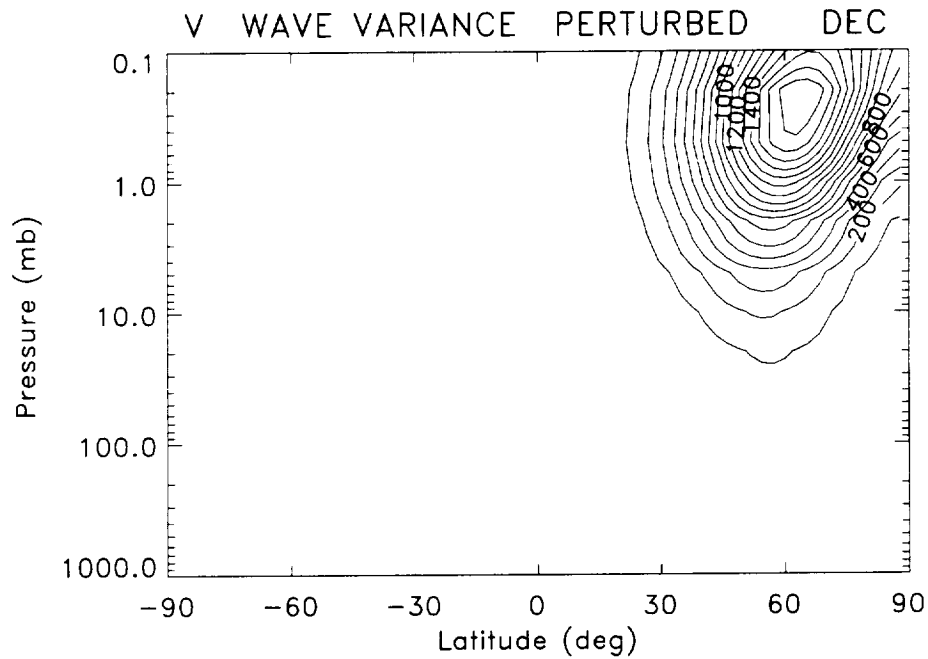


Figure 5.47: Same as Figure 5.46 except for the perturbed simulation.

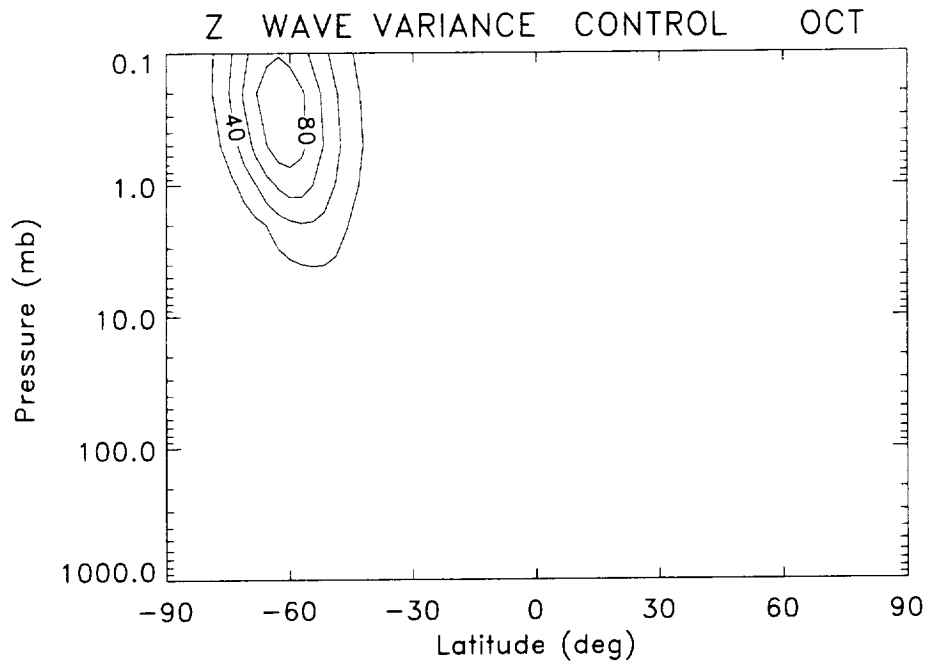


Figure 5.48: October monthly mean of the geopotential height wave variance for the control simulation. The contour interval is 20 km^2 .

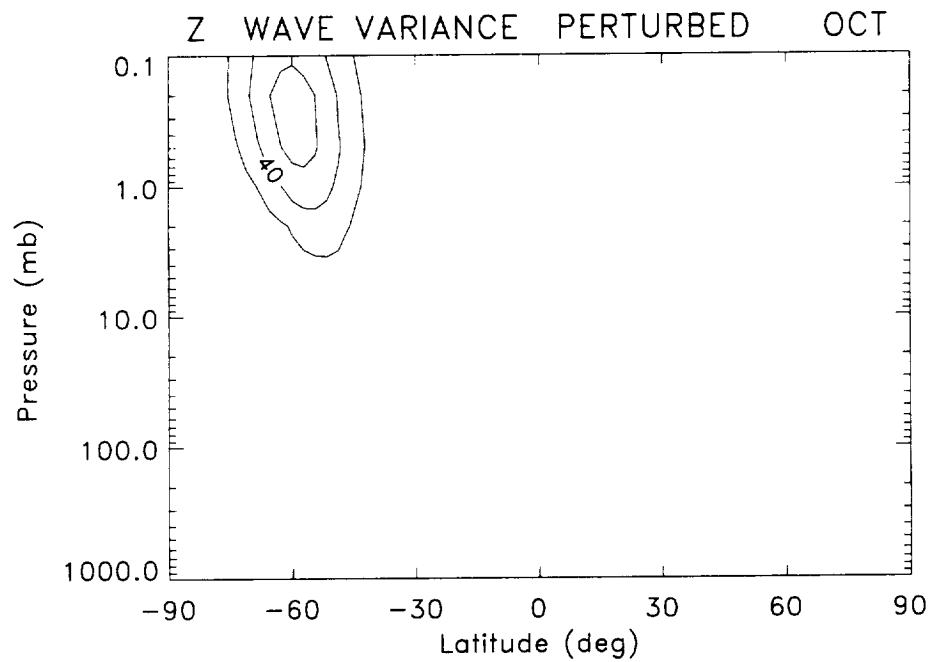


Figure 5.49: Same as Figure 5.48 except for the perturbed simulation.

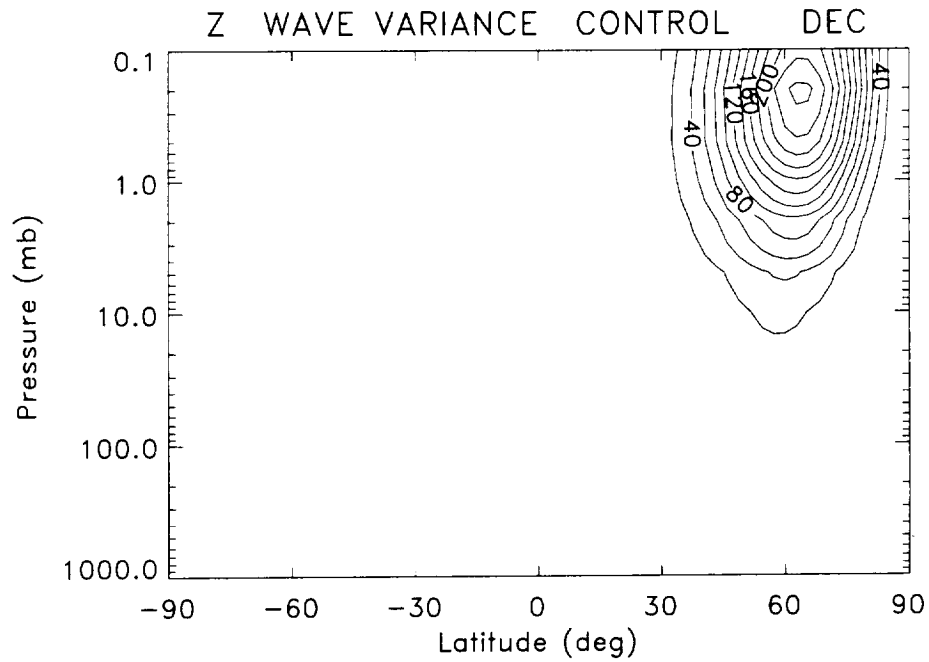


Figure 5.50: December monthly mean of the geopotential height wave variance for the control simulation. The contour interval is 20 km².

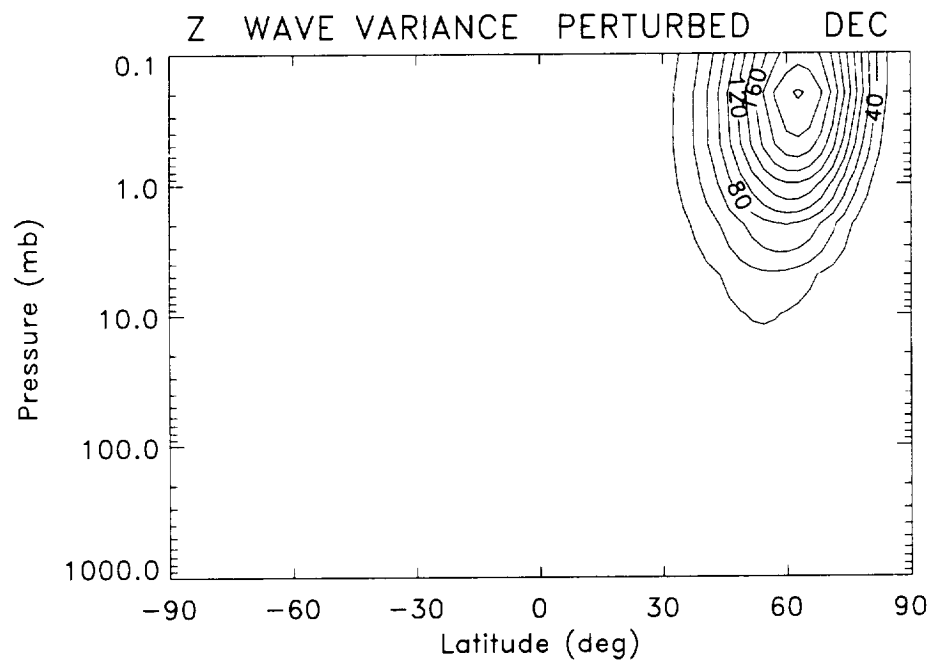


Figure 5.51: Same as Figure 5.50 except for the perturbed simulation.

5.5.4 Geopotential Height

Similar to the trend seen in the temperature, zonal wind, and meridional wind, the geopotential height wave variance is also in transition during October (Figures 5.48 and 5.49). The maximum in the wave variance shifts from the southern hemisphere to the northern hemisphere. Also consistent with the other model parameters, the control wave variance is greater than the perturbed wave variance.

During December (Figures 5.50 and 5.51), the wave variance in the northern hemisphere continues to grow and is confined to high northern latitudes above 10 mb. Up until the end of December control wave variance is greater than perturbed wave variance, when a switch occurs and the perturbed values are greater than the control values.

5.6 Conclusions

The zonal mean difference figures (5.1 through 5.13) showed large changes in temperature, zonal wind, and geopotential height due to the diabatic heating enhancement. By examining the climatological and perturbation variances in the monthly means of temperature, zonal wind, and geopotential height it is clear that the changes to these quantities seen in the zonal mean difference (Figures 5.1 through 5.13) are significant. These perturbations lie well outside the normal annual variations in the model data. Therefore, the enhanced diabatic heating included in the LaRC GCM has a non-trivial effect on model parameters. These changes include a strengthened equator to pole temperature gradient (increased by 50% in October and 25% in December), and enhanced zonal mean circulation (by about 13%). In addition, Figures 5.36 through 5.51 show how the wave activity in the model was weakened by the diabatic heating perturbation. The mechanism by which the heating pertur-

bation weakens the wave variance is not completely understood and further analysis is beyond the scope of this dissertation.

This chapter illustrated the changes in modeled quantities which resulted from the heating enhancement. The changes were not only significant when compared to the control run, but also significant when compared to model climatology. The next step is to address meteorological changes in the atmosphere following the eruption of Mt. Pinatubo and compare those changes to model results.

CHAPTER VI

COMPARISON OF MODEL RESULTS AND OBSERVATIONAL DATA

This chapter examines the model results hydrogen fluoride, temperature, and ozone changes and how they compare to observational data.

6.1 Hydrogen Fluoride

The initialization of hydrogen fluoride was described in Chapter III and an analysis of the control HF distribution was described in Chapter IV. This section focuses on the changes in HF resulting from the diabatic heating enhancement. As discussed in the introduction, the intention was to use changes in the modeled HF distribution due to the perturbation to investigate the HALOE HF data and hopefully make some conclusions about perturbations to stratospheric circulation. Unfortunately, this was not possible since there were some problems with the modeled hydrogen fluoride distribution that did not become evident until this analysis was attempted. The following is a discussion of the shortcomings of the HF distribution.

In general, changes in the HF distribution are expected to be most evident during the winter when waves can propagate upward into the stratosphere. Since the simulation began in June, we would first expect to see changes in the southern hemisphere,

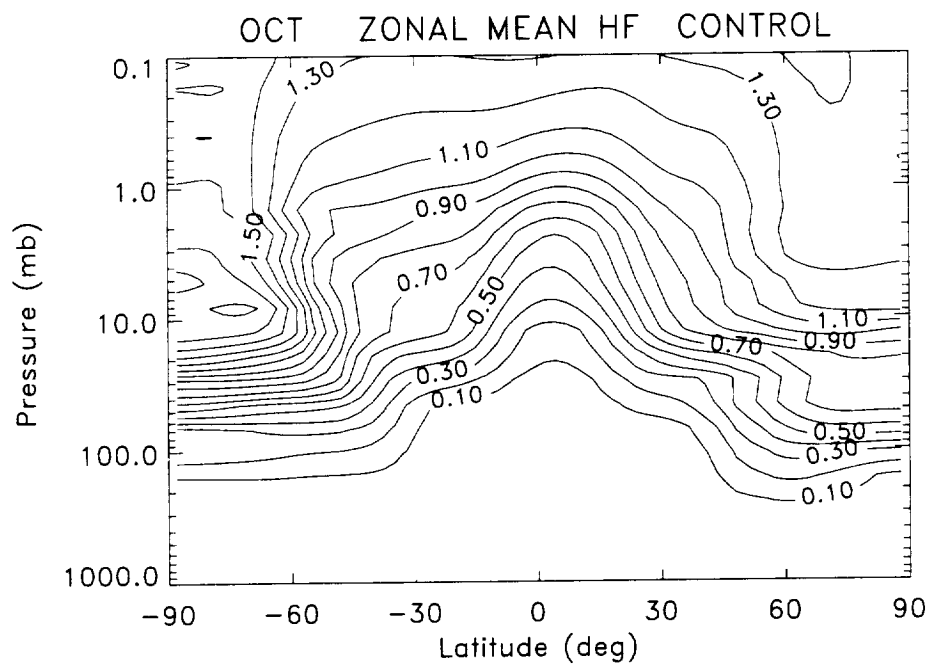


Figure 6.1: October monthly average of hydrogen fluoride for the control case.

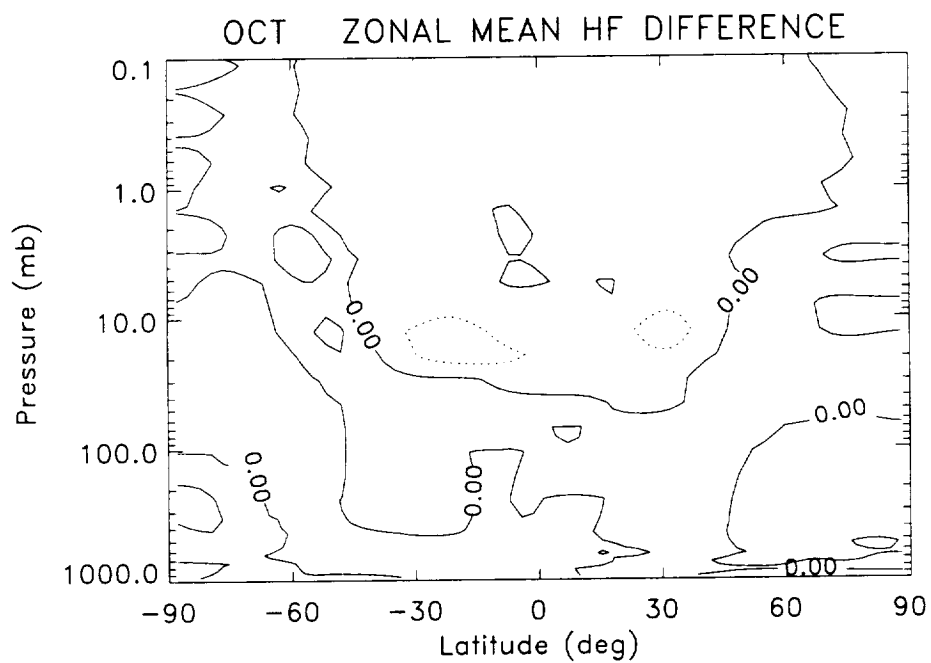


Figure 6.2: October monthly average for the zonal mean hydrogen fluoride difference.

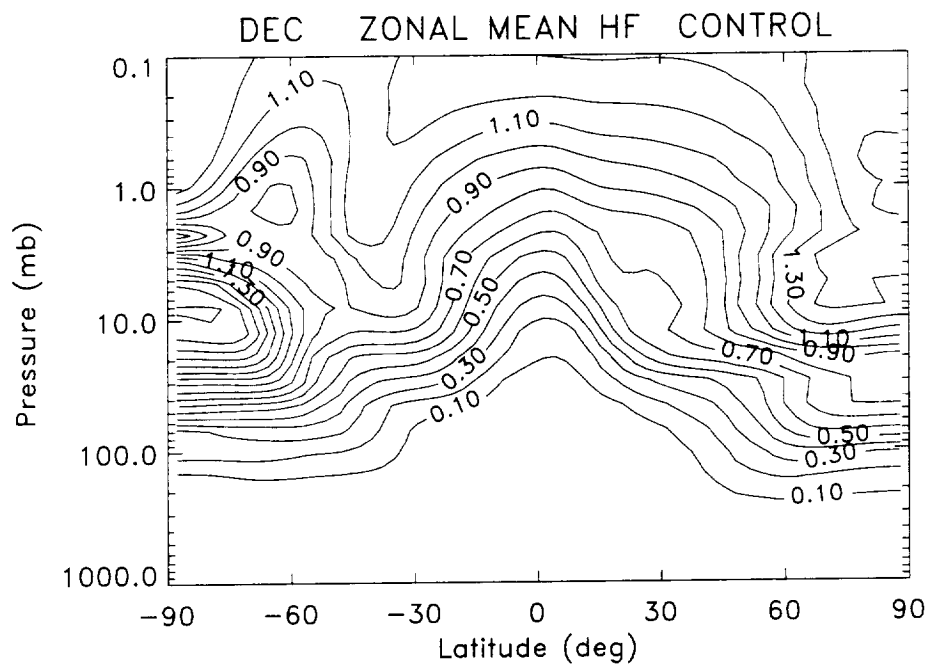


Figure 6.3: December monthly average of hydrogen fluoride for the control case.

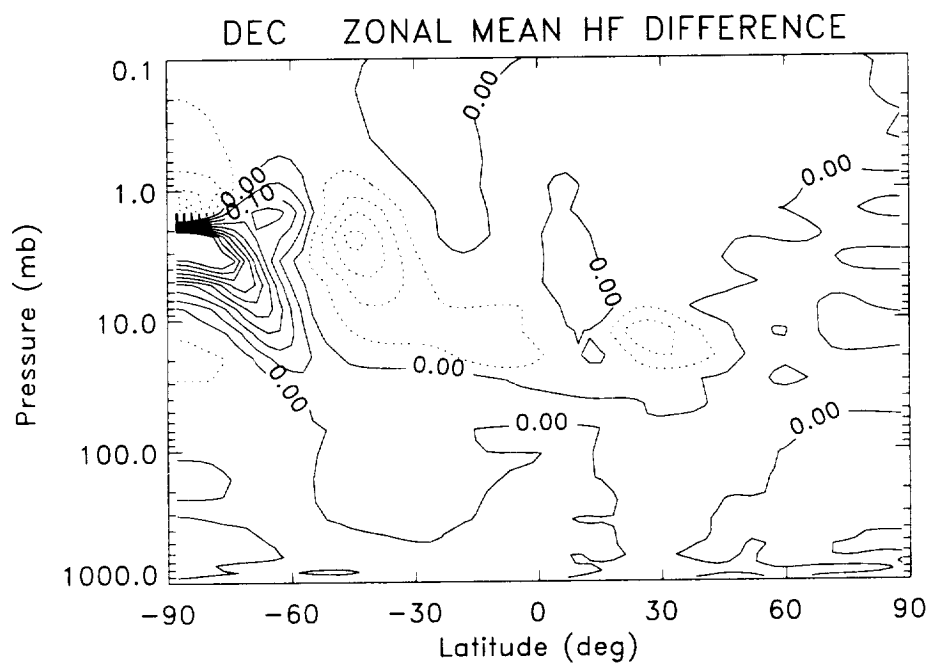


Figure 6.4: December monthly average for the zonal mean hydrogen fluoride difference.

then see changes in the northern hemisphere begin in November or December. As seen in Chapter V, the temperature and wind fields achieved their maximum perturbation in October (Figures 5.3 and 5.8). As a result, hydrogen fluoride did not begin to show a response to the perturbation until October, and not a significant response until December. Figures 6.1 and 6.2 depict the hydrogen fluoride distribution in October for the control case and the difference between the perturbed and control cases. There is a slight decrease in HF near 10 mb at lower and mid latitudes as well as a slight increase at high latitudes, both in the northern and southern hemispheres. Analogous illustrations for December are shown in Figures 6.3 and 6.4. Although not shown, during November the changes in HF were very similar to those in October. By December, however, the modifications to HF are quite obvious. The northern hemisphere perturbation at midlatitudes near 10 mb is weaker than in the southern hemisphere and covers a smaller geographical area. In the southern hemisphere, HF is somewhat depleted in the tropics near 10 mb. At middle and high latitudes there are large increases and decreases in HF between 20 mb and about .7 mb.

In addition to computing the difference between the perturbed and control zonal distributions, the eddy HF flux ($\overline{v'HF'}$) is calculated. This is the changes in HF due to wave activity. Figures 6.5 and 6.6 show the control and difference (perturbed minus control) at various times during December. Only December is shown since the difference between perturbed and control eddy HF flux is minimal until mid to late November. From mid-November until mid-December, most of the changes in HF due to waves occur in the southern hemisphere between 10 and 1 mb. During the second half of December, the northern hemisphere becomes the region of greatest changes in HF due to waves. The shift to the northern hemisphere in December is expected since this is when waves begin to propagate upward in the northern hemisphere.

The November southern hemisphere response is due most likely to the fact that large changes in the wind and temperature fields did not occur until October and later.

Unfortunately, the largest perturbations in HF (poleward of 60°S) in December are not completely understood and therefore should not be used to compare to HALOE HF. It is a result of shortcomings in the model as will be shown. As seen in Figure 6.3 it is evident that some peculiar dynamical processes are occurring at middle and high southern latitudes above 10 mb. These unusual features are not the result of chemical processes since HF is an inert tracer in this simulation. For the most part to the south of the equatorial ridge HF should smoothly increase as seen at high latitudes in Figures 4.1 and 4.8. Occasionally, HALOE has observed a weak enhancement of HF at high southern latitudes in late November (about 65°S at 30 mb in 1996), but not of the magnitude seen in the modeled HF. In 1994 HALOE observed a weak minimum in the same area. Since HALOE does not observe high southern latitudes in December, it is not clear how long the weak enhancement persists or if it strengthens in December as in the model. At any rate, the slight enhancement seen in the HALOE data is much weaker than the maximum apparent in the modeled HF in this region (about 9 mb, poleward of 60°S). The effect of the diabatic heating enhancement is to modify this anomaly by shifting the feature to a lower pressure level. In the control case the maximum is between 8 and 9 mb, while in the perturbed case it is between 6 and 7 mb.

To investigate this aberration, some additional diagnostics are used. Eddy heat flux (heat transport due to waves, $\overline{v'T'}$) is also examined. Figures 6.7 and 6.8 show the eddy heat flux during November and December for the control case. Beginning in mid October and continuing through early December (although very weak in

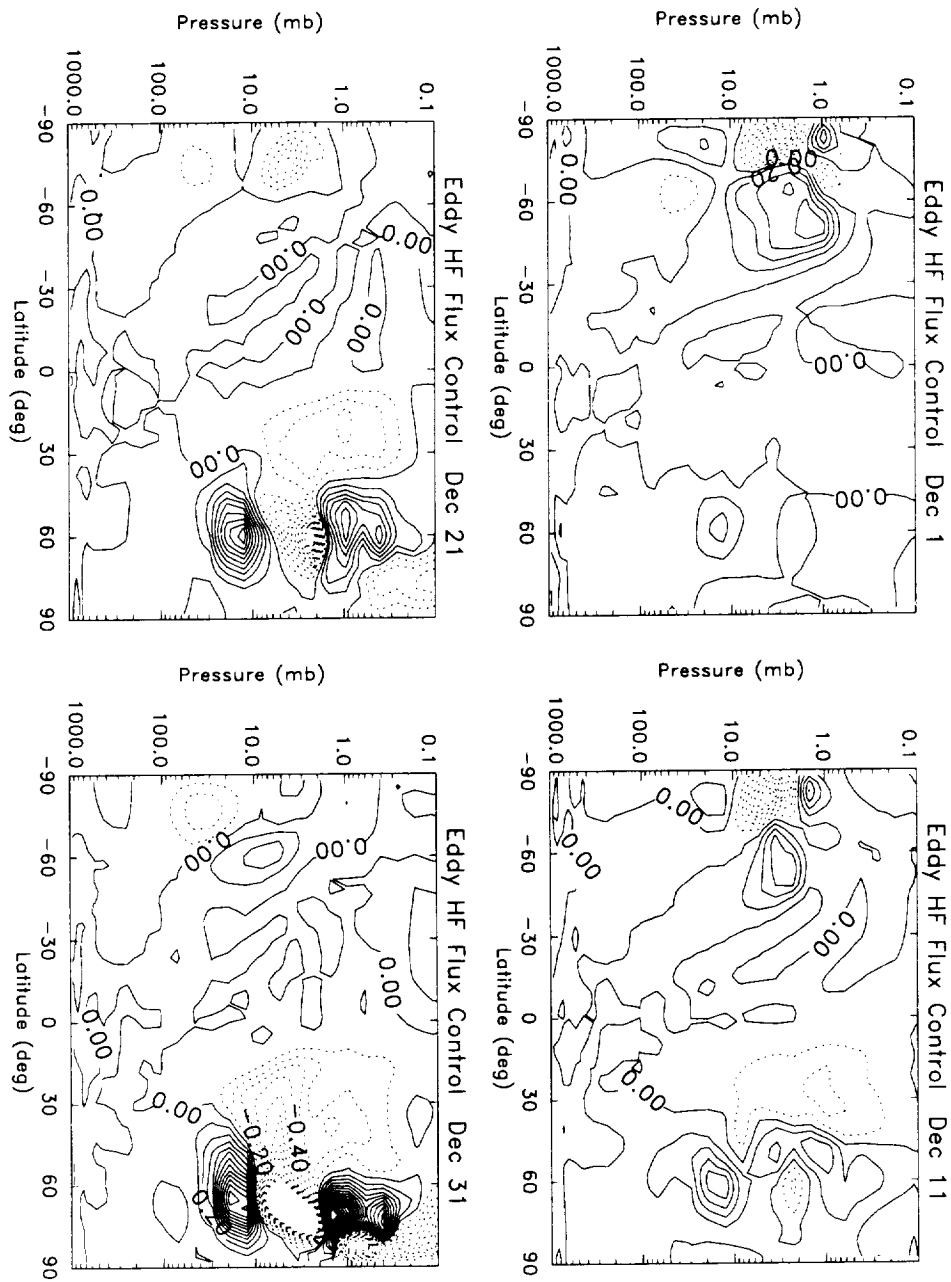


Figure 6.5: Control eddy hydrogen fluoride flux for December 1, 11, 21, and 31.

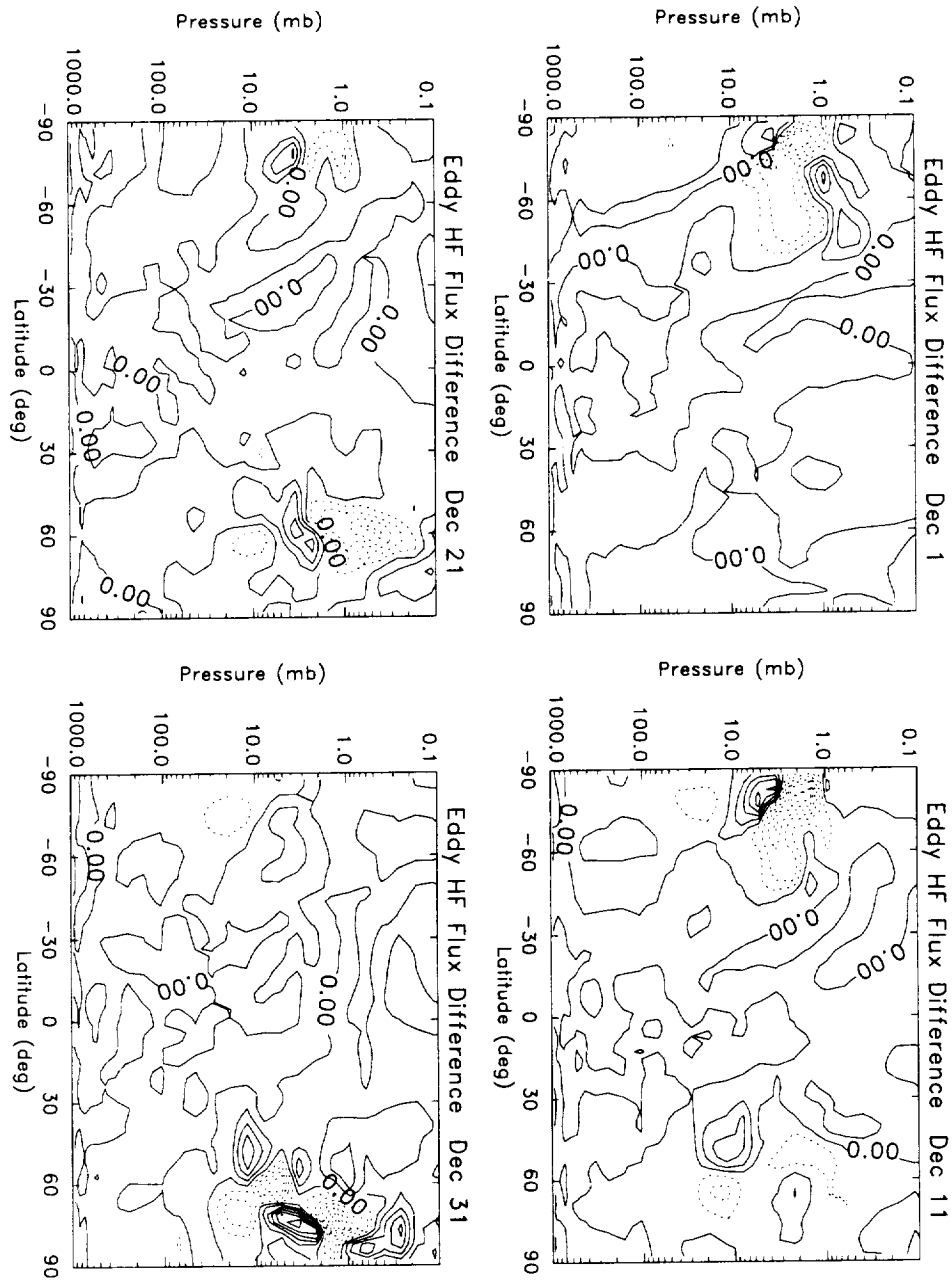


Figure 6.6: Difference (perturbed - control) eddy hydrogen fluoride flux for December 1, 11, 21, and 31.

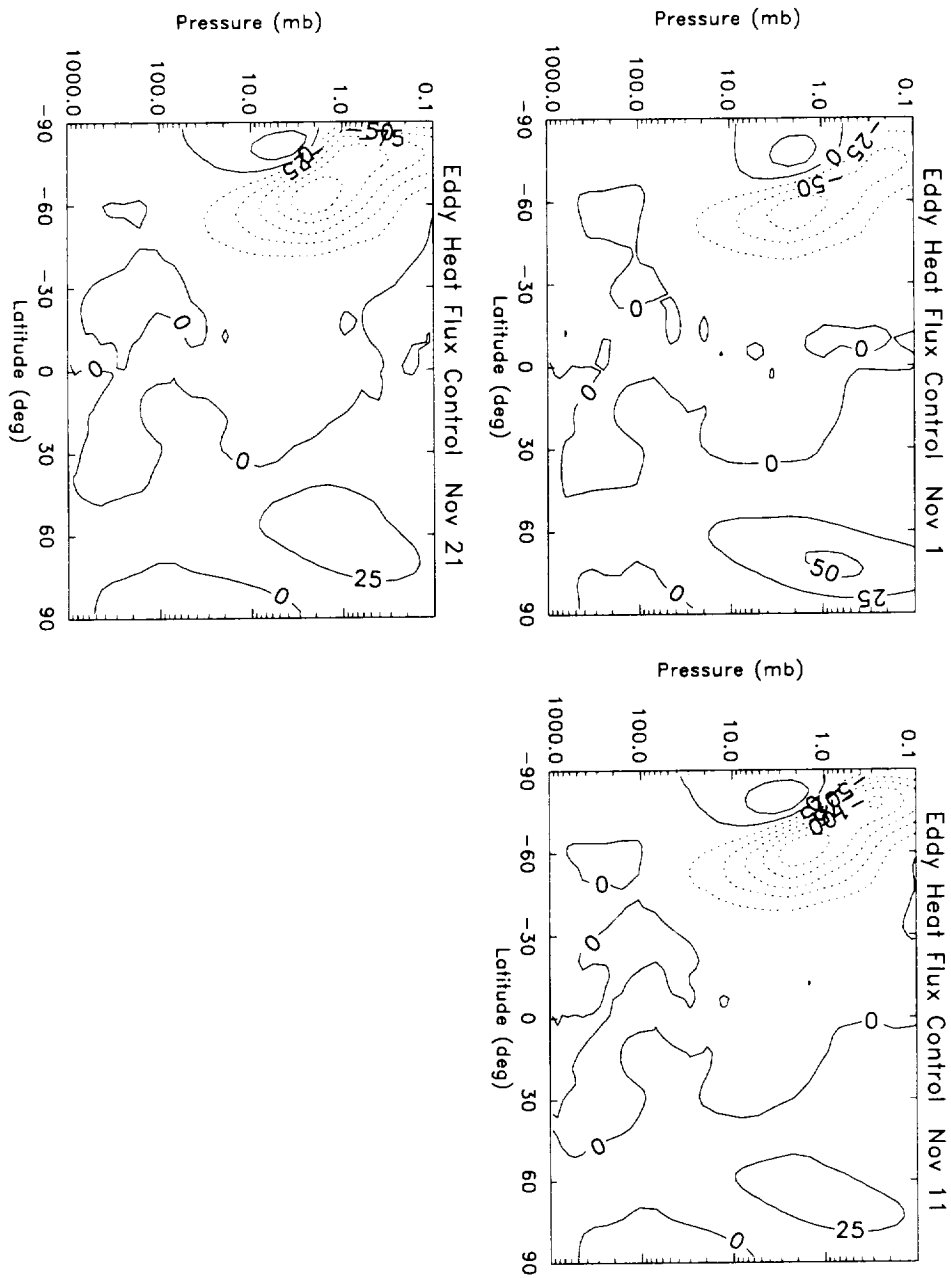


Figure 6.7: Control eddy heat flux for November 1, 11, and 21.

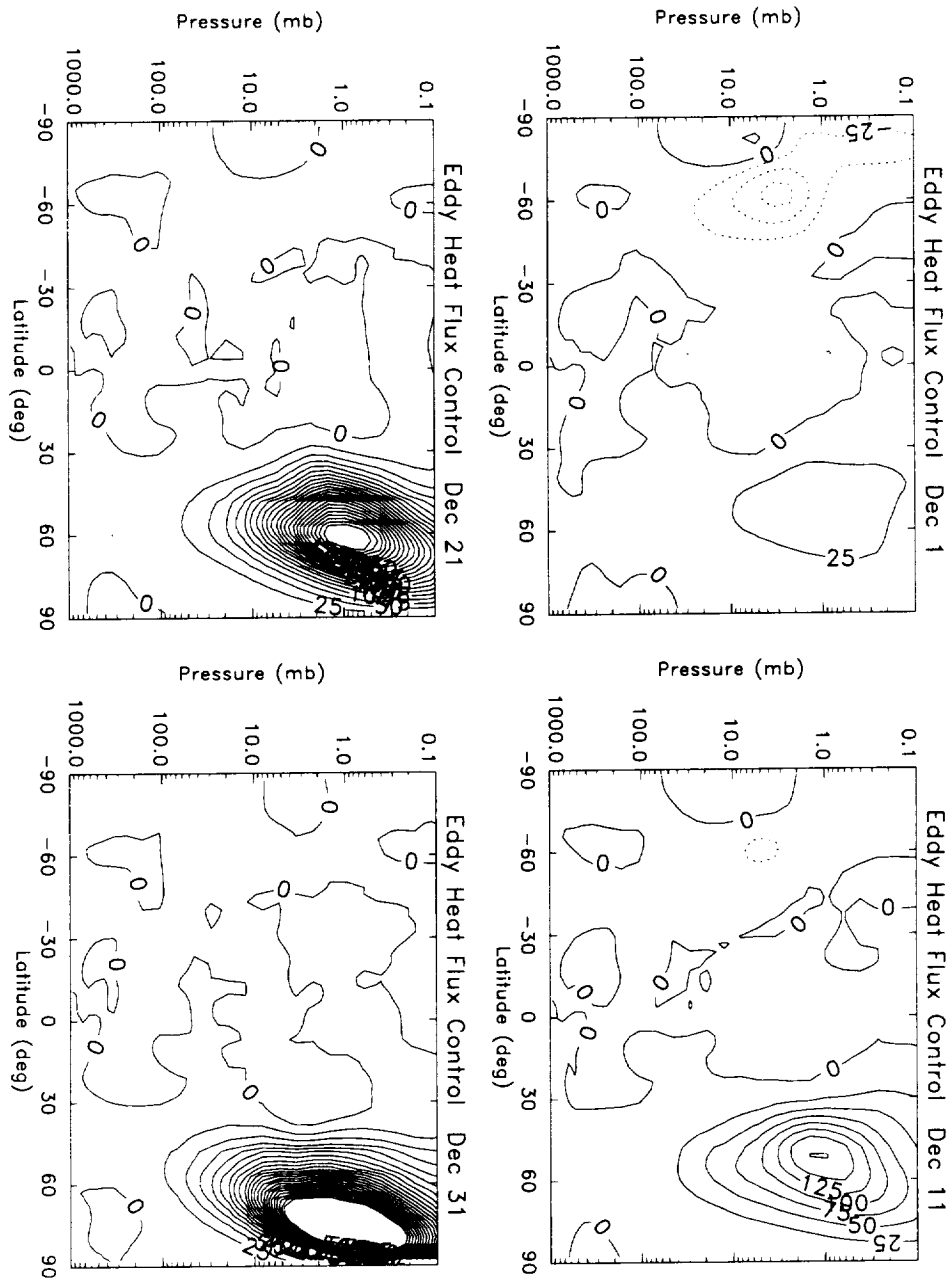


Figure 6.8: Control eddy heat flux for December 1, 11, 21, and 31.

December) at high southern latitudes in the between 10 mb and 1 mb there is a region of positive eddy heat flux. Having this area of positive (northward) eddy heat flux persist for two months is not normal. At that time of year the eddy heat flux should be negative (or southward) south of 60°S as seen in the real atmosphere [79]. The fact that it exists in the same location as the anomalous feature in the control hydrogen fluoride December average (Figure 6.3) suggests some connection between the two. This disturbed region in the control run is also the location of the largest changes in HF due to the perturbation.

What exactly causes these features is not completely understood except that they appear to be the result of wave activity. One possible explanation is that the southern hemisphere final warming is not sufficiently realistic and that its shortcomings permit the anomalous eddy heat flux to exist. The model southern hemisphere final warming depicted in Figure 6.11 occurs during November. Figure 6.11 shows geopotential height at 3.44 mb level. This pressure level is chosen since it is close to the center of the disturbed HF from the control simulation (Figure 6.3). Notice that the low (centered at about 120°E) and the high (centered at 285°E) remain essentially fixed geographically during the warming. There are not any episodic extractions of air from the regions of the low or high being drawn out and mixed as occurs in the real atmosphere. The fact that the low and high do not move or change shape at all during the final warming as would be expected may allow the anomalous eddy heat flux (positive at high southern latitudes, Figure 6.8) to persist for a long period of time. This in turn can impact the hydrogen fluoride distribution in an unrealistic way as was seen in Figure 6.3.

Due to the shortcomings of the HF distribution in the southern hemisphere and the fact that the northern hemisphere response to the perturbation seen in HF is

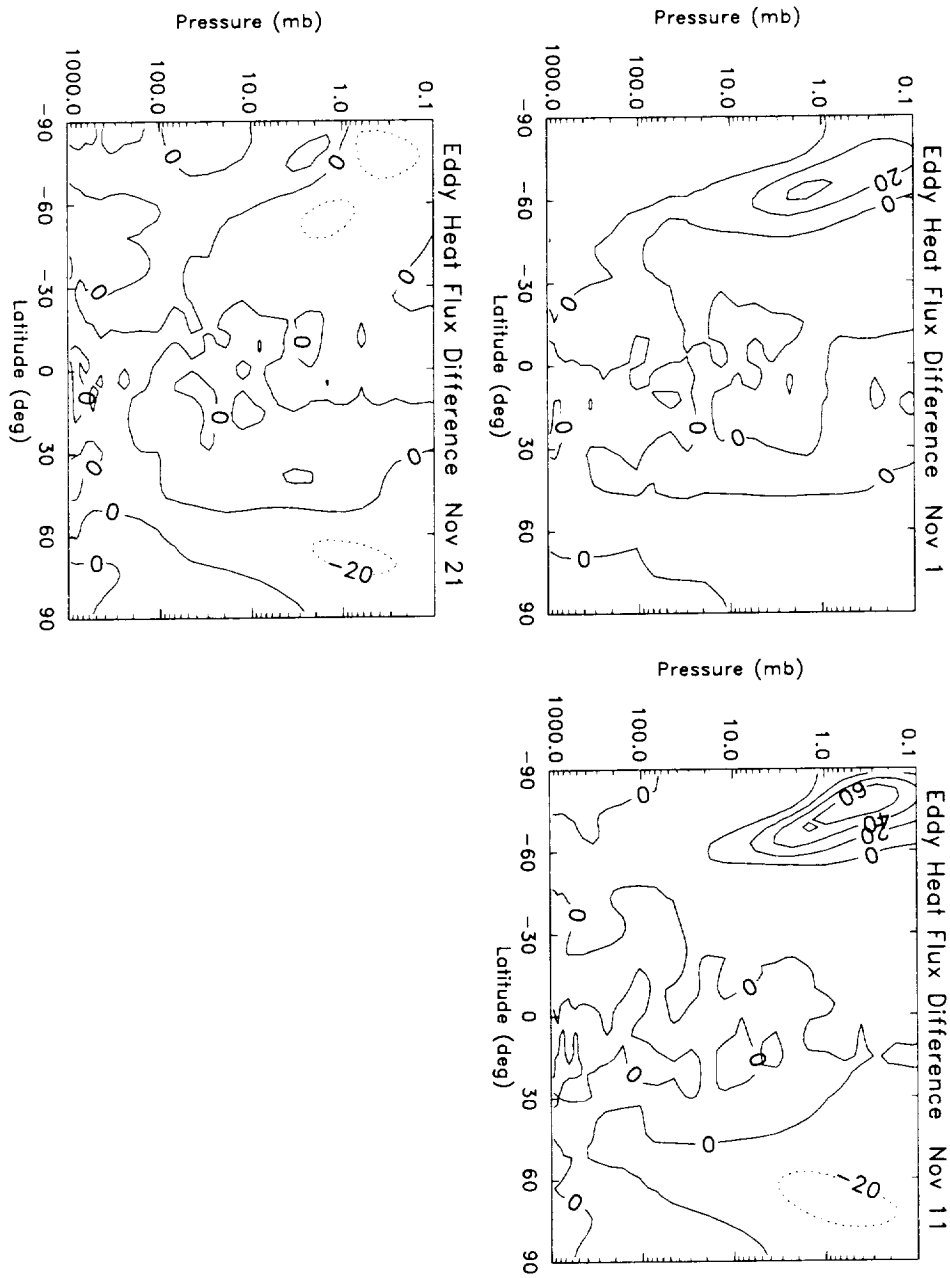


Figure 6.9: Difference (perturbed - control) eddy heat flux for November 1, 11, and 21.

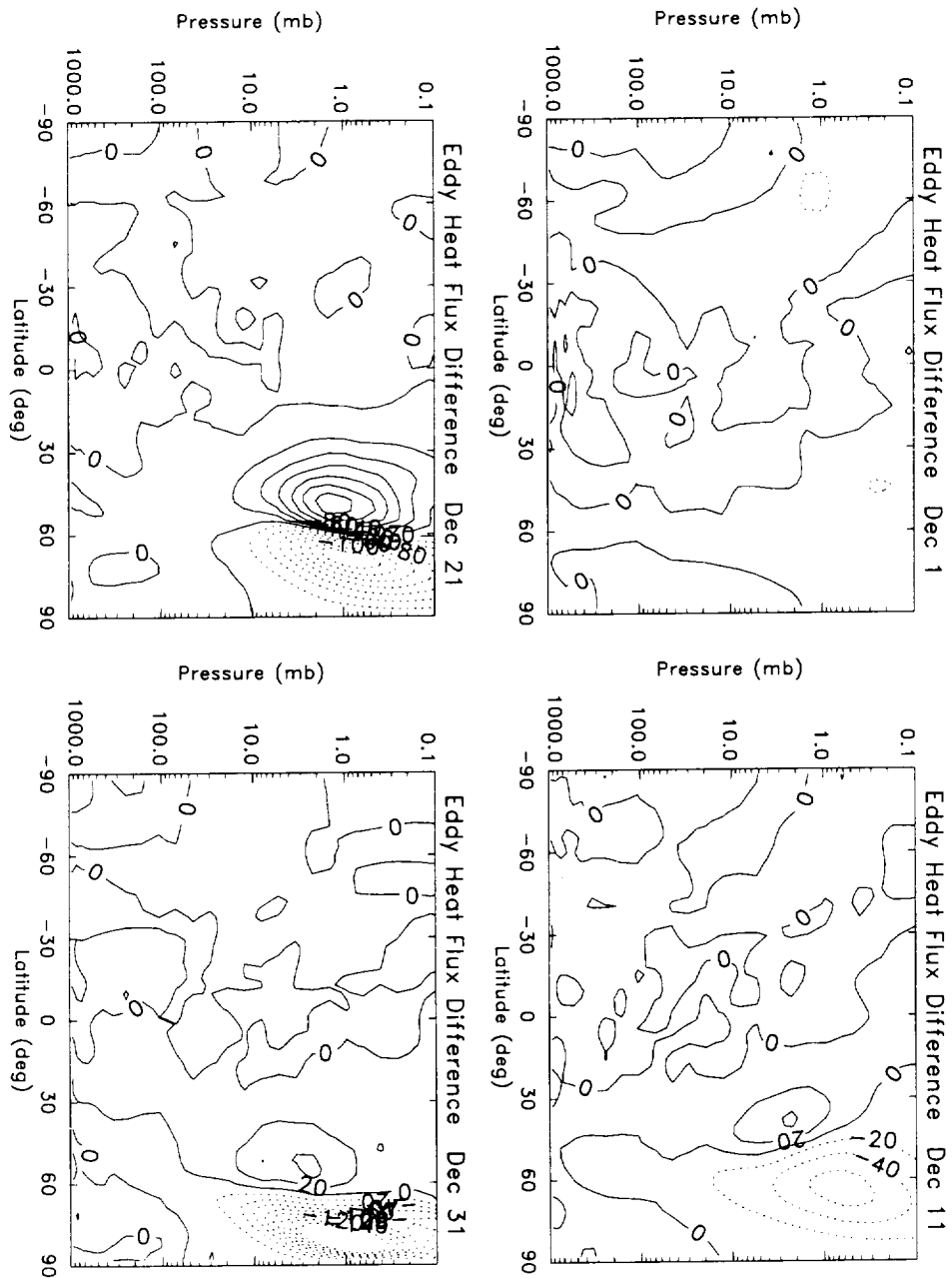


Figure 6.10: Difference (perturbed - control) eddy heat flux for December 1, 11, 21, and 31.

Figure 6.11: Control geopotential height in km ($\times 10^{-2}$) at 3.44 mb. Data is southern hemisphere on November 1 and 15 and December 1 and 15.

weak, it is believed that a meaningful comparison of the modeled HF and the HF measured by HALOE cannot be obtained. If the simulation could have been extended through the northern hemisphere winter, it is possible that a stronger northern hemisphere response could have been obtained.

6.2 Temperature

Several studies have been conducted to assess the degree to which stratospheric temperature was affected by the eruption of Mt. Pinatubo. By analyzing meteorological data from a variety of sources, a number of estimates have been put forth. In the tropics this analysis is complicated by the existence of the quasi-biennial oscillation (QBO). The QBO is an oscillation in the winds between easterly to westerly with a period of every 26 months or so. With these changes in wind direction also come changes in temperatures. During the easterly shear of the QBO (winds changing from west to east) temperatures are colder than average. Conversely, during the westerly shear of the QBO (winds changing from east to west) temperatures are warmer than average, [80]. When Mt. Pinatubo, erupted the winds in the lower stratosphere were changing from westerlies to easterlies, [80], clearly this must be considered in the analysis of the meteorological data. The following is a summary of the different studies that have been conducted which approximate the change in stratospheric temperature due to Mt. Pinatubo.

Probably the most complete study is one by Labitzke [80], however the data is limited in geographic coverage and analysis can only address changes in the northern hemisphere. The temperature data are daily analyses of northern hemisphere pressure levels based predominately on radiosonde data and supplemented by selected satellite derived thicknesses. In most cases the temperature analyses are available

beginning in 1965, but some are available beginning in 1963, [80]. In order to see the true impact of the eruption, Labitzke compared the stratospheric temperature from 1991 to the average temperature during the relevant phase of the QBO from climatology. At 50 mb in October 1991 the winds had just changed from westerly to easterly (easterly sheer, cold phase) so the temperature at 50 mb was compared to the average of the cold phase temperatures from climatology. At 10°N the temperature in October 1991 was nearly 3° warmer than the average of the cold QBO phases [80]. This represents 4.5 standard deviations above the long term mean, [80].

Labitzke also examined the changes in the zonal mean temperature at 20°N . This latitude was chosen because the interannual variability is very small and it is near the latitude of Mt. Pinatubo, [80]. By the end of June, temperatures began to rise and by the end of August temperatures were 3 standard deviations above the mean at both 30 mb and 50 mb, [80]. Temperatures remained 2 to 3 standard deviations above the 26 year mean at 30 mb and 50 mb until December 1991. At these pressure levels largest increases in temperature were in September and October 1991, [80]. It is also interesting to note the trend in temperatures in 1991 differed from the climatological mean. While the climatological mean temperature decreased steadily from June through February at 30 mb, the 1991 zonal mean temperature did not begin to decrease until the end of October, [80]. At 50 mb, the 26 year mean temperature increased slightly from June to July, then decreased through February. The 1991 zonal mean temperatures at 50 mb again did not begin to decrease until early October, [80].

In another study, Angell used a 63 station radiosonde network to analyze the changes in temperature due to the eruption of Mt. Pinatubo, [37]. In order to minimize the effects of the QBO, Angell averaged temperatures over 9 seasons, the

mean period of oscillation of the QBO, [37]. This method does not differentiate between the cold phase of the QBO and the warm phase, rather it averaged them together. In this way, Angell's method does not make as precise a comparison as Labitzke does. In the 100 to 50mb layer, Angell found the greatest heating resulting from Mt. Pinatubo to be at southern mid and high latitudes (up to 2°C), [37]. This warming may have been augmented by the eruption of another volcano (Cerro Hudson, 46°S) in August 1991, [37]. Although the sulfur dioxide emissions were about 10% of the Pinatubo emissions, they were confined to latitudes south of about 40°S . In the tropics, between 100 and 50 mb, the temperature enhancement was between $.5^{\circ}\text{C}$ and 1°C , [37]. In the northern polar latitudes, Angell showed a decrease in temperature of about $.75^{\circ}\text{C}$, [37]. It is likely that the temperature increase at low latitudes is underestimated since the climatology used was not just the cold phase of the QBO, but an average of the cold and warm phases. Examining the variation in temperature changes with respect to height in the tropics, Angell showed that following Pinatubo the maximum heating was at about 20 km, [37], and cooling above 25 km.

Chandra used NMC derived temperatures at 50 mb to assess the impact of the Pinatubo eruption on stratospheric temperatures, [81]. This dataset began in January 1979 and continued through June 1992, one year after Pinatubo erupted. The temperature data was zonally averaged in 10° intervals from 80°S to 80° , [81]. Chandra found that maximum change in temperature to be about 2° in September and October. The temperatures were compared to a 12 year mean, so that the effect of the QBO was not fully accounted for.

With the daily temperatures from the Japan Meteorological Agency (JMA) operational global analysis from the surface to 10 hPa, Kawamata also investigated the

effect of the Pinatubo eruption on stratospheric temperatures, [82]. This dataset provided data from January 1985 to August 1992. Kawamata compared the 1991 temperatures to monthly averages of the climatological data (approximately a 6 year average), [82]. The positive temperature anomaly began in July and reached a maximum in of 2°C increase in October 1991 between 100 and 30 hPa (global mean), [82]. The largest increases in temperature occurred from 30°S to 90°S (about 2.5°C increase), however, the sharpest increase in temperatures occurred equator ward of 30° , [82]. As with the studies conducted by Angell and Chandra, Kawamata did not compare the 1991 temperatures to the mean QBO cold temperature as Labitzke did, most likely because he could not. Their dataset did not cover a long enough time period to include even one oscillation of the QBO.

Randel et al. used data from the Microwave Sounding Unit (MSU) to approximate the temperature enhancement from Mt. Pinatubo between 150 mb and 50 mb, [83]. To minimize the impact of the QBO the 1991 data are compared to a 4 year mean (1987-1990) with the QBO statistically removed, [83]. There was substantial variability at high northern and southern latitudes which was attributed to stratospheric warmings in certain months. At tropical latitudes temperature increases were consistently observed beginning shortly after the eruption. Randel et al. found a 1-1.5 K increase in temperatures between 40°N and S, [83]. The maximum occurred in September and October between 10°S and 30°N , [83].

The temperature response seen in the model is qualitatively consistent with these analyses of meteorological data. Except for Angell who analyzed a 9 season average of temperature and thus was unable to specify a particular month with the maximum temperature change, all other studies found the greatest temperature change to occur in the September/October time frame. The LaRC GCM agrees with this as was

reported in Chapter V and seen in Figure 5.3. There was some disagreement between the various studies as to the geographical location of the greatest temperature change. Chandra does not specify an area and Angell and Kawamata report greatest change at mid to high southern latitudes. Angell indicates this may be due partly to the eruption of Cerro Hudson. Another factor is that neither of these studies accounted for the QBO as rigorously as did Labitzke and Randel. It is possible that because of this, their equatorial heating was under estimated. Labitzke reported maximum temperature change at equatorial and low northern latitudes (she did not have southern hemisphere data) and Randel reported the maximum change to be between 10°S and 30°N . These two studies are in good agreement and both accounted for the QBO in a more rigorous fashion. The temperature change in the LaRC GCM agrees well with this also. The maximum temperature change is in the equatorial region, however it is nearly symmetric with respect to the equator, the northern hemisphere response being only slightly stronger. The magnitude of the temperature change ranged from 1° to 3° . Labitzke reported the greatest temperature change which is not surprising since she had the longest data record and compared the post Pinatubo data to the relevant phase of the QBO from climatology. The model-derived temperature change, although the same sign as the observed temperature change, was significantly greater in magnitude (upwards of 9°C in Figure 5.3). The LaRC GCM does not have a QBO, however this does not account for the large differences in the temperature perturbation. As seen in Labitzke's study, the average cool temperature is -65°C and the average warm temperature is -63°C [80]. Since Pinatubo erupted during the cool phase of the QBO, most likely the temperature difference would be greater if the LaRC GCM did contain an QBO (than compared to an average temperature). It is not know exactly why the model response is so much greater than the response

estimated from observation. It could be related to a number of factors such as: a highly simplified troposphere in the model; no chemistry in the simulation; possibly over estimated heating rates which drove the model perturbation; and the general simplification and parameterization of the stratosphere which is unavoidable when simulating the atmosphere.

A high latitude comparison of the temperature change, although simplified by the absence of the QBO, is complicated by the absence of the feedback from ozone in the model. This version of the LaRC GCM is not coupled to chemistry. As a result the changes in temperature do not impact an ozone distribution which could then feed back into the GCM by altering temperature and thus dynamics also. In addition there is significant variation in the natural atmosphere at polar latitudes in the wintertime due to wave activity. Labitzke and Chandra do not discuss changes at high northern latitudes in December, and Kawamata and Randel have only 6 and 4 years of unperturbed data respectively. As a result a comparison at high northern latitudes was not attempted.

6.3 Ozone

In addition to changes in temperature, the eruption of Mt. Pinatubo also altered stratospheric ozone. Since the hydrogen fluoride tracer in the model cannot be used to infer modeled and observational changes in dynamics, stratospheric ozone is evaluated instead. The changes in ozone are assessed for evidence of changes in circulation related to the Mt. Pinatubo eruption.

Satellite and ground based data have been used to assess the impact of Pinatubo on stratospheric ozone. As with temperature, ozone at equatorial latitudes is influenced by the QBO and this should be addressed for a meaningful comparison to

be made. Numerous studies have been conducted concerning the possible volcanic signal in stratospheric ozone. The following is a summary of studies which evaluated stratospheric ozone following the eruption.

Chandra was one of the first to tackle this question. Using data from the Total Ozone Mapping Spectrometer (TOMS) on the Nimbus-7 satellite and the Solar Backscattered Ultraviolet (SBUV/2) instrument aboard the NOAA-11 satellite Chandra estimated the change in ozone due to Pinatubo [81]. The phase of the QBO was designated based on the 30 mb zonal wind at Singapore (1°N , 103°E). The data sets for the ozone and zonal winds begin January 1979 and run through June 1992. A comparison of the TOMS and SBUV/2 data revealed that the total ozone amounts derived independently are very similar, both in ozone amount and temporal trends [81]. Before accounting for the QBO Chandra reported decreases in total column ozone of 5-6% in the tropics, 3-4% at mid latitudes, and a 6-9% decrease at high latitudes. After accounting for the QBO (the method is not described), the tropical total ozone decrease attributed to Mt. Pinatubo was 2-3% [81]. This smaller decrease is within the range of interannual variability. The 6-9% decrease at high latitudes was 1-2% greater than occurred during the winter of 1990, before Mt. Pinatubo erupted [81]. Although Chandra found decreases in stratospheric ozone following the eruption, the decreases were not outside the interannual variability according to his analysis.

Another study was published at the same time by Schoeberl et al. which also analyzed TOMS data as well as ozonesonde data from Natal, Brazil (6°S , 35°W). The ozonesonde data were taken three months prior to and 2 months after the eruption [84]. Schoeberl et al. grouped latitudes and studied regions between 12°N and 12°S , 12°N and 18°N , and 12°S and 18°S . According to this study the ozone depletion

began about one month after the eruption with a maximum depletion in October 1991 in the equatorial latitudes [84]. There was a weak signal in the 12°S to 18°S band and no signal in the 12°N to 18°N region. In the equatorial region, Schoeberl et al. estimate ozone loss of 10% [84]. Combining this with the ozonesonde data which was verified to be consistent with the TOMS data, Schoeberl et al. found the ozone depletion to be confined to a 2-3 km thick layer between 24 and 28 km [84]. The greatest ozone depletion thus coincided with the upper portion of the aerosol cloud [84]. Schoeberl et al. attributed this ozone loss to enhanced lofting resulting from the heating of the aerosol layer by upwelling infrared radiation [84]. Schoeberl et al. however made no mention of the QBO, and so it is not known how or if this was accounted for.

Another study was conducted by Zerefos et al. which also used the TOMS data. Because this study was published nearly two years later, the TOMS data extended through April 1993 (previous studies had data sets through June 1992). Like Chandra, Zerefos et al. used the 30 mb zonal wind at Singapore to characterize the QBO [85]. Variations in total ozone due to the QBO, El Niño/Southern Oscillation, seasonal changes, the linear trend, and noise are all accounted for in a simple statistical model [85]. All effects except of the noise term are removed from the total ozone yielding a more precise picture of the Pinatubo induced effects. Zerefos et al. found a 2-4% depletion in total column ozone at equatorial latitudes and a 5% ozone loss at middle and high latitudes [85]. The equatorial loss began in August and reached a maximum in October 1991, while the middle and high latitude response did not begin until October 1991. The reasons for these changes are given as enhanced uplift in the tropics and enhanced heterogeneous chemistry at higher latitudes [85].

Randel et al. also investigated ozone changes using TOMS data from Nimbus

7 (January 1987 - April 1993) and Meteor 3 (September 1991 - December 1994) satellites and SBUV/2 (January 1989 - April 1994) data. During the period of overlap for the TOMS data (September 1991 - April 1993) the two instruments showed relatively small differences in geographical locations of ozone change and in the magnitude of ozone change [83]. The satellite data were compared to ground based Dobson spectrophotometer measurements at various latitudes ranging from 75°N to 14°S. A record of satellite data (beginning in 1979) was used to statistically fit and remove variations due to the QBO (approximately 2-4%) with a seasonally varying regression. In addition zonal wind fields between 10 mb and 70 mb were used to characterize the QBO rather than winds at a single pressure level. The changes in ozone are with respect to a pre-Pinatubo ozone average (1987-1990) [83].

The ozone loss that Randel et al. found ranged between 5 and 10% from 1991 through 1994 with large variations in space and time [83]. The maximum ozone depletion at the equator was 4-5% and found to occur in the September/October time frame. At high northern latitudes there was a 6-8% depletion [83]. Randel et al. attribute the equatorial loss to increased upwelling and the northern high latitude loss to heterogeneous reactions on sulfate aerosols [83].

Grant et al. conducted a similar study, but used data from a combination of several sources. Tropical ozone levels were found using data from electrical concentration cell (ECC) sondes both before and after the eruption. The airborne differential absorption lidar (DIAL) system was used for data after the eruption. Data from both of these instruments was compared to ozone the Stratospheric Aerosol and Gas Experiment (SAGE II) ozone climatology. This climatology was derived using data from October 1984 to June 1991. A regression/time series model was used to derive monthly mean ozone levels, [86] and references cited therein. The SAGE II

ozone climatology accounts for variations due to the QBO, annual cycle, and the semiannual oscillation (SAO).

Previously, using ECC sonde data and SAGE II climatology, Grant had shown that post Pinatubo changes in ozone at 25.5 km lay outside the range of normal variability due to the QBO and seasonal changes with greater than 95% confidence [86]. Extending those results Grant et al. later found that in 1991 the greatest ozone loss between 16 and 28 km to be 29 ± 9 DU (Dobson units) or 12% of the total column [86]. August, October, and November had similar results. There was also evidence of an increase in ozone between 28 and 32 km in the tropics (5.9 ± 2.0 DU). Both changes in ozone were well outside the 2σ values from the SAGE II climatology [86]. Grant et al. attributed these changes to a combination of enhanced vertical transport and subsequent lofting of stratospheric air mass and heterogeneous chemistry.

In a later comparison study, Grant revisited this issue and included TOMS data in the analysis [87]. Both the TOMS and SAGE II data showed about the same degree of influence from the QBO, however TOMS data had more seasonal variability [87]. From the TOMS data Grant estimated a loss of about 5% in total column ozone between August and November 1991 from the equator to 10°S . Again analysis of ECC sonde data from Brazzaville and Ascension Island coupled with SAGE II data showed an 8% decrease between 16 and 28 km and a 2% increase between 28 and 32 km during September 1991 [87]. In addition, Grant compared the ECC sonde data directly with the SAGE II data (as opposed to the climatology) and found an average (between Brazzaville and Ascension Island) decrease of 21 ± 9 DU for the September - November 1991 time period (tropical southern latitudes, 16 km to 28 km). In the 28 - 32 km range there was a 2.5 ± 4 DU increase when compared to the easterly phase of the QBO and a 10 ± 4 DU increase when compared to the transition

between the easterly and westerly phase of the QBO [87]. Grant's best estimate for the 28 km to 32 km range was then 6 ± 4 DU. This resulted in a total column ozone decrease of 15 ± 10 DU.

The final and most recent study of the impact of the eruption of Pinatubo on stratospheric ozone was conducted by Angell. Using total ozone data from the ground based Dobson network, Angell was able to address this question with the longest data set yet (1958 to present) [88]. Angell removed the effects of the QBO and the solar cycle. The QBO was accounted for using the epoch method, [88], which involved centering the seasonal total ozone values on the 50 mb Singapore east wind maxima for the 13 QBO cycles between 1958 and 1995 which did not include the eruptions of Agung, El Chichón, and Pinatubo. The 13 total ozone values are then averaged [88]. Solar influences were removed using binomially smoothed total ozone annual deviations and subtracting that from binomially smoothed seasonal deviations. Angell calculated seasonal total ozone changes in several different regions. These included polar, temperate, and tropical climate zones as well as 4 regions in the north temperate region (Russia, Europe, North America, and Asia) [88]. Angell found the largest decreases in total column ozone in the northern polar and temperate regions (about 6%) [88]. In the tropics a weak 1.7% decrease was found. Further investigation of the Northern temperate region by dividing it into 4 regions yielded decreases ranging from 8.5% to 5.5% showing relatively significant longitudinal variation [88]. The maximum ozone depletion in these regions occurred in the winter/spring time period.

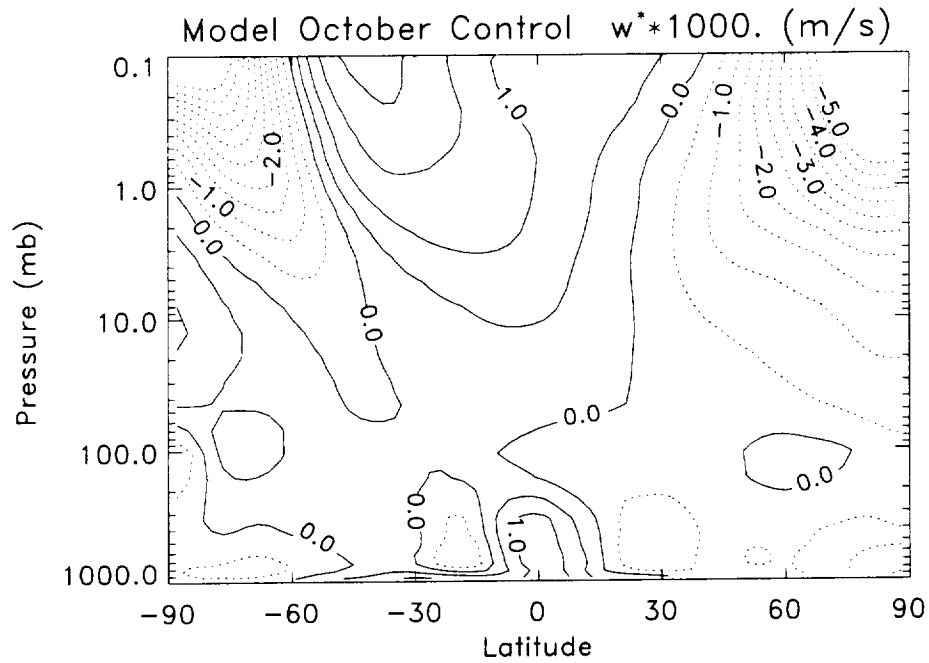


Figure 6.12: October monthly mean of the vertical component of the diabatic circulation for the control case.

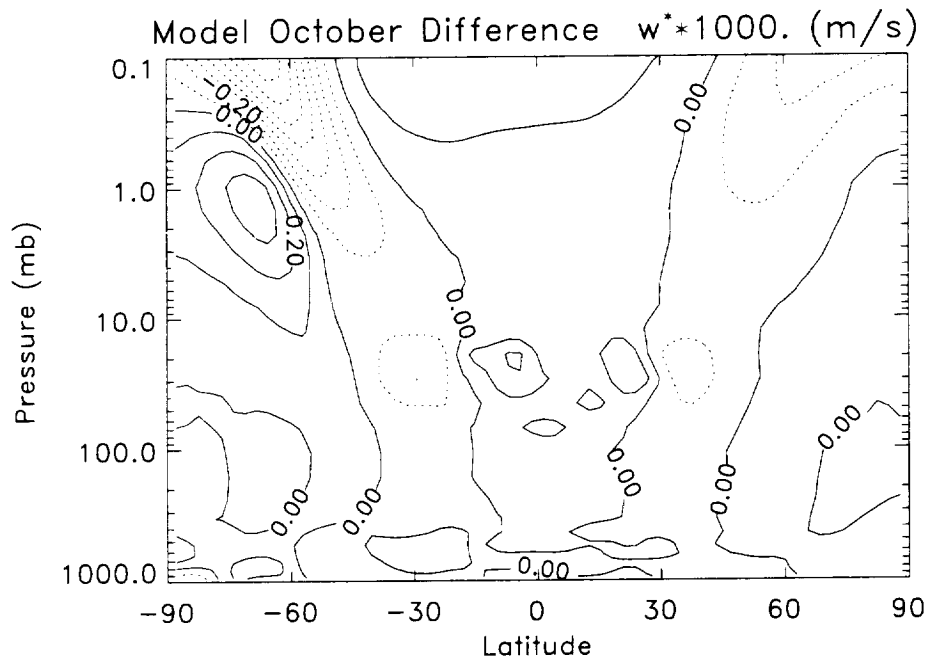


Figure 6.13: Same as Figure 6.12 except for perturbed minus control cases.

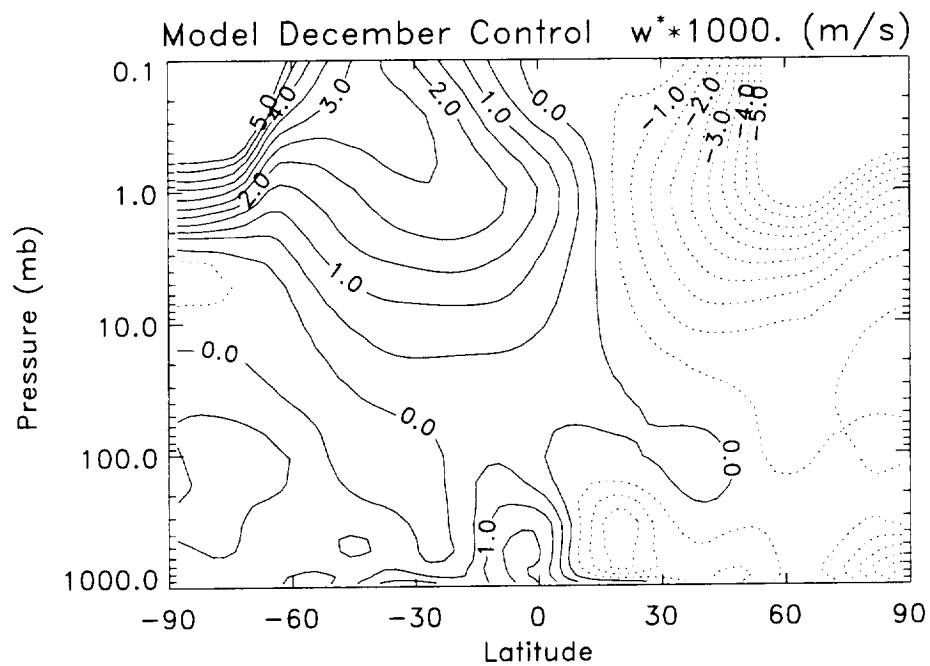


Figure 6.14: Same as Figure 6.12 except for December.

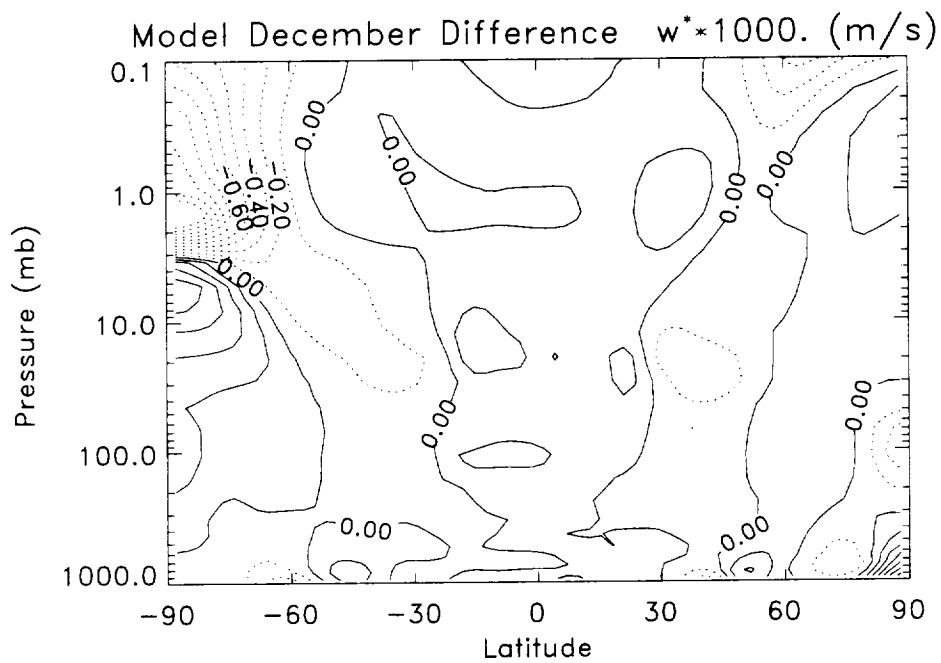


Figure 6.15: Same as Figure 6.13 except for December.

Through a variety of analysis techniques and using various data sets most of these studies concluded that there was a loss of ozone at low latitudes that was attributable to the eruption of Mt. Pinatubo. The reason most often given to explain the loss is enhanced uplift resulting from the infrared heating of the aerosol cloud. To address this hypothesis, the vertical component of the diabatic circulation from the LaRC 3D GCM is examined for evidence of enhanced lofting.

Figures 6.12 through 6.15 show the vertical component of the diabatic circulation for October and December, both the control case and the difference between the perturbed and control cases. These model results show that there is a weak enhancement in lofting for October which is slightly greater in December. The region of increased uplift (15°S - 25°N) is centered slightly north of the equator between 30 mb and 10 mb (approximately 24 km to 32 km). Qualitatively this is in agreement with the location and direction of the circulation perturbation suggested by most of the ozone studies. This is also supported by the weak decreases seen in the model HF at tropical latitudes between 20 and 10 mb (Figures 6.2 and 6.4). Enhanced uplift would decrease equatorial HF levels since HF levels are lower at lower levels in the atmosphere. Whether or not these changes in HF are significant when compared to interannual variability is not known.

6.4 Conclusions

In this chapter it was shown that the hydrogen fluoride distribution was not suitable for comparison to HALOE data in order to deduce changes in the circulation. A comparison of the changes in observed temperature and model calculated changes following the eruption of Mt. Pinatubo showed good qualitative agreement. The geographical location, timing, and sign of the temperature perturbations were con-

sistent. The magnitude of the simulated perturbation however was about 3 times greater than the estimated observed change in temperature. An analysis of changes in ozone and resulting changes in circulation yielded similar results. The geographical location, timing, and sign of the circulation perturbation deduced from observed ozone changes are consistent with changes seen in the vertical component of the diabatic circulation. The enhanced tropical uplift is weak in the model, but no estimation of the magnitude of the increased lofting from ozone observations was made. Therefore, the simulated Pinatubo perturbation is qualitatively consistent with observations. In the following chapter this research is summarized.

CHAPTER VII

SUMMARY

The NASA Langley Research Center (LaRC) three dimensional general circulation model (GCM) was used to investigate the effect of a large volcanic eruption on stratospheric dynamics.

For this study, two modifications were made to the LaRC GCM. First, a hydrogen fluoride inert tracer was initialized in the model. This change involved using the European Center for Medium-range Weather Forecast (ECMWF) meteorological data to calculate isentropic potential vorticity and hydrogen fluoride data from the Halogen Occultation Experiment aboard the Upper Atmosphere Research Satellite. These two quantities were correlated in space and time to derive a function of HF in terms of the potential vorticity. Since model PV is known globally, this relationship could then be used to initialize HF in the GCM within the altitude range of the ECMWF data. Outside the region of ECMWF data a simplified approach is used. Below the lowest ECMWF level model HF is set to .01 ppbv and above the highest ECMWF level the HF distribution is derived from vertical profiles of HALOE HF at various latitudes. Following this initialization the model was run for one year to allow the HF distribution to adjust to model dynamics and to minimize effects of initialization on the study. An ad hoc HF source term was added to counter the

effects of model circulation carrying too much of the HF out of the stratosphere. This HF distribution with the source term included at the time of initialization was then integrated for one year (again to allow for adjustment to model dynamics). The end of this year of adjustment marks the starting point for the control and perturbed simulations.

To simulate the effect of a volcanic eruption an additional heating source was added to the model. The heating source was provided by Ames Research Center and is the result of a modeled dispersion of the Mt. Pinatubo plume. The data is three dimensional and given as heating in units of K/day. This heat source is the additional heating due only to the absorption of infrared radiation by the aerosol cloud. It is updated once per day for the entire six and a half month simulation. The simulation began June 15 (when Mt. Pinatubo erupted) and ended December 31. Originally a one year simulation was planned, however it was not possible to obtain heating perturbation data from Ames for the second six months due to inadequacies in the Ames microphysical/transport model. The microphysical/transport model was not configured to produce realistic aerosol distributions beyond the end of December.

An evaluation of the modeled control hydrogen fluoride distribution illustrated some strengths and weaknesses in the distribution. The modeled HF distribution was compared to zonal HALOE data from January and July 1994 (an approximately 'clean' stratosphere, free from Pinatubo aerosol). For the most part, HALOE and modeled HF exhibited the same basic features. There is a ridge over the equator, with decreasing values to the north and south. There is a notable exception in the southern hemisphere in January when modeled HF has a maximum at high southern latitudes which is not seen in the HALOE data. A comparison of vertical profiles at selected latitudes from the model and HALOE (1993, 1994, and 1995) was conducted

to account for some of the natural annual variability in HF. In these comparisons the strengths and weaknesses were further illustrated. At middle and low latitudes the modeled HF and HALOE HF exhibited the same general shape. At equatorial latitudes model HF is consistently lower than HALOE HF due to greater uplift in the model. At middle latitudes the agreement quite good. There are differences at high latitudes as seen in the zonal July and January comparisons. The high latitude differences have been attributed to differences in wave activity.

An evaluation of the control and perturbed model simulations show that there are significant differences between the two simulations due to the enhanced heating. The model quantities which were investigated were temperature, zonal wind, and geopotential height. These parameters were analyzed in terms of the zonal mean distribution, model climatological variance, temporal evolution, and wave variance. Temperature showed a maximum increase (of about 9 K) in October in the equatorial region. Temperature decreases at higher latitudes in the northern and southern hemispheres continued to deepen through December. The model climatological variance showed these perturbations to be significantly greater than could be expected from annual variability. The temporal evolution of the temperature illustrated the gradual deepening of the positive temperature perturbation in the equatorial region and the development of a negative perturbation at higher latitudes. Also depicted was a hemispheric asymmetry with greater temperature increases in the northern hemisphere. Finally by looking at the wave variance it was shown that the effect of the heating perturbation was to decrease the wave activity.

Analysis of the zonal wind yielded similar results. The largest perturbations to the zonal wind occurred in October, although the perturbations in December were still quite large. In general the heating enhancement resulted in a strengthening

of the zonal mean circulation. In October the southern hemisphere westerlies were strengthened and the center of the jet was shifted northward. In the northern hemisphere the westerlies were also strengthened, however not by as much. In December, the southern hemisphere easterlies were weakened, while the northern hemisphere westerlies strengthened. Again an analysis of the model climatology revealed these perturbations to the zonal wind to be significantly greater than could be expected from climatology. The temporal evolution of the zonal wind also reinforced the previous result showing the largest changes to the zonal wind to be at middle to upper latitudes. As with temperature, the perturbation decreased the wave activity present in the zonal wind.

The geopotential height showed sensitivity to the heating enhancement as well. The zonal mean perturbation to the geopotential height illustrated an enhanced geopotential height at mid to low latitudes and a negative response at high latitudes. The positive perturbation is centered slightly north of the equator. The negative response in the northern hemisphere is weaker than the perturbation in the southern hemisphere. The model climatology showed some degree of variance at middle and low latitudes and at high southern latitudes. The changes initiated by the heating enhancement however were well outside the climatological variance especially from southern mid latitudes to the north pole. The temporal evolution again showed the positive anomaly favoring the northern hemisphere and the greatest negative changes to be at high southern latitudes. Unlike the temperature and zonal wind which had maximum changes in October, the geopotential height perturbation was still growing when the simulation ended in December. As with temperature and zonal wind, the geopotential height wave variance decreased as a result of the heating enhancement.

Evaluating these results against available observational data yielded positive re-

sults. The comparison of model temperature changes with several analyses of temperature data showed good qualitative agreement. The timing of the maximum change (September/October), the geographical location of the maximum (equatorial region), and the sign of the change (positive, indicating a temperature increase) were in agreement with most of the analyses. The magnitude of the change however, was much greater in the model than calculated from meteorological data. Some analyses differed in their conclusions. This is to be expected when datasets of varying length are used, analysis techniques differ, and equatorial data is influenced by the quasi-biennial oscillation.

The plan to analyze changes in circulation using the HF perturbations from model simulations and comparing these to changes in HALOE HF data was not achieved. This was due partly to an anomalous feature discovered in the model control HF distribution which was enhanced by the perturbation. The anomalous feature dominated the HF difference (perturbed minus control). In addition, other changes in the HF data proved to be considerably weaker than expected. Since the changes in HF were either unrealistic or too weak to compare to HALOE HF, this analysis was not completed. As a result ozone was used to try to infer dynamical changes. In general the studies concerned with changes in ozone due to Mt. Pinatubo concluded that there were decreases in the equatorial region which were postulated be the result of enhanced lofting. Enhanced lofting occurred as a result of heating of the aerosol cloud at equatorial latitudes. An analysis of the vertical component of the model diabatic circulation showed that there was an area of weak enhancement in uplift in the model at approximately the expected location and at the proper time. Model HF also shows some evidence of enhanced uplift in the equatorial region (although very weak).

This dissertation study illustrated some of the strengths and weaknesses of an older version of the Langley 3-D general circulation model. It has reasonable success in modeling a climatology similar to the real atmosphere however some features are not well represented. The southern hemisphere final warming is the most visible example encountered here. The experiment of adding an HF tracer and diabatic heating enhancement to simulate the effects of the eruption of Mt. Pinatubo proved to yield interesting results. Although the hydrogen fluoride portion of the experiment did not work out as planned the addition of a heating rate did. The heating perturbation resulted in significant changes in model parameters (temperature, zonal wind, and geopotential height). The changes in temperature and weak changes in equatorial ascent were also concluded to be present in observed data. These changes in model data and observed data agreed reasonably well in space, time, and sign of perturbation. An exact match was not expected since there are some obvious limitations in the modeling study and also in several of the analyses techniques of observed quantities. Two sources of model error are possible. One is errors in the heating rates obtained from Ames. Not all microphysical properties are completely understood or can be exactly represented by a model. In addition the LaRC 3-D GCM does not simulate a specific year. The winds and temperature were not initialized to simulate the months following the eruption of Mt. Pinatubo. Instead the model produces a generic simulation of the atmosphere and the model data are consistent with a climatology of the actual atmosphere. The analyses of observational data were limited by the temporal extent of the datasets and the geographical coverage. In spite of these limitations, this experiment still provided useful results.

APPENDICES

APPENDIX A**Hydrogen Flouride Sources and Sinks**

Pressure (mb)	Source
.0022	1.91×10^{-4}
.0056	2.07×10^{-4}
.0085	2.04×10^{-4}
.0131	2.12×10^{-4}
.0201	2.12×10^{-4}
.0309	2.37×10^{-4}
.0474	2.34×10^{-4}
.0728	2.22×10^{-4}
.1117	1.95×10^{-4}
.1715	1.63×10^{-4}
.2632	1.53×10^{-4}
.4041	1.62×10^{-4}
.6202	1.99×10^{-4}
.9521	2.44×10^{-4}
1.462	2.88×10^{-4}
2.244	3.17×10^{-4}

Pressure (mb)	Source
3.444	2.89×10^{-4}
5.287	2.70×10^{-4}
8.116	2.04×10^{-4}
12.46	1.11×10^{-4}
19.12	3.41×10^{-5}
29.36	1.52×10^{-5}
45.06	-7.47×10^{-6}
69.18	-1.42×10^{-5}
106.2	-9.77×10^{-6}
163.0	-9.78×10^{-6}
242.7	-8.54×10^{-6}
336.7	-3.76×10^{-6}
435.4	-2.35×10^{-6}
535.4	-1.39×10^{-6}
635.4	-1.41×10^{-6}
735.4	-1.15×10^{-6}
835.4	-1.15×10^{-6}
942.7	-8.49×10^{-7}

BIBLIOGRAPHY

BIBLIOGRAPHY

- [1] D. L. Albritton, R. T. Watson, and P. J. Aucamp, "Scientific Assessment of Ozone Depletion: 1994," tech. rep., World Meteorological Organization, February 1995. Global Ozone Research and Monitoring Project, Report No. 37.
- [2] D. J. Hofmann, "Perturbations to the global atmosphere associated with the El Chichón volcanic eruption of 1982," *Reviews of Geophysics*, vol. 25, pp. 743–759, May 1987.
- [3] G. Brasseur and S. Solomon, *Aeronomy of the Middle Atmosphere*. Dordrecht, Holland: D. Reidel and Co., second ed., 1986.
- [4] R. Monastersky, "Pinatubo's impact spreads around the globe," *Science News*, vol. 140, pp. 132–133, August 1991.
- [5] G. Brasseur and C. Granier, "Mount Pinatubo aerosols, chlorofluorocarbons, and ozone depletion," *Science*, vol. 257, pp. 1,239–1,242, August 1992.
- [6] P. V. Johnston, R. L. McKenzie, J. G. Keys, and W. A. Matthews, "Observations of depleted stratospheric NO₂ following the Pinatubo volcanic eruption," *Geophysical Research Letters*, vol. 19, pp. 211–213, January 1992.
- [7] D. J. Hofmann and S. Solomon, "Ozone destruction through heterogeneous chemistry following the eruption of El Chichón," *Journal of Geophysical Research*, vol. 94, pp. 5,029–5,041, April 1989.
- [8] J. M. Rodriguez, M. K. W. Ko, and N. D. Sze, "Role of heterogeneous conversion of N₂O₅ on sulphate aerosols in global ozone losses," *Nature*, vol. 352, pp. 134–137, July 1991.
- [9] S. Solomon, "Progress toward a quantitative understanding of Antarctic ozone depletion," *Nature*, vol. 347, pp. 347–354, September 1990.
- [10] S. Solomon, R. W. Sanders, R. O. Jakoubek, K. H. Arpag, S. L. Stephens, J. G. Keys, and R. R. Garcia, "Visible and near-ultraviolet spectroscopy at McMurdo Station, Antarctica 10. Reductions of stratospheric NO₂ due to Pinatubo aerosols," *Journal of Geophysical Research*, vol. 99, pp. 3,509–3,516, February 1994.

- [11] H. Jäger and K. Wege, "Stratospheric ozone depletion at northern midlatitudes after major volcanic eruptions," *Journal of Atmospheric Chemistry*, vol. 10, pp. 273–287, 1990.
- [12] G. P. Brasseur, C. Granier, and S. Walters, "Future changes in stratospheric ozone and the role of heterogeneous chemistry," *Nature*, vol. 348, pp. 626–628, December 1990.
- [13] S. Kinne, O. B. Toon, and M. J. Prather, "Buffering of stratospheric circulation by changing amounts of tropical ozone: A Pinatubo case study," *Geophysical Research Letters*, vol. 19, pp. 1,927–1,930, October 1992.
- [14] G. Pitari, "A numerical study of the possible perturbation of stratospheric dynamics due to Pinatubo aerosols: Implications for tracer transport," *Journal of the Atmospheric Sciences*, vol. 50, pp. 2,443–2,461, August 1993.
- [15] G. Pitari and V. Rizi, "An estimate of the chemical and radiative perturbation of stratospheric ozone following the eruption of Mt. Pinatubo," *Journal of the Atmospheric Sciences*, vol. 50, pp. 3,260–3,276, August 1993.
- [16] M. Verdecchia, G. Visconti, and G. Pitari, "Radiative perturbation due to the eruption of El Chichón: Effects on ozone," *Journal of Atmospheric and Terrestrial Physics*, vol. 54, no. 7/8, pp. 1,081–1,084, 1992.
- [17] D. J. Hofmann, S. J. Oltmans, J. M. Harris, S. Solomon, T. Deshler, and B. J. Johnson, "Observation and possible causes of new ozone depletion in Antarctica in 1991," *Nature*, vol. 359, pp. 283–287, September 1992.
- [18] T. J. Dunkerton and D. P. Delisi, "Anomalous temperature and zonal wind in the tropical upper stratosphere, 1982/1983," *Journal of Geophysical Research*, vol. 96, pp. 22,631–22,641, December 1991.
- [19] NASA, "UARS (Upper Atmosphere Research Satellite): A program to study global ozone change." Technical Report, 1991.
- [20] A. Lambert, R. G. Grainger, J. J. Remedo, C. D. Rodgers, M. Corney, and F. W. Taylor, "Measurements of the evolution of the Mt. Pinatubo aerosol cloud by ISAMS," *Geophysical Research Letters*, vol. 20, pp. 1,287–1,290, June 1993.
- [21] M. P. McCormick and R. E. Veiga, "SAGE II measurements of early Pinatubo aerosols," *Geophysical Research Letters*, vol. 19, pp. 155–158, January 1992.
- [22] J. M. Russell III, A. F. Tuck, L. L. Gordley, J. H. Park, S. R. Drayson, J. E. Harries, R. J. Cicerone, and P. J. Crutzen, "HALOE Antarctic observations in the spring of 1991," *Geophysical Research Letters*, vol. 20, pp. 719–722, April 1993.

- [23] J. M. Russell III, L. L. Gordley, J. H. Park, S. R. Drayson, W. D. Hesketh, R. J. Cicerone, A. F. Tuck, J. E. Frederick, J. E. Harries, and P. J. Crutzen, "The Halogen Occultation Experiment," *Journal of Geophysical Research*, vol. 97, January 1992.
- [24] R. E. Young, H. Houben, and O. B. Toon, "Radiatively forced dispersion of the Mt. Pinatubo volcanic cloud and induced temperature perturbation in the stratosphere during the first few months following the eruption," *Geophysical Research Letters*, vol. 21, pp. 369–372, March 1994.
- [25] K. Labitzke and M. P. McCormick, "Stratospheric temperature increases due to Pinatubo aerosols," *Geophysical Research Letters*, vol. 19, pp. 207–210, January 1992.
- [26] D. M. Winker and M. T. Osborn, "Airborne lidar observations of the Pinatubo volcanic plume," *Geophysical Research Letters*, vol. 19, pp. 167–170, January 1992.
- [27] A. F. D'Altorio, F. Masci, G. Visconti, V. Rizi, and E. Boschi, "Simultaneous stratospheric aerosol and ozone lidar measurements after the Pinatubo volcanic eruption," *Geophysical Research Letters*, vol. 19, pp. 393–396, 1992.
- [28] L. L. Stowe, R. M. Carey, and P. P. Pellegrino, "Monitoring the Mt. Pinatubo aerosol layer with NOAA/11 AVHRR data," *Geophysical Research Letters*, vol. 19, pp. 159–162, January 1992.
- [29] T. E. DeFoor, E. Robinson, and S. Ryan, "Early observations of the June 1991 Pinatubo eruption plume at Mauna Loa Observatory, Hawaii," *Geophysical Research Letters*, vol. 19, pp. 187–190, 1992.
- [30] D. E. Kinnison, K. E. Grant, P. S. Connell, D. A. Rotman, and D. J. Wuebbles, "The chemical and radiative effects of the Mount Pinatubo eruption," *Journal of Geophysical Research*, vol. 99, pp. 25,705–25,731, December 1994.
- [31] X. Tie, G. Brasseur, B. Briegleb, and C. Granier, "Two-dimensional simulation of Pinatubo aerosol and its effect on stratospheric ozone," *Journal of Geophysical Research*, vol. 99, pp. 20,545–20,562, October 1994.
- [32] G. Brasseur, M. H. Hitchman, S. Walters, M. Dymek, E. Falise, and M. Pirre, "An interactive chemical dynamical radiative two-dimensional model of the middle atmosphere," *Journal of Geophysical Research*, vol. 95, pp. 5,639–5,655, April 1990.
- [33] J. E. Rosenfield, D. B. Considine, P. E. Meade, J. T. Bacmeister, C. H. Jackman, and M. R. Schoeberl, "Stratospheric effects of Mount Pinatubo aerosol studied with a coupled two-dimensional model," *Journal of Geophysical Research*, vol. 102, pp. 3,649–3,670, February 1997.

- [34] A. R. Douglass, C. H. Jackman, and R. D. Stolarski, "Comparison of model results transporting the odd nitrogen family with results transporting separate odd nitrogen species," *Journal of Geophysical Research*, vol. 94, pp. 9,862–9,872, July 1989.
- [35] J. T. Bacmeister, M. R. Schoeberl, M. E. Summers, J. E. Rosenfield, and X. Zhu, "Descent of long-lived trace gases in the winter polar vortex," *Journal of Geophysical Research*, vol. 100, pp. 11,669–11,684, June 1995.
- [36] M. H. Hitchman, M. McKay, and C. R. Trepte, "A climatology of stratospheric aerosol," *Journal of Geophysical Research*, vol. 99, pp. 20,689–20,700, October 1994.
- [37] J. K. Angell, "Comparison of stratospheric warming following the Agung, El Chichón, and Pinatubo eruptions," *Geophysical Research Letters*, vol. 20, pp. 715–718, April 1993.
- [38] D. Rind, N. K. Balachandran, and R. Suozzo, "Climate change and the middle atmosphere. Part II: The impact of volcanic aerosols," *Journal of Climate*, vol. 5, pp. 189–208, March 1992.
- [39] G. Pitari, M. Verdecchia, and G. Visconti, "A transformed Eulerian model to study possible effects of the El Chichón eruption on the stratospheric circulation," *Journal of Geophysical Research*, vol. 92, pp. 10,961–10,975, 1987.
- [40] J. B. Pollack and T. P. Ackerman, "Possible effects of the El Chichón volcanic cloud on the radiation budget of the northern tropics," *Geophysical Research Letters*, vol. 10, pp. 1,057–1,060, November 1983.
- [41] B. J. Hoskins and A. J. Simmons, "A multi-layer spectral model and the semi-implicit method," *Quarterly Journal of the Royal Meteorological Society*, vol. 101, pp. 637–655, 1975.
- [42] W. L. Grose, J. E. Nealy, R. E. Turner, and W. T. Blackshear, "Modeling the transport of chemically active constituents in the stratosphere," in *Transport Processes in the Middle Atmosphere* (G. Visconti and R. Garcia, eds.), (Dordrecht), pp. 229–250, D. Reidel and Co., 1987.
- [43] W. T. Blackshear, W. L. Grose, and R. E. Turner, "Simulated sudden stratospheric warming: Synoptic evolution," *Quarterly Journal of the Royal Meteorological Society*, vol. 113, pp. 815–846, 1987.
- [44] R. B. Pierce, W. T. Blackshear, T. D. Fairlie, W. L. Grose, and R. E. Turner, "The interaction of radiative and dynamical processes during a simulated sudden stratospheric warming," *Journal of the Atmospheric Sciences*, vol. 50, pp. 3,829–3,851, December 1993.

- [45] W. L. Gates and A. B. Nelson, "A new (revised) tabulation of the Scripps topography on a one degree global grid. Part I. Terrain heights," Tech. Rep. R-1276-1-ARPH, The Rand Corporation, Santa Monica, CA, 1975.
- [46] K. Puri and W. Bourke, "Implications of horizontal resolution in spectral model integrations," *Monthly Weather Review*, vol. 102, pp. 333–347, May 1974.
- [47] W. Bourke, "A multi-level spectral model. I. Formulation and hemispheric integrations," *Monthly Weather Review*, vol. 102, pp. 687–701, October 1974.
- [48] H. M. Helfand, "The effect of cumulus friction on the simulation of the January Hadley circulation by the GLAS model of the general circulation," *Journal of the Atmospheric Sciences*, vol. 36, pp. 1,827–1,843, October 1979.
- [49] J. R. Holton and D. E. Colton, "A diagnostic study of the vorticity balance at 200 mb in the tropics during the northern summer," *Journal of the Atmospheric Sciences*, vol. 29, pp. 1,124–1,128, September 1972.
- [50] S. L. Thompson and D. L. Hartmann, "'Cumulus friction': Estimated influence on the tropical mean meridional circulation," *Journal of the Atmospheric Sciences*, vol. 36, pp. 2,022–2,026, October 1979.
- [51] G. A. Corby, A. Gilchrist, and R. L. Newson, "A general circulation model of the atmosphere suitable for long period integrations," *Quarterly Journal of the Royal Meteorological Society*, vol. 98, pp. 809–832, 1972.
- [52] W. M. Washington, ed., *Documentation for the Community Climate Model (CCM)*, ch. III. Boulder, CO: National Center for Atmospheric Research, January 1982. Version 0.
- [53] D. L. Williamson, J. T. Kiehl, V. Ramanathan, R. E. Dickinson, and J. J. Hack, "Description of NCAR Community Climate Model (CCM1)," Tech. Rep. TN-285+STR, National Center for Atmospheric Research, Boulder, CO, June 1987.
- [54] J. R. Holton, "The role of gravity wave induced drag and diffusion in the momentum budget of the mesosphere," *Journal of the Atmospheric Sciences*, vol. 39, pp. 791–799, April 1982.
- [55] J. R. Holton, *The Dynamic Meteorology of the Stratosphere and Mesosphere*, vol. 15 of *Meteorological Monographs*. Boston, MA: American Meteorological Society, 1975.
- [56] J. R. Holton and W. M. Wehrbein, "A numerical model of the zonal mean circulation of the middle atmosphere," *Pure and Applied Geophysics*, vol. 118, pp. 284–306, 1980.

- [57] B. A. Boville, "Wave-mean flow interactions in a general circulation model of the troposphere and stratosphere," *Journal of the Atmospheric Sciences*, vol. 43, pp. 1,711–1,725, August 1986.
- [58] K. P. Shine, "The middle atmosphere in the absence of dynamical heat fluxes," *Quarterly Journal of the Royal Meteorological Society*, vol. 113, pp. 603–633, 1987.
- [59] K. P. Shine, "Source and sinks of zonal momentum in the middle atmosphere diagnosed using the diabatic circulation," *Quarterly Journal of the Royal Meteorological Society*, vol. 115, pp. 265–292, 1989.
- [60] A. H. Oort, "Global atmospheric statistics, 1958-1973." Government Printing Office, Washington, D. C., 1983. NOAA Professional Paper No.14.
- [61] K. F. Klenk, P. K. Bhartia, E. Hilsenrath, and A. J. Fleig, "Standard ozone profiles from balloon and satellite data sets," *Journal of Climate and Applied Meteorology*, vol. 22, pp. 2,012–2,022, 1983.
- [62] G. M. Keating and D. F. Young, "Interim reference ozone models for the middle atmosphere," in *Atmospheric structure and its variation in the region 20-120 km: Draft of a new reference middle atmosphere* (K. Labitzke, J. J. Barnett, and B. Edwards, eds.), pp. 205–209, Middle Atmosphere Program, 1985. Handbook 16.
- [63] M. Wie, D. R. Johnson, and R. D. Townsend, "Seasonal distributions of diabatic heating during the First GARP Global Experiment," *Tellus*, vol. 35A, pp. 241–255, 1983.
- [64] D. Cunnold, F. Alyea, N. Phillips, and R. Prinn, "A three-dimensional dynamical-chemical model of atmospheric ozone," *Journal of the Atmospheric Sciences*, vol. 32, pp. 170–194, January 1975.
- [65] W. J. Randel, "Global atmospheric circulation statistics, 1000-1 mb," Tech. Rep. TN-295+STR, National Center for Atmospheric Research, Boulder, CO, December 1987.
- [66] S. A. Orszag, "Transform method for calculation of vector coupled sums: Application to the spectral form of the vorticity equation," *Journal of the Atmospheric Sciences*, vol. 27, pp. 890–895, 1970.
- [67] E. Eliassen, B. Machenaver, and E. Rasmussen, "On a numerical method for integration of the hydrodynamical equations with a spectral representation of the horizontal fields," Tech. Rep. 2, University of Copenhagen, Institute of Theoretical Meteorology, 1970.
- [68] A. Robert, J. Henderson, and C. Turnbull, "An implicit time integration scheme for baroclinic models of the atmosphere," *Monthly Weather Review*, vol. 100, pp. 329–335, May 1972.

- [69] R. J. Murgatroyd, "The structure and dynamics of the stratosphere," in *The Global Circulation of the Atmosphere* (G. A. Corby, ed.), pp. 159–195, London: Royal Meteorological Society, 1969.
- [70] M. R. Schoeberl, L. R. Lait, P. A. Newman, R. L. Martin, M. H. Proffitt, D. L. Hartmann, M. Loewenstein, J. Podolske, S. E. Strahan, J. Anderson, K. R. Chan, and B. Gary, "Reconstruction of the constituent distribution and trends in the Antarctic polar vortex from ER-2 flight observations," *Journal of Geophysical Research*, vol. 94, pp. 16,815–16,845, November 1989.
- [71] M. Schoeberl and L. R. Lait, "Conservative-coordinate transformations for atmospheric measurements," in *The Use of EOS for Studies of Atmospheric Physics* (J. C. Gille and G. Visconti, eds.), pp. 419–431, Italian Physical Society, 1992.
- [72] R. E. Young and G. L. Villere, "Nonlinear forcing of planetary scale waves by amplifying unstable baroclinic eddies generated in the troposphere," *Journal of the Atmospheric Sciences*, vol. 42, pp. 1,991–2,006, 1985.
- [73] O. B. Toon, R. P. Turco, D. Westphal, R. Malone, and S. Liu, "A multi-dimensional model for aerosols: Description of computational analogs," *Journal of the Atmospheric Sciences*, vol. 45, pp. 2,123–2,143, 1988.
- [74] O. B. Toon, C. P. McKay, T. P. Ackerman, and K. Santhanam, "Rapid calculation of radiative heating rates and photodissociation rates in inhomogeneous multiple scattering atmospheres," *Journal of Geophysical Research*, vol. 94, pp. 16,287–16,301, 1989.
- [75] R. D. McPeters, D. F. Heath, and P. K. Bhartia, "Average ozone profiles for 1979 from the NIMBUS 7 SBUV instrument," *Journal of Geophysical Research*, vol. 89, pp. 5199–5214, 1984.
- [76] C. R. Trepte, R. E. Veiga, and M. P. McCormick, "The poleward dispersion of Mount Pinatubo volcanic aerosol," *Journal of Geophysical Research*, vol. 98, pp. 18,563–18,573, October 1993.
- [77] J. M. Russell III, L. E. Deaver, M. Luo, R. J. Cicerone, J. H. Park, L. L. Gordley, G. C. Toon, M. R. Gunson, W. A. Traub, D. G. Johnson, K. W. Jucks, R. Zander, and I. G. Nolt, "Validation of hydrogen fluoride measurements made by the Halogen Occultation Experiment from the UARS platform," *Journal of Geophysical Research*, vol. 101, pp. 10,163–10,174, April 1996.
- [78] T. J. Dunkerton, "On the mean meridional mass motions of the stratosphere and mesosphere," *Journal of the Atmospheric Sciences*, vol. 35, pp. 2,325–2,333, December 1978.
- [79] W. J. Randel, "Global atmospheric circulation statistics, 1000-1 mb," Tech. Rep. TN-366+STR, National Center for Atmospheric Research, Boulder, CO, February 1992.

- [80] K. Labitzke, "Stratospheric temperature changes after the Pinatubo eruption," *Journal of Atmospheric and Terrestrial Physics*, vol. 56, no. 9, pp. 1,027–1,034, 1994.
- [81] S. Chandra, "Changes in stratospheric ozone and temperature due to the eruptions of Mt. Pinatubo," *Geophysical Research Letters*, vol. 20, pp. 33–36, January 1993.
- [82] M. Kawamata, S. Yamada, T. Kudoh, K. Takano, and S. Kusunoki, "Atmospheric temperature variation after the 1991 Mt. Pinatubo eruption," *Journal of the Meteorological Society of Japan*, vol. 70, pp. 1,161–1,166, December 1992.
- [83] W. J. Randel, F. Wu, J. M. R. III, J. W. Waters, and L. Froidevaux, "Ozone and temperature changes in the stratosphere following the eruption of Mt. Pinatubo," *Journal of Geophysical Research*, vol. 100, pp. 16,753–16,764, August 1995.
- [84] M. R. Schoeberl, P. K. Bhartia, E. Hilsenrath, and O. Torres, "Tropical ozone loss following the eruption of Mt. Pinatubo," *Geophysical Research Letters*, vol. 20, pp. 29–32, January 1993.
- [85] C. S. Zerefos, K. Tourpali, and A. F. Bais, "Further studies on possible volcanic signal to the ozone layer," *Journal of Geophysical Research*, vol. 99, pp. 25,741–25,746, December 1994.
- [86] W. B. Grant, E. V. Browell, J. Fishman, V. G. Brackett, R. E. Veiga, D. Nganga, A. Minga, B. Cros, C. F. Butler, M. A. Fenn, C. S. Long, and L. L. Stowe, "Aerosol-associated changes in tropical stratospheric ozone following the eruption of Mount Pinatubo," *Journal of Geophysical Research*, vol. 99, pp. 8,197–8,211, April 1994.
- [87] W. B. Grant, "Tropical stratospheric ozone changes following the eruption of Mount Pinatubo," in *The Mount Pinatubo Eruption Effects of the Atmosphere and Climate* (G. Fiocco, D. Fua, and G. Visconti, eds.), (Berlin-Heidelberg), pp. 161–175, Springer-Verlag, 1996. NATO ASI Series, vol. I 42.
- [88] J. K. Angell, "Estimated impact of Agung, El Chichón, and Pinatubo volcanic eruptions on global and regional total ozone after adjustment for the QBO," *Geophysical Research Letters*, vol. 24, pp. 647–650, March 1997.